

THESIS
2
2006

LIBRARY
Michigan State
University

This is to certify that the
dissertation entitled

Polycrystalline Diamond RF MEMS Resonator Technology and
Characterization

presented by

Nelson Sepúlveda-Alanastro

has been accepted towards fulfillment
of the requirements for the

Doctoral

degree in

Electrical and Computer
Engineering

Dr. Alan

Major Professor's Signature

December 8 2005

Date

MSU is an Affirmative Action/Equal Opportunity Institution

PLACE IN RETURN BOX to remove this checkout from your record.
TO AVOID FINES return on or before date due.
MAY BE RECALLED with earlier due date if requested.

DATE DUE	DATE DUE	DATE DUE

**POLYCRYSTALLINE DIAMOND RF MEMS RESONATOR TECHNOLOGY AND
CHARACTERIZATION**

By

Nelson Sepúlveda-Alancastro

A DISSERTATION

**Submitted to
Michigan State University
in partial fulfillment of the requirements
for the degree of**

DOCTOR OF PHILOSOPHY

Department of Electrical Engineering

2005

ABSTRACT

POLYCRYSTALLINE DIAMOND RF MEMS RESONATOR TECHNOLOGY AND CHARACTERIZATION

By

Nelson Sepúlveda-Alancastro

Due to material limitations of polycrystalline silicon resonators, polycrystalline diamond has been explored as a new RF MEMS resonator material. This work presents the development of polycrystalline diamond micro and nano resonators with quality factor (Q) values as high as 116,000.

Polycrystalline diamond resonator structures were tested using electrostatic and piezoelectric actuation. Similar resonator structures were tested using both testing methods, and their performance showed a difference in resonant frequency of about 3%, while the measured Q values differed by approximately a factor of 10.

The resonant frequency shifts due to different testing temperatures was quantified by the temperature coefficient (TC_f) value, which ranged from $-1.59 \times 10^{-5} / ^\circ\text{C}$ to $-2.56 \times 10^{-5} / ^\circ\text{C}$ for the different polycrystalline diamond structures. The Q values were not limited by clamping losses, phonon-phonon interaction or thermoelastic dissipation and they were measured as a function of temperature. The results showed an apparent thermally activated relaxation process, with an activation energy of 1.9 eV responsible for limiting the highest achievable Q value in the tested polycrystalline diamond resonators.

The fabrication technology and the performance of polycrystalline diamond resonators with dimensions in the nano scale are also presented. Polycrystalline diamond resonator cantilevers and torsional resonators with dimensions in the nanometer range (as

small as 100 nm) have been fabricated and tested. The performance of these structures shows resonant frequencies and Q values in the range of 23 KHz – 805 KHz and 2,800 – 103,600 respectively.

*To all those who defend peace
and happiness at the same time*

ACKNOWLEDGMENTS

First, I would like to thank my big and great family. My dad (Don Agustín Sepúlveda), who always motivated me to give the best of me. My mom (Doña Matilde Alancastro) who has been part of the “big events” in my life (even watching me strike out in a little league baseball game). My brothers (Isaías, Agustín, Ricardo, Jorge, “Cacho”, and Javier) and sisters (Nelly and Tere), which I have always felt close even though most of the time we have been physically distant. During my graduate school I married Laura, the most beautiful and wonderful girl in the planet. She has been very patient and also motivating during my career. Thanks also to “las malas compañías” from “El Colegio”. They showed me that friendship is a blessing.

This thesis would not have ever been written if it was not for those who inspired and motivated me to begin this journey after my B.S. degree. Thanks to Yuxing, Xiangwei, and Yang who helped me in my research and with which I spend happy and painful moments in the RCE.

Thanks also to Dr. John Sullivan for his knowledge and friendship, and to The Bill and Melinda Gates Foundation for their financial support.

TABLE OF CONTENTS

LIST OF TABLES	x
LIST OF FIGURES	xi
CHAPTER I: Research Motivation and Goals	1
1.1 Introduction	1
1.2 Objective of this Work	2
1.3 Overview of this Thesis	3
CHAPTER II: Background	5
2.1 Introduction	5
2.2 Resonator Theory and Operation	5
2.2.1 Resonance Frequency	5
2.2.2 Quality Factor	9
2.2.2.1 Lorentzian Fit	11
2.2.3 Actuation and Detection Methods	12
2.2.3.1 Electrostatic Actuation	13
2.2.3.2 Piezoelectric actuation and Optical Detection	19
2.2.3.3 Magnetomotive Actuation	22
2.3 Energy Dissipation Mechanisms	22
2.3.1 Extrinsic Mechanism	23
2.3.2 Intrinsic Mechanism	24
2.4 Micromechanical Resonator Structures and Limitations	28
2.4.1 Micromechanical Resonators	28

2.4.2 Resonator Geometry.....	28
2.4.3 Resonator Materials.....	33
2.4.4 Resistance Rx.....	35
2.5 Polycrystalline Diamond Material.....	36
2.5.1 Why Diamond?.....	36
2.5.2 Chemical Vapor Deposition (CVD) of Diamond Films.....	38
2.5.3 Seeding.....	40
2.5.4 Doping.....	40
2.5.5 Patterning.....	41
CHAPTER III: Polycrystalline Diamond Film Technology.....	43
3.1 Introduction.....	43
3.2 Seeding.....	43
3.3 Film Growth Process.....	44
3.4 Doping.....	46
3.5 Patterning.....	48
3.6 Surface Roughness.....	55
3.7 Microresonator Fabrication Process.....	57
3.7.1 Fabrication Technology.....	57
3.7.1.1 Samples for Electrostatic Testing.....	58
3.7.1.2 Samples for Piezoelectric/Optical Testing.....	61
3.7.2 Post-Processing.....	63
CHAPTER IV: Resonator Testing Methods.....	65
4.1 Introduction.....	65

4.2 Electrostatic Testing.....	65
4.2.1 Electrostatic Testing Equipment Set-Up.....	65
4.2.2 Electrostatic Testing Measurement Results.....	66
4.3 Piezoelectric Actuation with Optical Detection.....	69
4.3.1 Piezoelectric Actuation and Optical Detection Results.....	69
4.4 Comparison of Results.....	73
CHAPTER V: Study of Q and Frequency Shifts in Polycrystalline Diamond Resonators.....	79
5.1 Introduction.....	79
5.2 Quality Factor Limitations.....	79
5.3 Quality Factors in Polycrystalline Diamond Resonators.....	81
5.4 Polycrystalline Diamond Film Microstructure.....	85
5.4.1 <i>Seeding</i> Layer and <i>Film</i> Layer.....	86
5.5 Temperature Dependence.....	92
5.5.1 Young's Modulus and Frequency Temperature Dependence.....	92
5.5.2 Quality factor temperature dependence.....	94
CHAPTER VI: Polycrystalline Diamond Nanoresonators.....	101
6.1 Introduction.....	101
6.2 Fabrication of Nanoresonators.....	101
6.3 Torsional Resonators.....	102
6.3.1 Testing of Torsional Resonators.....	104
6.4 Nanocantilevers.....	105
6.4.1 Testing of Nanocantilevers.....	109
CHAPTER VII: Conclusions and Future Research.....	116

7.1 Summary and Conclusions.....	116
7.2 Future Research.....	117
BIBLIOGRAPHY.....	119

LIST OF TABLES

2.1	Constant K_n for the first five flexural modes of a bridge structure.....	7
2.2	Resonator structures fabricated from polycrystalline diamond. The torsional resonator shown in the second row was patterned at Sandia National Laboratories. The other structures were completely fabricated at Michigan State University.....	31
2.3	Properties of materials that can be used to fabricate micromechanical resonators.....	34
2.4	Most recent results for diamond resonators before the work reported in this thesis.....	35
3.1	Growth parameters for the three polycrystalline diamond samples studied and dry etching parameters (superscript denotes the sample on which the value was used).....	46
4.1	Results for piezoelectrically-actuated cantilever beams (first vibration mode) made from sample	70
4.2	Polycrystalline diamond growth parameters for the sample tested electrostatically and piezoelectrically.....	73
5.1	Polycrystalline diamond and polycrystalline silicon properties used for plotting the dissipation curves in figure 5.1.....	81
5.2	Ratio of seeding and film thickness to total thickness for each sample and the average of the 15 higher measured Q values for each sample ($\overline{Q_{tot}}$).....	88
6.1	Measurement results for single and double torsional resonators.....	105
6.2	Results of polycrystalline diamond nanocantilevers fabricated from sample 1. The resonant frequencies were calculated using the width as the resonator thickness (a), and the film thickness as the resonator thickness (b). M^* represents the number of measurements taken from each structure (the values shown in the table correspond to the measurement with the highest measured Q).....	114

LIST OF FIGURES

1.1	Thesis overview.....	4
2.1	Bridge resonator diagram to be tested using electrostatic actuation [8].....	6
2.2	Example of resonant peak obtained using electrostatic actuation. The resonant frequency and Q are obtained directly from the measured data shown in the spectrum.....	11
2.3	Schematic diagram for piezoelectric actuation and detection. The reflected laser beam from the vibrating structure is sent to a photodetector. A network analyzer uses the output of the photodetector to plot the resonance spectrum.....	21
2.4	Schematic diagram for the magnetomotive actuation and detection.....	22
2.5	a) HFCVD and b) MPCVD polycrystalline diamond deposition.....	39
3.1	Raman spectra for the three samples studied.....	48
3.2	<i>Grass effect</i> diagram. The sputtering of aluminum during the dry etching of diamond prevents the plasma from etching the diamond under the sputtered aluminum.....	51
3.3	Evidence of the <i>grass effect</i> found on (a) the dry etching of the polycrystalline diamond resonators reported in this thesis and (b) the DRIE of silicon-on-insulator wafers [78].....	52
3.4	Released polycrystalline diamond structures (comb-drives and bridges) patterned at Michigan State University. No <i>grass effect</i> can be observed.....	53
3.5	a) Fabricated and patterned polycrystalline diamond resonators from [31] and b) Michigan State University (reported in this thesis).....	54
3.6	AFM images showing the polycrystalline diamond surface roughness of Sample 3 (a) and Sample 2 (b). The difference in the film roughness is about 5 nm.....	56
3.7	Starting substrate for the fabrication of polycrystalline diamond resonators.....	57
3.8	Fabrication process flow for electrostatically tested resonators.....	59
3.9	Fabrication process flow for resonators to be tested using piezoelectric actuation and optical detection.....	63

4.1	Connections to the resonator structure for electrostatic testing. In order to measure only the change in current across the resonator, a bias tee is used to isolate the dc- bias from the IN-port of the network analyzer.....	66
4.2	Electrostatic measurements on polycrystalline diamond resonators: a) bridge structure, b) comb-drive. The resonant frequency (f_o) was calculated by finding the frequency at maximum magnitude and the Q was calculated using this f_o value and the 3dB bandwidth (Δf).....	68
4.3	Young's modulus of sample 1 was calculated from a linear fit done to the measured data.	72
4.4	Raman spectra for samples measured using different actuation methods: a) piezoelectric b) electrostatic.....	74
4.5	Testing results on two similar polycrystalline diamond cantilevers using different actuation and detection methods.....	76
5.1	Energy loss mechanism curves for a 1 μm thick poly-crystalline diamond and polycrystalline silicon cantilever beam.....	80
5.2	Q value limiting curves for a 0.6 μm polycrystalline diamond cantilever beam and measured data for the three samples.....	82
5.3	Measured Q values as a function of frequency for the three studied samples. Resonant peaks show the highest Q value for each sample.....	84
5.4	Cross section TEM images of the three studied polycrystalline diamond samples.....	86
5.5	Plot of $1/Q_{tot}$ as a function of t_s/t_{tot} . The values for Q_f and Q_s are obtained from the slope and intercept of the linear fit.....	89
5.6	The approximation for the minimum space of solutions is determined by the rectangle, which touches all the curves at least in one single point.....	91
5.7	Young's modulus temperature dependence for the three samples. The three samples have very similar slopes and the sample 1 showed the highest Young's modulus at room temperature.....	93
5.8	Frequency shift as a function of testing temperature for sample 1.....	95
5.9	Frequency shift as a function of testing temperature for sample 2.....	96

5.10	Frequency shift as a function of testing temperature for sample 3.....	97
5.11	Measured Q values vs. temperature a) Three samples plotted in the entire testing temperature range; b) Sample 2 in the range of temperature where a minimum in Q was observed.....	99
5.12	Measured Q values vs. activation energy for the three samples. A minimum in Q was observed for two of the three samples at an activation energy around 1.9 eV.....	100
6.1	SEM image of polycrystalline diamond single torsional resonator.....	103
6.2	Excitation of torsional resonator. The offset of the paddle support from the center of the paddle causes a torsional vibration mode.....	104
6.3	Smooth sidewalls of polycrystalline diamond nanocantilevers fabricated using e-beam lithography.....	107
6.4	Use of piezoelectric actuation and optical detection for a cantilever with vibration perpendicular to the substrate (a) and parallel to the substrate (b). The vibration will be in the direction parallel to the smallest dimension of the cantilever.....	108
6.5	100 nm wide polycrystalline diamond cantilever. The top view shows that the width of the cantilever is in not uniform along the beam length.....	109
6.6	SEM image and performance of the nanocantilever with the highest measured Q.....	110
6.7	SEM image and performance of a 100 nm wide polycrystalline diamond nanocantilever.....	111
6.8	Plot of measured Q values on cantilever beams made of silicon nitride [26], single crystal silicon [26] and polycrystalline diamond (reported in this work). All the cantilevers had a thickness between 170 nm and 200 nm.....	115

Chapter 1

Research Motivation and Goals

1.1 Introduction

Microsystems and Broadband/wireless communication systems need high performance, low-cost, low-power and small-size components. Such components can lead to single-chip transceivers and microsystems. However, the majority of the high-Q bandpass filters commonly used in the radio frequency (RF) and intermediate frequency (IF) stages of transceivers are realized using off-chip, mechanically resonant components, such as crystal filters and surface acoustic wave (SAW) devices. These off-chip resonator components can contribute to the substantial percentage (often up to 80%) of portable transceiver area taken up by board-level passive components.

Recently, silicon-based low-power resonant micromechanical structures have been fabricated. Microelectromechanical systems (MEMS) technologies that make it possible to fabricate high quality factor (Q) on-chip micromechanical resonators [1,2] now suggest a method for miniaturizing and integrating highly selective filters alongside transistors leading to miniaturized transceivers. Among the RF MEMS components that could replace conventional components in cellular and cordless applications are image reject and IF filters with center frequencies in the ranges of 0.8 - 2.5 GHz and 0.455 - 254 MHz, respectively [1]. Some of the specific devices fabricated are tunable micromachined capacitors, integrated high-Q inductors, low-loss micromechanical switches, and micromechanical resonators with quality factors (Qs) above 10,000. Microfabricated resonant structures for sensing pressure, acceleration, and vapor

concentration have been demonstrated [3]. Recent advances in IC-compatible MEMS technologies suggest methods for board-less integration of wireless transceiver components [4]. In fact, given the existence already of technologies that merge micromechanics with transistor circuits onto single silicon chips [4-7], single-chip RF MEMS transceivers are not a far goal anymore.

However, before one can take full advantage of RF MEMS, a number of issues need to be addressed including higher frequency, selectivity, vacuum encapsulation and reliability. In order to solve these issues, researchers have tried to use different resonator structures, designs and materials.

1.2 Objective of this Work

Polycrystalline silicon has been the material of choice for RF MEMS micromechanical resonators. It is, however, found that reducing the resonator dimensions (to achieve higher frequencies) close to or below 1 μm for polycrystalline silicon resonators is expected to lead to size related limitations due primarily to enhanced adsorption properties of water-related species to the silicon surface. As diamond surfaces are known to be chemically inert to such adsorption and diamond has the highest Young's Modulus (which allows higher resonant frequencies) among all the materials, polycrystalline diamond micromechanical resonators are expected to be superior to silicon based resonators.

The goal of this work is to study the polycrystalline diamond material for its use as a structural material in RF MEMS micromechanical resonators. The major accomplishments and/or contributions to the scientific community reported in this thesis include the following:

- 1) The development of the fabrication technology for polycrystalline diamond RF MEMS resonators.
- 2) The testing of polycrystalline diamond resonator using different techniques showed similar resonant frequencies but differences in Q values by a factor of 10.
- 3) Achievement of the highest Q of 116,000 measured for any polycrystalline diamond resonators structure or cantilever beams made of any polycrystalline material.
- 4) Study of the energy dissipation mechanisms (which influence the Q) in polycrystalline diamond micromechanical resonators and their relation to the film microstructure.
- 5) Study of the temperature dependence of the resonant frequency and Q in polycrystalline diamond resonators.
- 6) Fabrication and testing of polycrystalline diamond nanocantilevers with widths as small as 100 nm.

1.3 Overview of this Thesis

This thesis presents the development and characterization of a polycrystalline diamond microresonator fabrication technology capable of achieving high Q and nano-sized polycrystalline diamond resonators. Chapter 2 explains the theory of the resonator dynamic behavior and the different actuation and detection methods that can be used for the testing of micromechanical resonators. It also discusses the energy dissipation mechanisms, the micromechanical resonators limitations and the polycrystalline diamond material. The third chapter on this thesis talks about the polycrystalline diamond microresonator technology used for the fabricated and tested devices. The details for

polycrystalline diamond film growth and patterning are presented with some of the issues faced and ways to avoid/solve them. The fourth chapter describes the measurement techniques used and the equipment set up. It discusses the measurement results on the two actuation and detection techniques used: 1) electrostatic actuation and detection and 2) piezoelectric actuation with optical detection. Then, in chapter five, the energy dissipation mechanisms present in polycrystalline diamond micromechanical resonators and the thermal stability of such devices are discussed. The last chapter shows the technology for the fabrication of nano sized cantilever beams and the results obtained from such structures. The following figure (figure 1.1) shows an overview of this thesis.

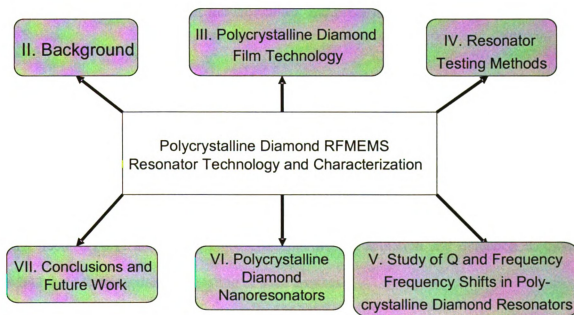


Figure 1.1: Thesis Overview

Chapter 2

Background

2.1 Introduction

This chapter presents the theory necessary to understand the dynamic behavior of micromechanical resonators and discusses the energy dissipation mechanisms, which are responsible for limiting the Q . It also mentions the resonator geometries and materials commonly used, their limitations and a summary of the latest results obtained for RF MEMS resonators. Finally, the justification for using polycrystalline diamond and some of the common techniques for the fabrication and processing of polycrystalline diamond films are discussed.

2.2 Resonator Theory and Operation

For the understanding of the operation of an RF MEMS micromechanical resonator there are important concepts and parameters such as resonance frequency and Q that need to be clear. Some related concepts are the actuation and detection methods, which help to understand the testing of such devices.

The following section describes the concept of resonant frequency assuming electrostatic actuation and detection is used as the testing technique.

2.2.1 Resonance frequency

Figure 2.2 shows a typical clamped-clamped (bridge) structure [8]. It is clamped at both ends, and a capacitance is formed between the beam and the underlying electrode.

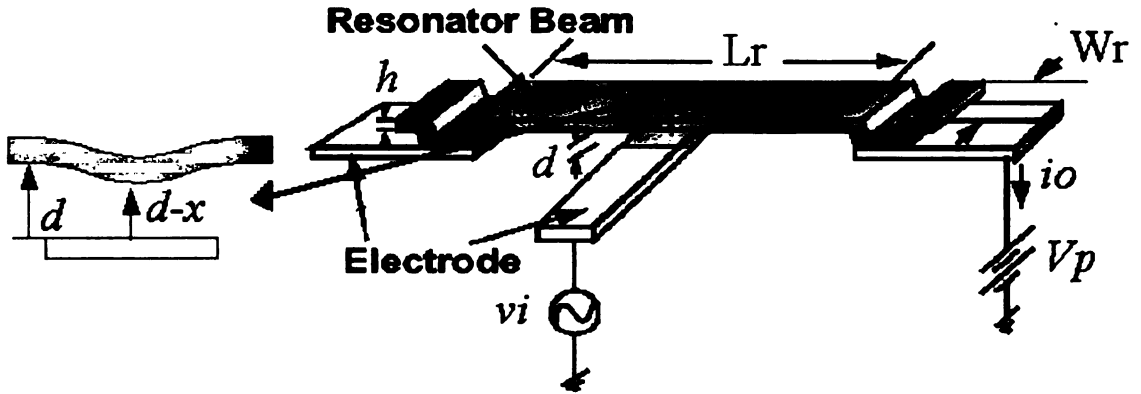


Figure 2.1 Bridge resonator diagram to be tested using electrostatic actuation [8].

An infinite number of resonance modes are possible for the structure presented in figure 2.1. The frequency of each mode is determined by the structural material properties and resonator geometry. The resonance frequency f_{rn} of a given mode n for the bridge in figure 2.1 is given by the expression [9]

$$f_{rn} = \frac{1}{2\pi} \sqrt{\frac{k_r}{m_r}} \quad (2.1)$$

where k_r and m_r are the stiffness and mass of the beam respectively. The stiffness is given by [9]:

$$k_r = EW_r \frac{h^3}{L_r^3} \quad (2.2)$$

where E is the Young's modulus of the structural material; L_r , W_r and h are the beam length, width and thickness specified in figure 2.1 respectively. By substituting equation

(2.2) in equation (2.1) the following expression for the resonance frequency of a bridge resonator is obtained:

$$f_{rn} = \frac{1}{2\pi} \sqrt{\frac{E}{\rho}} \frac{h}{L_r^2} \quad (2.3)$$

where ρ is the density of the structural material. Different modes are distinguished by a constant K_n . If this constant is taken into consideration a more general expression for the resonant frequency of a bridge or cantilever beam can be obtained [10]:

$$f_{rn} = K_n \sqrt{\frac{E}{\rho}} \frac{h}{L_r^2} \quad (2.4)$$

The constant K_n will depend on the vibration mode the beam is operated and is tabulated for the first five modes of a bridge structure in table 2.1.

Table 2.1 Constant K_n for the first five flexural modes of a bridge structure

Mode	n	Nodal Points	K_n	f_{rn}/f_0
Fundamental (f_0)	1	2	1.03	1
1 st Harmonic (f_2)	2	3	2.83	2.76
2 nd Harmonic (f_3)	3	4	5.55	5.4
3 rd Harmonic (f_4)	4	5	9.18	8.93
4 th Harmonic (f_5)	5	6	13.72	13.34

Now, equation (2.4) is the mechanical resonance frequency of the resonator if there were no electrodes or applied voltages. The presence of electrostatic forces on the vibrating beam seems to alter the stiffness of the beam [11]. Mathematically, it may be appropriate to re-define the spring constant k_r . If k_r is the spring constant in the absence of electrostatic forces, then

$$k'_r = k_r - k_e \quad (2.5)$$

where k_e is the electrostatic spring stiffness, which is subtracted from the spring constant k_r to give the “modified” spring constant k'_r . Thus equation (2.1) can be modified to:

$$f_{rm} = \frac{1}{2\pi} \sqrt{\frac{k'_r}{m_r}} = \frac{1}{2\pi} \sqrt{\frac{k_r - k_e}{m_r}} = \frac{1}{2\pi} \sqrt{\frac{k_r}{m_r}} \left[1 - \frac{k_e}{k_r}\right]^{1/2} \quad (2.6)$$

A good approximation for k_e , can be made to get [11]:

$$k_e = \frac{(\epsilon A V_P^2)}{d^3} \quad (2.7)$$

where A is the electrode overlap area, ϵ is the permittivity of free space, V_P is the dc bias applied to the resonator and d is the electrode to resonator gap as shown in figure 2.1.

After substituting equation (2.2) and equation (2.7) in equation (2.6) and taking in account the constant K_n discussed earlier the following equation is obtained:

$$f_{rm} = K_n \sqrt{\frac{E}{\rho}} \frac{h}{L_r^2} \left[1 - \left\langle \frac{\epsilon A V_P^2 L^3}{d^3 E W h^3} \right\rangle\right]^{1/2} \quad (2.8)$$

It is important to remember that equation (2.8) adds the effect of electrostatic actuation testing, and therefore it can only be used when this testing method is used. When testing methods that do not affect the spring constant (k_r) of the resonator structure are used, the resonant frequency can be calculated using equation 2.4. Due to the fact that the polycrystalline diamond Young's Modulus is about 6 times larger than that of polycrystalline silicon, the ratio $\left\langle \frac{k_e}{k_r} \right\rangle = \left\langle \frac{\epsilon A V_P^2 L^3}{d^3 E W h^3} \right\rangle$ is about 6 times smaller for a polycrystalline diamond beam when compared to a polycrystalline silicon. For a typical bridge structure (100 μm long, 10 μm wide, 2 μm thick) with a gap spacing of 0.2 μm , an electrode beam overlap of 20 μm and a DC bias (V_p) of 2V, the ratio $\left\langle \frac{k_e}{k_r} \right\rangle$ is 0.06 for a polycrystalline silicon beam and 0.01 for a polycrystalline diamond beam.

2.2.2 Quality factor

Another parameter that is important to study in order to characterize the performance of a resonator is the Q. The Q is defined as the ratio between the energy stored in the system to the energy lost per cycle. It describes the frequency selectivity of the device (i.e. the device response to a specific frequency). Processes or mechanisms, which increase the energy dissipated in the resonator are sources of Q degradation. Section 2.3 explains in more detail the energy dissipation mechanisms for a micromechanical resonator.

High Q resonators are necessary for sensor and RF MEMS applications. In sensor applications, if a resonator is exposed to a chemical leading to a change in its mass, a

shift in its resonant frequency could be used to detect the chemical. The shift in resonant frequency needed for detection or sensing of a mass change is determined more precisely if the resonator has a high Q. Thus, the sensitivity of a microresonator based sensor increases with Q. Also, a high Q value is desirable for oscillators and filter applications, where the frequency of operation needs to be carefully controlled.

The Q of a resonator can be obtained in different ways. When electrostatic actuation and detection is used for testing the resonator, the measured output is the magnitude of the S_{21} scattering parameter (y-axis) as a function of frequency (x-axis). The scattering parameters are commonly used in RF circuits to measure the ratio of the output power signal to the input power signal. When the resonator beam is vibrating, the changes in the output current (which are discussed in section 2.2.3.1) are reflected on the output power signal used to determine the scattering parameters. In most cases, the magnitude of the S_{21} parameter is converted to decibels by using $|S_{21}|_{dB} = 20 \times \log(|S_{21}|)$.

The frequency at maximum magnitude is used as the resonant frequency f_0 . The half power points $(1/\sqrt{2} \max |S_{21}|)$ [12] are determined on either side of the resonant frequency and the difference of those frequency positions is the bandwidth Δf . If the $|S_{21}|$ value is in decibel units ($|S_{21}|_{dB}$), then the half power points are located at the two points of the curve which are 3dB apart from the maximum magnitude $(20 \times \log (1/\sqrt{2} \max |S_{21}|) = |S_{21}|_{dB} - 3\text{dB})$.

Figure 2.2 shows an example of a resonant peak obtained using electrostatic testing and the procedure for calculating the Q. This method relies solely on the measured

data. However, there is a more accurate method for calculating the resonator Q, which uses a curve fit.

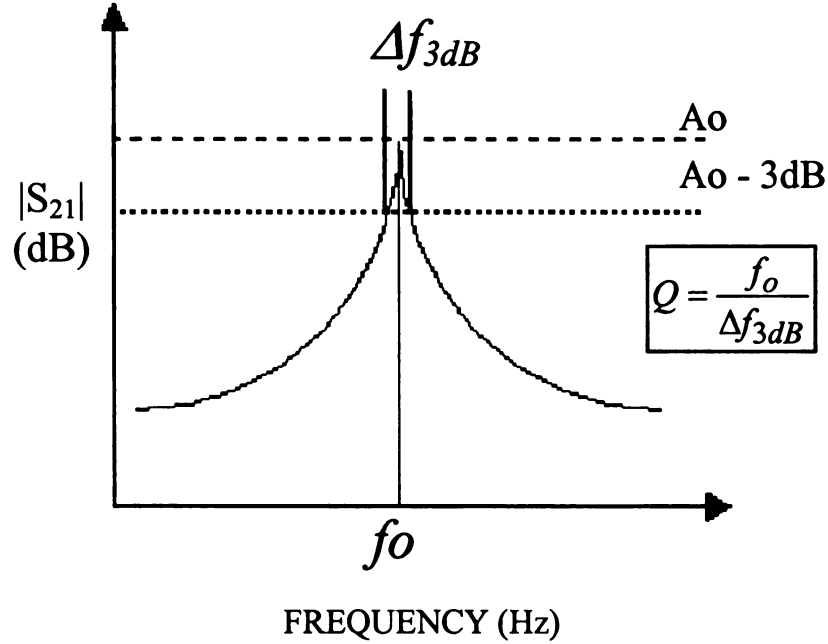


Figure 2.2 Example of resonant peak obtained using electrostatic actuation. The resonant frequency and Q are obtained directly from the measured data shown in the spectrum.

2.2.2.1 Lorentzian fit

The equation for a Lorentzian curve is given by [12]:

$$y = \frac{y_{\max}}{\sqrt{1 + 4Q^2 \left[\frac{x}{x_0} - 1 \right]^2}} \quad (2.9)$$

where x_0 is the x value that corresponds to y_{\max} . It has been found that the most accurate fit for the resonant curve of micromechanical resonators is a Lorentzian curve using nonlinear least-squares fit using frequency in the x-axis and a variable directly proportional to the resonator amplitude of motion (such as $|S_{21}|$ or the voltage read from

a photodetector) in the y-axis [12]. Therefore, the data from which the resonant peak is plotted can be fit with a Lorentzian curve, and the frequency f_0 and Q parameters can be extracted from the fit.

2.2.3 Actuation and detection methods

Different resonator actuation and detection methods have been described and used [13,14,15]. The two techniques most commonly used for micromechanical resonator measurement are the capacitive (electrostatic actuation and detection) and the combination of mechanical actuation (piezoelectric actuation) with optical detection. The electrostatic method measures the change in the scattering parameter S_{21} (caused by a change in the output current) for the detection of motion and the mechanical method measures the change in an optical (laser) signal reflected from the resonator surface for motion detection. The change in output current for the electrostatic actuation is caused by the change in charge across the vibrating resonator which behaves as a time varying capacitor. However, as the structure gets smaller and its geometry more complicated, the difficulty to use these two techniques for movement detection increases significantly.

The problem with optical detection is the minimum spot size of the laser. If the laser spot size is larger than $1\text{ }\mu\text{m}$, it would be difficult to measure the reflected signal from the surface of a resonator with dimensions smaller than $1\text{ }\mu\text{m}$. Also, the laser induces noise such as heating.

The capacitive method suffers from various drawbacks such as parasitic capacitances (which are difficult to account for) [16]. Restrictions on the device design and changes to the structural material (e.g. the stiffness of the material) are introduced due to the current flow, which limits the material capabilities [17].

The third method for actuation and detection of a resonator is the magnetomotive technique. This method makes use of the Lorentz force [18]. A drawback of this method is that in order to prevent heating the structure has to have low resistance [19]. For a polycrystalline diamond resonator this can only be accomplished with heavy doping or a thick metal film on top of the resonator, which makes this method unsuitable if the intrinsic characteristics of diamond are of interest. These three techniques are described in more detail in the following sections.

2.2.3.1 Electrostatic actuation

When electrostatic force is used, a dc-bias V_P is applied to the suspended beam, and an ac input voltage $v_i = V_m \sin \omega t$ (V_m is in the range of the mV) is applied to the electrode under the beam (see figure 2.1). Therefore, the resulting electrostatic potential across the beam is

$$v = v_i + V_P. \quad (2.10)$$

In a vibrating resonator, the capacitance formed between the bottom electrode and the beam is changing with time. Therefore, the charge stored in the capacitor is also changing with time, which implies a current flow. From equation (2.10) three different inputs can be analyzed: 1) $v = V_P$ ($v_i = 0$), 2) $v = v_i$ ($V_P = 0$) and 3) $v = v_i + V_P$. Each one of these cases is analyzed separately.

First, let the input to the system be purely dc (i.e. $v = V_P$). The electrostatic force will make the beam bend towards the bottom electrode, generating a change in capacitance for a short period of time. However, once the system reaches its equilibrium,

the beam stops moving, and the equivalent circuit can be represented by a dc voltage source connected in series with a capacitor. The expression for the current flowing through a capacitor is:

$$i_o = \frac{\partial Cv}{\partial t} = C \frac{\partial v}{\partial t} + v \frac{\partial C}{\partial t} \quad (2.11)$$

From (2.11) it can be seen that if neither the voltage nor the capacitance varies with time, the current will be zero. Therefore, in steady state, the current for a purely dc input would be zero.

Now, let $v=v_i$. If the frequency of this input signal ($f_i = \frac{\omega_i}{2\pi}$) is far from the natural frequency of the beam ($f_0 = \frac{\omega_0}{2\pi}$), the beam does not vibrate, and therefore the capacitance between the beam and the electrode does not change with time. The second term in (2.11) becomes zero, and the total current becomes $i_o = C \partial v_i / \partial t$. As the frequency of the ac signal approaches the natural frequency of the beam, it begins to vibrate, creating a time varying capacitor. Then the current is given by (2.11) with $v = v_i$.

The third input $v = v_i + V_P$ results in a current given by

$$i_o = C \frac{\partial(v_i + V_P)}{\partial t} + (v_i + V_P) \frac{\partial C}{\partial t} \quad (2.12)$$

Since the magnitude of the ac signal (V_m) is in the range of mV and the dc signal is in the range of Volts, the current is significantly increased when the dc signal is added to an ac signal with frequency close to the natural frequency of the resonator.

Knowing that the change of V_P with respect of time is zero ($\partial V_P / \partial t = 0$), equation (2.12)

can be simplified to:

$$i_o = C \frac{\partial v_i}{\partial t} + (v_i + V_P) \frac{\partial C}{\partial t} \quad (2.13)$$

Now, in the second term in equation (2.13) V_P is added to v_i and since the magnitude of

the ac signal is in the mV range, it can be neglected and we get the following equation:

$$i_o = C \frac{\partial v_i}{\partial t} + V_P \frac{\partial C}{\partial t} \quad (2.14)$$

The derivative of capacitance with respect of time ($\partial C / \partial t$) can be expressed as:

$$\frac{\partial C}{\partial t} = \frac{\partial C}{\partial x} \frac{\partial x}{\partial t} \quad (2.15)$$

where the derivative of capacitance with respect to the displacement x can be obtained directly from the plate capacitance formula:

$$C = \frac{\epsilon_0 A}{(d - x)} \quad (2.16)$$

where ϵ_0 is the permittivity of free space, A is the electrode area, d is the initial electrode

gap, and x is the beam displacement (see figure 2.1).

So, after taking the derivate of the capacitance with respect to displacement x we get;

$$\frac{\partial C}{\partial x} = \frac{\epsilon A}{(d - x)^2} \quad (2.17)$$

For a typical vibrating beam the beam displacement is very small when compared to the gap spacing ($x \ll d$). So, equation (2.17) can be simplified to:

Substituting equation (2.18) in equation (2.15) and the result in equation (2.14), the following equation is obtained:

$$i_o = C \frac{\partial v_i}{\partial t} + \frac{V_P \epsilon A}{d^2} \frac{\partial x}{\partial t} \quad (2.19)$$

Defining the new variable η to be:

$$\eta = \frac{V_P \epsilon A}{d^2} \quad (2.20)$$

Using this variable η (herein after referred as *electromechanical transduction factor*) equation (2.19) can be simplified to:

$$i_o = C \frac{\partial v_i}{\partial t} + \eta \frac{\partial x}{\partial t} = i_{ac} + i_{mot} \quad (2.21)$$

The first term is recognized as the normal ac-current through the capacitor and the second term is the *motional current* $i_{mot} = \eta^* \partial x / \partial t$, due to the time varying capacitance. Since the current is proportional to the dc-bias, it is reasonable to think of the dc-bias as a parameter to use for getting a more noticeable peak in the transmission spectrum. However, when the dc-bias voltage V_P is sufficiently large, catastrophic failure of the device ensues, in which the resonator beam is pulled down onto the electrode. This leads to either destruction of the device due to excessive current passing through the now shorted electrode to resonator path. The dc-bias voltage V_P at which this event occurs is known as the pull-in voltage (V_{PI}). The pull-in voltage can be estimated to be [20]

$$V_{PI} = \sqrt{\frac{8k_{eff} d^3}{27\epsilon_0}} \quad (2.22)$$

where

$$k_{eff} = \frac{8\sigma_o h}{L_r^3} \frac{[(\frac{k_o L}{2}) \sinh(\frac{k_o L_r}{2})]}{(\frac{k_o L_r}{2}) \sinh(\frac{k_o L_r}{2}) + 2(1 - \cosh(\frac{k_o L_r}{2}))} \quad (2.23)$$

In (2.23) σ_o , h and L_r are the residual stress, thickness and length of the beam

respectively,

$$\text{and } k_o = \sqrt{\frac{12\sigma_o}{Eh^2}}.$$

Equation (2.22) yields a pull-in voltage, which captures the dependence of pull-in voltage on beam dimensions, elastic modulus, and residual stress. However, since the gap under the beam is not uniform, this approximation is off by about 20% [20]. Expressions for the pull-in voltage of the beam have been developed by adding some adjustable constants so that the pull-in voltage expression matches the calculated behavior based on full non-linear simulations [20]. This has been done, with a factor added to account for electrostatic fringing at the edges of the beam. The result is [20]

$$V_{PI} = \sqrt{\frac{4\gamma_1(\sigma_o h d^3)}{\epsilon_o L^2 D(\gamma_2, k_o, L)[1 + \gamma_3 \frac{d}{W}]} } \quad (2.24)$$

where

$$D(\gamma_2, k_o, L) = 1 + 2 \frac{[1 - \cosh(\gamma_2 k_o \frac{L}{2})]}{(\gamma_2 k_o \frac{L}{2}) \sinh(\gamma_2 k_o \frac{L}{2})} \quad (2.25)$$

The values of the constants for a fixed-fixed beam with fully clamped boundary conditions are $\gamma_1=2.79$, $\gamma_2=0.97$ and the fringing field correction term is $\gamma_3=0.42$ [20].

So far, the system has been described in the electrical domain. Now, let's see how the voltages applied to the resonator relate to the forces in the system. The application of the voltage input to the resonator creates an electrostatic force between the electrode and the beam. The energy stored in the parallel plate capacitor C formed by the beam and the electrode is:

$$E = \frac{1}{2} C v^2 \quad (2.26)$$

Then, by substituting the voltage given by equation (2.10) into equation (2.26) we get

$$E = \frac{1}{2} C (V_P^2 + 2v_i V_P + v_i^2) \quad (2.27)$$

The force is obtained from

$$F = \frac{\partial E}{\partial x} = \frac{1}{2} v^2 \frac{\partial C}{\partial x} \quad (2.28)$$

and using the simplified derivative of capacitance with respect to distance obtained in equation (2.18), and substituting it into equation (2.28) we get:

$$F = v^2 \frac{\epsilon A}{2d^2} \quad (2.29)$$

Now, substituting (2.10) into (2.29) we get:

$$F = (V_P^2 + 2v_i V_P + v_i^2) \frac{\epsilon A}{2d^2} \quad (2.30)$$

As can be seen in equation (2.30), there are three forces: a dc-force ($V_p^2 \frac{\epsilon A}{2d^2}$), a force at the excitation frequency f due to a combination of ac and dc ($2v_i V_p \frac{\epsilon A}{2d^2}$) and a force at twice the excitation frequency due to the square term ($v_i^2 \frac{\epsilon A}{2d^2}$). The $v_i^2 \frac{\epsilon A}{2d^2}$ term is very small in comparison to the other two terms (V_m in the mV range) so it can be ignored. When the beam is vibrating, and the system has reached equilibrium, the pure dc-term ($V_p^2 \frac{\epsilon A}{2d^2}$) has no effect on the device response. It is a purely dc-force that statically bends the beam but dynamically has no effect on the frequency response. In other words, the pure dc-term ($V_p^2 \frac{\epsilon A}{2d^2}$) is a constant term which does not influence the force frequency. So, when the beam is actuated, and begins to vibrate, after reaching equilibrium the frequency of the force acting on the beam can be calculated by:

$$F = \frac{v_i V_p \epsilon A}{d^2} = \eta v_i \quad (2.31)$$

where the variable η is the electromechanical transduction factor defined in (2.20) and it represents the connection between the mechanical and electrical domain in the system.

2.2.3.2 Piezoelectric actuation and optical detection

The basic idea behind the piezoelectric actuation method is to physically attach the sample that contains the resonator structure to a piezo transducer. This piezo element is driven to vibration at a frequency determined by the output of a spectrum analyzer. For the laser detection, a laser is focused on the vibrating beam and the reflected signal is

used to determine the frequency of vibration. A schematic of the piezoelectric actuation and detection set up is shown in figure 2.3.

The frequency of a light source changes with the speed of the light source (Doppler effect). Since the reflective surface of the resonator can be considered as a point source, this effect can be employed to detect the vibration of a resonator. A laser is reflected off the point of the resonator structure where the amplitude of motion is maximum (for a cantilever, this point would be the tip of the cantilever, for a bridge, this point would be the beam midpoint along the length axis), and directed to a photodiode. Depending on the angle between the surface of the cantilever and the incident laser beam, the position of the reflected light at the detector changes. This is how the photodiode detects when the device is vibrating.

In this technique, light from a laser was passed through a lens, which caused the beam to diverge, and then it was sent through another lens to focus the light. The now converged beam is reflected off a mirror, through the vacuum chamber window and focused on the resonator structure of interest. The beam hits the sample and the reflected light is sent to a split photodiode. The reflected light is positioned so that the light on the two halves of the photodiode is about the same. Then the difference between the photovoltages is the output from the photodetector, and this is then routed into the spectrum analyzer that is simultaneously driving the piezo element that is driving the resonator into vibration. When the beam is vibrating, the output from the photodetector is maximum and a resonant peak is observed in the spectrum analyzer. This technique is very similar to the one used in AFM's.

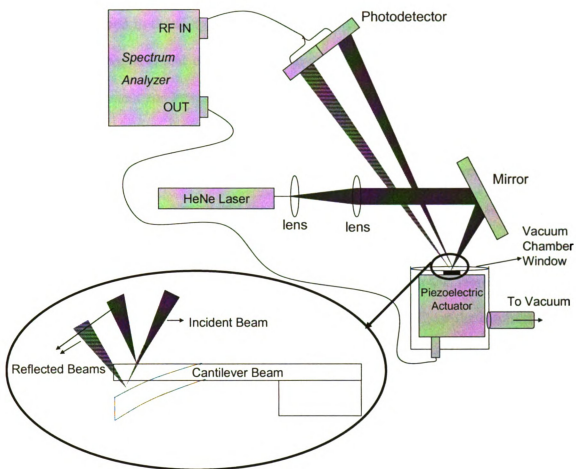


Figure 2.3 Schematic diagram for a the piezoelectric actuation and detection. The reflected laser beam from the vibrating structure is sent to a photodetector. A network analyzer uses the output of the photodetector to plot the resonance spectrum

The force that drives the resonator comes from the piezo-transducer that mechanically shakes the sample containing the resonator. The detection is done by monitoring the reflected light from a laser that was focused on the resonator. This technique does not involve any current flow through the resonator and therefore the sample does not need to be conductive.

The optical detection scheme used in this work was light interferometry, which has been described in detail by Czaplewski [13]. In this technique, a better resolution of the cantilever displacement can be obtained, and therefore resonator structures with a smaller displacement can be tested.

2.2.3.3 Magnetomotive actuation

If an ac current flows through a wire that is exposed to a perpendicular magnetic field, a force acts on the current and the wire moves perpendicular to the magnetic field. Since the current is oscillating the wire also oscillates and an electromotive force (emf), having the same frequency, is induced in the wire. To pick up the vibration either the reflected voltage can be measured with a network analyzer [18], or the electromagnetic power that is absorbed by the motion of the beam can be measured [21]. To excite the resonator, relatively large magnetic fields are required (up to 12 Tesla [21]). So, the idea is to excite the resonator by applying a drive current through an electrode on its surface in the presence of a magnetic field perpendicular to the length of the current carrying electrode, and motion is detected by measuring the induced emf in the electrode. Figure 2.4 shows a diagram of the parameters involved in this type of technique.

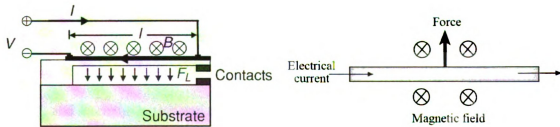


Figure 2.4 Schematic diagram for the magnetomotive actuation and detection

2.3 Energy Dissipation Mechanisms

As it was mentioned earlier, the Q of a microresonator can be improved by

minimizing the energy losses. The energy loss mechanisms can be divided in two categories; extrinsic and intrinsic.

2.3.1 Extrinsic mechanisms

Extrinsic loss mechanisms have nothing to do with the material itself but are influenced by the design of the microresonator structures. Intrinsic loss mechanisms, on the other hand, are the loss mechanisms that come from the material properties, and will limit the highest possible achievable Q. Two main extrinsic loss mechanisms are the energy losses due to clamping and air damping.

Clamping losses originate from the fact that since no structure can be perfectly rigid, energy can be dissipated from the resonator to the support structure, where local deformations and microslip can occur. By increasing the rigidity of the anchor, the movement in this area of the resonator is decreased. As a result of this decrease in displacement, the anchor losses are reduced. It is often not possible to increase the rigidity of the support, but energy losses can be reduced by optimizing the structure design. In the case of a cantilever beam, if the support is considered as an infinitely large elastic plate, the damping ratio of the radiation on the support was given by Hosaka *et al.* and the maximum achievable Q can be estimated from the following equation [22]:

$$Q_{clamp} = .34 \times \frac{L^3}{h^3} \quad (2.32)$$

where L and h are the length and thickness of the cantilever respectively.

Air damping arises from the transfer of mechanical energy to the gas surrounding the structure [22]. Depending on the pressure level the microresonator is subjected while it is being tested, air damping may affect its Q. At pressures below 10 mtorr, the air

damping is negligible compared to the intrinsic damping of the vibrating beam itself. Since at this pressure level intrinsic mechanisms limit the Q, this pressure regime is called the *intrinsic damping region*. When the pressure is between 4 torr and 10 mtorr (*molecular region*), the Q is inversely proportional to P, following the relationship [22]:

$$Q = \frac{2\pi f_n h \rho}{k_m P} \quad (2.33)$$

where f_n is the resonance frequency of the n^{th} vibrational mode, ρ is the density, P is the gas pressure, and $k_m = [(32M)/(9\pi RT)]^{1/2}$, where M is the molecular weight of the gas, R is the gas constant, and T is the temperature. At pressures above 4 torr (*viscous region*) the air acts as a viscous fluid and air damping becomes a significant factor for limiting the Q. In this region the Q is limited by the following expression [23]:

$$Q = \frac{\rho h l}{6\pi\mu \left(1 + \frac{w}{\sigma}\right)} 2\pi f_n \quad (2.34)$$

where w and l are the beam width and length respectively, μ is the dynamic viscosity of the medium, $\sigma = \sqrt{\frac{2\mu RT}{PM 2\pi f_n}}$ and P, M, R, T and f_n are the same parameters used for (2.33).

The maximum Q for a 100 μm long, 10 μm wide, 1 μm thick polycrystalline diamond cantilever beam, is in the order of 10,000 when it is operated at a pressure of 75 mtorr (*molecular region*), and about 500 when it is operated at 7 torr (*viscous region*).

2.3.2 Intrinsic mechanisms

Intrinsic loss mechanisms, on the other hand, are the loss mechanisms that come from the material properties, and will limit the highest possible achievable Q. Energy

losses due to thermoelastic dissipation (TED), phonon-phonon interaction, and internal friction can be considered intrinsic loss mechanisms.

It is well known that a material that possesses a positive coefficient of thermal expansion will experience a temperature increase when subjected to a compressive stress and a decrease in temperature when subjected to a tensile stress. When a resonator vibrates in a vibrational mode other than pure torsion, it experiences both tensile and compressive stresses in the structure, leading to regions of elevated and reduced temperatures. For example, when a cantilever beam is operated in its flexural mode, one of its surfaces experiences a tensile stress while the other a compressive stress. As a result, one side of the beam has a higher temperature than the other. Some of the mechanical energy in the resonator is lost due to heat flow from the warmer to the cooler side of the resonator, and this is known as thermoelastic dissipation. Following Roszhart [24], the thermoelastically limited Q value (Q_{TED}) can be obtained from the product of two different functions $\Gamma(T)$ and $\Omega(f)$ in the following way:

$$Q_{TED} = \frac{1}{2\Gamma(T)\Omega(f)} \quad (2.35)$$

The term $\Gamma(T)$ depends on temperature and contains the material dependencies of the TED process. It can be expressed as [24]:

$$\Gamma(T) = \frac{\alpha^2 T E}{4\rho C_p} \quad (2.36)$$

where T is the cantilever temperature α is the coefficient of thermal expansion and C_p is the specific heat capacity. The term $\Omega(f)$ depends on the cantilever resonant frequency and it can be expressed as [24],

$$\Omega(f) = \frac{2f/F_0}{1 + \left(f/F_0\right)^2} \quad (2.37)$$

where f is the cantilever frequency and F_0 is the frequency at which heat flows from the warm side to the cool side. This F_0 value can be calculated from [24],

$$F_0 = \frac{\pi\kappa}{2\rho C_p h^2} \quad (2.38)$$

where κ is the thermal conductivity of the cantilever. If the temperature is fixed, $\Gamma(T)$ becomes a constant, leaving $\Omega(f)$ as the parameter to influence Q_{TED} . When the cantilever frequency f matches the characteristic frequency F_0 , $\Omega(f)$ becomes unity and Q_{TED} gets to its lowest value. The larger the difference between f and F_0 , the smaller $\Omega(f)$ gets, and the larger Q_{TED} becomes.

When a beam is vibrating, the mechanical vibration of the structure (sound waves) can interact with the thermal phonons changing the population distribution of thermal phonons [25]. This process leads to a direct conversion of mechanical energy into a temperature increase of the resonator and is the origin of the phonon-phonon energy loss mechanism. The highest achievable Q limited by phonon-phonon interaction is given by [25],

$$Q_{ph} = \frac{\rho v^2}{CT\gamma^2} \left[\frac{\omega\tau_{ph}}{1 + (\omega\tau)^2} \right]^{-1} \quad (2.39)$$

where v is the sound velocity, γ is the Gruneisen's constant, and τ_{ph} is the phonon relaxation time. The phonon relaxation time can be calculated from the longitudinal and transverse velocities of sound in the material from the following equation [25],

$$\tau_{ph} = \frac{3\kappa}{\rho C_p v_D^2} \quad (2.40)$$

where v_D is the Debye sound velocity, which is obtained from [25],

$$v_D = \sqrt[3]{\frac{3v_l^3 v_t^3}{v_t^3 + 2v_l^3}} \quad (2.41)$$

Here in equation (2.41) v_l and v_t are the velocity of longitudinal and transverse sound waves in the material, respectively.

Another energy loss mechanism can arise from internal friction. Such an energy loss mechanism can be associated with defects (intrinsic or extrinsic) in the crystal lattice [13]. Additionally, there are energy loss mechanisms related to the surface of the resonator, which are not well understood. In many cases, a linear relationship between the energy loss and the surface area to volume ratio has been observed [19,23,26], suggesting that the Q is limited by surface losses. The reported studies on the origin of surface losses point at either a thin film of a different material on the surface of the resonator [26] or the resonator surface roughness [16].

2.4 Micromechanical Resonator Structures and Limitations

The three methods used for increasing the performance (i.e. resonant frequency and Q) of a micromechanical resonator are:

- 1) The use of materials with superior elastic properties
- 2) The use of strategic resonator geometries
- 3) Decreasing resonator dimensions

Researchers have used combinations of these 3 techniques to achieve resonators with unique performance [7,8,11,22,26,27]. However, these techniques have challenges that need to be overcome. Every resonator geometry and material has some advantages and some limitations.

2.4.1 Micromechanical resonators

The resonator structure stiffness and mass depend on the resonator geometry and size. Therefore, the natural mechanical frequency of the micromechanical resonator will also depend on the type of structure (geometry). However, no matter which type of geometry or operation mode (i.e. flexural, torsional or radial contour) is being analyzed; the frequency will always depend on the elastic properties of the material the device is made of. For example; a cantilever beam, comb-drive or bridge structure has a resonant frequency that is dependent on the material's Young's modulus, and the torsional resonator has a resonant frequency dependent on the material's shear modulus.

2.4.2 Resonator geometry

As it was mentioned before, the modification of resonator geometry is one of the tools used for increasing the fundamental frequency of the device, and also the Q. Table 2.2 shows pictures of some resonator structures fabricated from polycrystalline diamond.

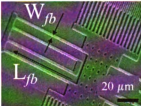
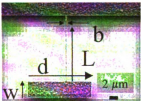

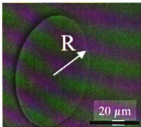
The structures in this table have different advantages and disadvantages in their performance.

The first resonator shown in table 2.2 is a comb-drive structure. Comb-drive structures can be designed to get a Q higher than even free-free beams (i.e. 100,000 when operated at 1m torr) [23]. However, these structures tend to have a low resonance frequency (KHz range), since their dimensions and consequently their mass are much larger than other structures. Due to the geometrical complexity of comb-drive structures, it is harder to reduce the size of these devices than it is to reduce the size of a bridge structure. Since the resonant frequency of a structure is inversely proportional to the resonator mass, most comb-drive structures show a lower frequency than bridges or other structures that can be fabricated in much smaller sizes.

The next structure in table 2.2 is a torsional resonator. Torsional resonators can be operated in a torsional mode (instead of flexural as in the bridge, comb-drive, cantilever and free-free structures), which makes the resonant frequency dependent on the shear modulus instead of the Young's modulus. When this type of resonator is excited in its pure torsional mode, the structure does not experience the tensile and compressive stress as in the case for other vibration modes. This eliminates the regions in the structure with elevated and reduced temperatures. Therefore, there is no heat flow across the structure and the losses due to thermoelastic dissipation (TED) are eliminated. Torsional resonators have the limitation of having only one torsional vibration mode, limiting the number of resonant frequencies for a specific device (when it is operated in their torsional modes) to one.

The third row of table 2.2 shows an SEM picture of a 92MHz free-free beam flexural mode micromechanical resonator with some of its dimensions. This device is comprised of a free-free micromechanical beam supported at its flexural node points by four torsional beams, each of which is anchored to the substrate by rigid contact anchors. The free-free beam supports will be located at the nodal points of the beam. At these points there is ideally no movement. As a result, anchor dissipation mechanisms normally found in the bridge structure, are greatly suppressed (ideally zero), allowing much higher device Q . It can be noticed from equations (2.4) and (2.32) that the resonant frequency increases and that the Q_{clamp} decreases with decreasing beam length. Therefore, if the clamping losses are the dominant energy dissipation mechanism on a cantilever beam, then the Q values would decrease with increasing resonant frequency. However, since clamping losses do not affect free-free beams; the Q does not drop with frequency.

Table 2.2 Resonator structures fabricated from polycrystalline diamond. The torsional resonator shown in the second row was patterned at Sandia National Laboratories. The other structures were completely fabricated at Michigan State University.

Structure	Picture	Performance	Frequency
Comb-Drive		-High Qs due to low anchor losses - Low frequency due to large mass	$f_o = \frac{1}{2\pi} \sqrt{\frac{E}{\rho} \left[\frac{2hE \left(\frac{W_{fb}}{L_{fb}} \right)^3}{V_p + \left(\frac{1}{4} \right) V_t + \left(\frac{12}{35} \right) V_b} \right]}^{\frac{1}{2}}$ <p>Where W_{fb} and L_{fb} are the width and length of the folded beam suspensions; h is the thickness; and V_p, V_t and V_b are the shuttle volume, the total combined volume of the folding trusses and total combined volume of the suspended beams respectively.</p>
Torsional		- Operated in torsional mode. No dissipation due to thermoelastic dissipation	$f_o = \sqrt{\frac{.0522Gb^3}{\rho w L d^3}}$ <p>Where G is the shear modulus, d and w are the paddle's length and width respectively, and b and L are the paddle's support length and width.</p>
Free-Free		-No anchor losses (ideally)	$f_o = K_n \sqrt{\frac{E}{\rho} \frac{h}{L^2}}$ <p>Free-Free beams share the same dynamic behavior as a Clamped Clamped Beam; therefore the frequency is the same given by equation (2.4)</p>
Disk		-Radial contour mode operation instead of flexural	$\delta \times J_0 \frac{(\delta)}{J_1}(\delta) = 1 - \sigma$ $\delta = \omega_o \times R \times \sqrt{\frac{\rho \times (1 - \sigma^2)}{E}}$ <p>Where R is the disk radius; $\omega_o = 2\pi f_o$ is its angular resonance frequency; $J_n(y)$ is the Bessel function of the first kind of order n; and ρ, σ and E are the density, poisson ratio, and Young's modulus of the disk structural material respectively.</p>

70MHz bridges have been tested under 50 μ Torr vacuum and the results have been compared to a free-free beam with similar dimensions [11]. The results show a Q difference by a factor of 28 between both structures with the same frequency. This shows that free-free beams can operate at the same frequency of a bridge with similar dimensions but a much larger Q.

In a disk structure (last row of table 2.2), if the position of the anchor (at the middle of the disk) is carefully controlled, and the anchor is made from a different material than the disk, the anchor losses can also be suppressed. These advantages allow this type of structure to have a high frequency and Q as it was shown for polycrystalline silicon [7]. The disk resonator shown in table 2.2 has achieved the highest resonance frequency (1.51GHz when operated in its second radial-contour mode) while maintaining relatively large dimensions (20 μ m diameter) and a decent Q (17,458 for first mode, 11,555 for the second one). The device consists of a 2 μ m-thick nanocrystalline diamond disk suspended by a stem located at its center and enclosed by polycrystalline silicon electrodes spaced less than 1,000Å from the disk perimeter. Such tiny lateral electrode-to resonator gaps were achieved using a recent lateral sub- μ m gap process technology that combines surface micromachining technologies with a sacrificial sidewall technique to achieve sub-micron (sub- μ m) lateral gaps without the need for aggressive lithography or etching [27]. Since the center of the disk corresponds to a node location for the radial contour vibration mode shape, anchor losses through the supporting stem are greatly suppressed, allowing this design to retain a very high Q.

The fourth column in Table 2.2 shows the equation for determining the resonant frequency of each device. Either the Young's or shear moduli (E or G) is present in all

these equations. Since diamond is the hardest material known, the use of polycrystalline diamond in small strategic resonator geometries is the best alternative for achieving high frequency RF MEMS resonators.

2.4.3 Resonator materials

So far, polycrystalline silicon has been the preferred material for RF MEMS resonators [27,28,29]. This is mainly due to the fact that silicon technologies have been deeply studied, and are well known. However, the electrical and mechanical properties of polycrystalline silicon begin to rapidly degrade at elevated temperatures ($>350\text{ }^{\circ}\text{C}$), making it increasingly unsuitable for high temperature applications [30]. Materials with higher Young's and shear moduli will provide a larger resonant frequency as the equations in the fourth column of table 2.2 show. That is why polycrystalline silicon carbide and polycrystalline diamond materials are being studied for use in RF MEMS devices. Both materials have a larger Young's and shear moduli than polycrystalline silicon (see table 2.3). Early results on polycrystalline silicon carbide [30] and polycrystalline diamond [31,32] show that indeed devices made of these two materials show a higher resonance frequency than that of equivalently sized polycrystalline silicon versions. Polycrystalline diamond folded beam comb-drive micromechanical resonators have now been measured with resonance frequencies 1.77 times higher than that of identical polycrystalline silicon counterparts, 1.20 times higher than achievable by polycrystalline SiC, and 1.53 times higher than a previous attempt at using CVD polycrystalline diamond as a resonator structural material [32]. Also, polycrystalline diamond cantilever beams have shown the highest Q for cantilevers made of any polycrystalline material [33]. Table 2.4 shows the most recent and outstanding results

(prior to the work shown in this thesis) for diamond resonators tested using different actuation methods.

Table 2.3 Properties of crystalline materials that can be used to fabricate micromechanical resonators

Property / Material	Polycrystalline silicon	Polycrystalline silicon carbide	SCD	Units
Density, ρ	2300	3300	3500	Kg/m ³
Young's Modulus, E	150	448	1200	GPa
Shear Modulus, G	52	160	478	GPa
Acoustic Velocity, $\sqrt{E/\rho}$	8075	11652	18516	m/s
Normalized Acoustic Velocity	1	1.44	2.29	---

Table 2.4 Most recent results for diamond resonators before the work reported in this thesis

<i>Actuation Method</i>	<i>Structure</i>	<i>f_o</i>	<i>Q</i>
Electrostatic	Disk* [7]	1.51GHz	11,555
	Bridge [31]	2.938 MHz	6,225
	Comb-Drive [32]	27.35 KHz	36,460
Piezoelectric	Doubly-Clamped Paddle * [34]	640 MHz	~3,000
	Doubly-Clamped Paddle * [14]	157 MHz	~9,000
Magnetomotive	Doubly-Clamped Paddle * [14]	157 MHz	~9,000
* These structures (Doubly-Clamped Paddle and Disks) were made of nanocrystalline diamond			

2.4.4 Resistance R_x

Now that the GHz frequency range has been reached, micromechanical resonators are emerging as viable candidates for on-chip versions of the high-Q resonator used in wireless communication systems for frequency generation and filtering. Among the more important of the remaining issues that still hinder development of these devices in RF front ends is their larger-than-conventional impedance. In particular, it is their large impedance (commonly called motional resistance, R_x) that presently prevents micromechanical resonator devices in the VHF and UHF ranges from directly coupling to antennas in wireless communication applications, where matching impedances in the range of 50Ω and 330Ω are often required [35].

The most direct methods for lowering the motional resistance R_x of electrostatically actuated micromechanical resonators are [36]: 1) decrease the electrode-to-resonator gap; 2) raising the dc-bias voltage; and 3) summing together the outputs of an array of identical resonators. Each of these methods comes with drawbacks. The first two methods are very effective in lowering R_x , with exponential dependences. However, they do so at the cost of linearity [37]. On the other hand the third method improves linearity while lowering R_x . Unfortunately, the third method is difficult to implement, since resonators with identical responses are required. This is even harder for large Q devices.

2.5 Polycrystalline Diamond Material

In this thesis, the polycrystalline diamond material is studied for its use as a structural material for RF MEMS resonators. The following sections show the justification for the use of polycrystalline diamond and a summary of the reported properties and techniques for the processing of this material.

2.5.1 Why diamond?

The use of strategic geometries, and alternative materials, are the two methods of choice for increasing the resonance of the device. Going for smaller dimensions (sub- μm range) on polycrystalline silicon resonator structures is not practical due to enhanced adsorption properties of water-related species to the silicon surface. Diamond, with the highest acoustic velocity of $18,076 \text{ ms}^{-1}$ [38] and chemical inertness, seems to be the

most superior among the new materials including polycrystalline silicon carbide. The carbon-carbon sp^3 bonds in tetrahedral configuration, crucial for the formation of single crystal diamond (SCD), are responsible for a unique combination of diamond properties. However, SCD is too expensive for most applications in wireless systems. Furthermore SCD technology is not compatible with the conventional silicon technologies. Fortunately, the polycrystalline diamond, with physical properties approaching those of SCD, can be fabricated on silicon substrates using the chemical vapor deposition (CVD) techniques and its cost is comparable to that of polycrystalline silicon for film thicknesses in the range of 1 – 2 μm . Table 2.3 shows a comparison of properties of the three structural materials that have been studied for RF MEMS applications. Polycrystalline diamond films with the same acoustic velocity of SCD can be obtained by controlling the sp^3/sp^2 ratio during its growth [38].

As the polycrystalline diamond films contain sp and sp^2 carbon-carbon bonds leading to non-diamond phases at the grain boundaries, their properties, such as acoustic velocity can be affected adversely if the polycrystalline diamond quality, indicated by the sp^3/sp^2 ratio as measured by Raman spectroscopy, is not carefully controlled. As mentioned earlier, reducing the resonator dimensions close to or below 1 μm for polycrystalline silicon resonators is expected to lead to size related limitations due primarily to enhanced adsorption properties of water-related species to the silicon surface. The diamond surfaces are known to be chemically inert to such adsorption, which makes this material more suitable and reliable for resonators with dimensions below 1 μm .

2.5.2 Chemical Vapor Deposition (CVD) of diamond films

Thermodynamically, graphite, not diamond, is the stable form of solid carbon at ambient pressures and temperatures.

The CVD technique is based on decomposition of carbon-containing precursor molecules (typically CH_4) diluted in H_2 gas. This generally involves thermal (i.e. hot filament) or plasma (DC, RF, or microwave) activation, or use of a combustion flame (oxyacetylene or plasma torches). The fact that polycrystalline diamond films can be formed by CVD techniques is linked to the presence of H_2 and hydrocarbon molecules. The H_2 atoms are believed to play a number of crucial roles in the CVD process [39].

There are several techniques for the deposition of polycrystalline diamond including microwave plasma CVD (MPCVD), hot filament CVD, radio frequency CVD, and dc-arc jet CVD. MPCVD is the most widely used technique due to its efficacy to produce high film quality, large substrate size, less contamination and better controllability [40]. Figure 2.5 includes schematics of HFCVD and MPCVD techniques. These processes have been described in the past [41, 42, 43, 44].

All the deposition techniques rely on the ability to set up a dynamic non-equilibrium system, in which only sp^3 carbon bonding can survive. This is achieved by the presence of hydrocarbon radicals, and more importantly, by large quantities of atomic hydrogen in the deposition gas. The hydrocarbon radicals provide the vapor source of carbon for diamond deposition. The atomic hydrogen is believed to play two important roles: it eliminates sp^2 bonded carbon (graphite), while establishing the dangling bonds of the tetrahedrally bonded carbon sp^3 . By creating a plasma system where atomic hydrogen

predominates, any graphitic bonding is etched away. Atomic hydrogen etches both diamond and graphite out, but under typical CVD conditions, the rate of diamond growth exceeds its etch rate, while this is the opposite for other forms of carbon (graphite).

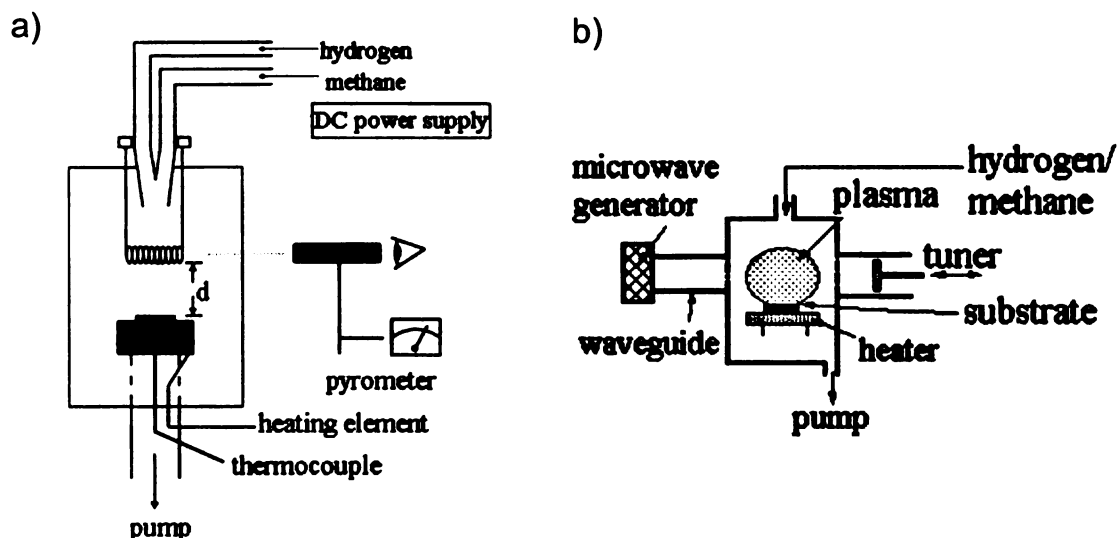


Figure 2.5 a) HFCVD and b) MPCVD polycrystalline diamond deposition

When the sample is ready for diamond growth it is loaded into the chamber and taken to a low pressure level. A mixture of gases (gases and their quantities depend on the type of polycrystalline diamond film that needs to be deposited) is then introduced into the chamber. The energy, provided by either D.C. power supply or microwave generator, helps creating the conditions inside the chamber for creating the plasma (ionized gas). The sample is heated by the plasma and usually monitored with a pyrometer.

2.5.3 Seeding

One of the most crucial steps in CVD growth of polycrystalline diamond films is generating seeds on the substrate (seeding) before the growth begins. In order to guarantee a continuous polycrystalline diamond film, a high nucleation density of diamond particles is necessary. Some of the techniques for this seeding step, are the abrasive polishing of the substrate with various grain sizes of diamond [45,46] and the ultrasonic agitation of the substrate with a diamond powder suspension [47,48,49,50]. Bias enhanced nucleation (BEN) has also been reported for effectively creating nucleation sites on silicon substrates [51] and preparing highly oriented diamond films [52,53].

An IC-compatible nucleation technique which does not cause surface damage [54] is the use of Diamond Powder Loaded Fluids (DPLF) with different carrier fluids, mean powder sizes and densities. The idea of this method is to spread diamond crystals, suspended in carrier fluids, on the substrate surface. During the diamond deposition process, the carrier fluids are evaporated at initial stages leaving behind the diamond particles which act as seeds for diamond growth. There are different ways to apply the DPLF to the substrate such as direct writing, spinning, spraying or brush painting.

2.5.4 Doping

As a wide band gap semiconductor material ($E_g = 5.5$ eV), CVD diamond films deposited without intentional doping are usually good insulators. Since the micromechanical resonators which are meant to replace oscillating components in transceivers need to be conductive, the diamond films used for the fabrication of such devices, need to be doped. Because the 2000 K temperature necessary for effective

diffusion in diamond is too high [55], diamond doping is performed either during growth, or by subsequent ion-implantation. Boron, aluminum, phosphorous, lithium and nitrogen have been tested as dopants for diamond [56].

Polycrystalline diamond film doping (p-type) during the CVD process is usually achieved by using pure boron powder [57], boron trioxide (B_2O_3) [58], diborane (B_2H_6) [59,60], or trimethylboron [61]. IR measurements have confirmed that boron atoms occupy substitutional sites [62]. Diamond quality, grain size, growth rate, hydrogen and oxygen contents, dislocation and planar defect densities are affected by boron doping [63-66]. The changes in polycrystalline diamond resistivity as a function of doping concentration have been reported by [40].

2.5.5 Patterning

Due to diamond's chemical inertness, standard wet etching techniques are not possible. Two patterning techniques can be applied: selective deposition and selective dry etching. Selective deposition is achieved by selective nucleation or by masking the areas where diamond growth is not desired. SiO_2 was successfully used as a masking layer by Masood et al. [54], Roppel et al. [66] and Davidson et al. [67]. A nucleation technique, which consists of spinning a layer of photoresist pre-mixed with diamond powder and lithographically patterning it, was developed at Michigan State University [54].

Selective etching of CVD diamond with SiO_2 or Si_3N_4 as a mask, was performed at atmospheric pressure, in oxygen environment at 700 °C, in a rapid thermal processor [54].

The dry etching of polycrystalline diamond, which uses different active gas species such as oxygen, argon, CF_4 and SF_6 with metal or SiO_2 masks [69-71] seems to be an excellent choice for polycrystalline diamond patterning. Most researchers have used conventional reactive ion etching (RIE) methods where the gas species are excited by RF power [71-72]. Dry etching using ECR assisted microwave plasma at low substrate temperatures and pressures has led to very clean structures with small feature sizes and sharp edges [73-74].

Chapter 3

Polycrystalline Diamond Film Technology

3.1 Introduction

The work reported in this thesis focuses on the use of polycrystalline diamond as a micromechanical resonator structural material. This chapter explains the polycrystalline diamond film technology used for the fabrication of such devices as well as the fabrication process flow.

3.2 Seeding

The seeding process influences the grain sizes in the polycrystalline diamond film and is the fabrication step responsible for guaranteeing a continuous film. The seeding technique used for the polycrystalline diamond films reported in this thesis consists of the use of a diamond powder loaded water suspension, commonly known as diamond in water (DW). This suspension is prepared by mixing of 25 carats of diamond powder, with an average particle size of 25 nm, in 1000 ml of deionized (DI) water and a suspension reagent. The DW suspension is placed in an ultrasonic bath for 30 minutes before it is intended to use.

For the fabrication of the resonators reported in this work, the surface over which the seeding will be done is mainly SiO₂. The starting substrate depends on the fabrication process that will be used, which are discussed in section 3.7.

The first step is to clean the substrate, which was done using RCA cleaning [74]. Then, before the DW was poured over the substrate a quick dip of the sample in a diluted

HF solution (1% HF in H₂O) for 10-20 seconds was done to clean the SiO₂ layer. It was observed that this HF dip step improved the DW suspension surface coverage over the sample. After the HF dip, the sample was rinsed in DI water for 5 minutes, and then blown dried with nitrogen. Now the samples are ready to be seeded. The DW suspension is taken out from the ultrasonic bath and it is poured over the substrate. The sample, which is now covered with the DW suspension, was loaded in a conventional spinner, and was spun for 30 seconds at 1000 rpm. For improving the seeding density, the spinning process was repeated more than once. This seeding method is particularly suitable for clean hydrophilic surfaces [75] such as SiO₂ or Si₃N₄. A nucleation density of 10^{11} cm^{-2} , and an average surface area of film grains of $0.06 \mu\text{m}^2$ has been obtained by using this seeding method [76].

3.3 Film Growth Process

All the CVD polycrystalline diamond films reported in this work were grown in a bell jar type MPCVD chamber (WavematTM MPDR 313EHP) with a 9 inch chamber diameter and a 5 inch quartz bell jar diameter. A 2.45 GHz, 5 kW microwave power supply (SairemTM GMP60KSM) and a large chamber size ensured the uniformity of the plasma. The sample wafer was heated by the plasma and its temperature was monitored by a pyrometer. The gas mixture introduced to the chamber depended on the properties needed for the diamond film. Since the polycrystalline diamond film quality increases with lower methane concentrations [77], the methane concentration was never above 2% of the total gas mixture.

As it will be seen in later chapters, a comparative study between different diamond films was made to identify the growth parameters that affect the diamond microstructure and consequently the Q. More precisely, the parameters varied in order to get diamond films with different microstructures were the growth temperature (600 °C - 780°C) and the gas percentage of tri-methyl-boron (TMB) in the MPCVD chamber during growth .

The following samples are referred to in the rest of the thesis.

- Sample 1: Undoped film grown 780 °C (66 measurements)
- Sample 2: Highly doped film grown at 780 °C (69 measurements)
- Sample 3: Undoped film grown at 600 °C (62 measurements)

Each sample represents one specific type of polycrystalline diamond film from which different resonator structures were tested at different vibration modes and temperatures.

Table 3.1 shows the polycrystalline diamond growth parameters used for each one of the films.

Table 3.1 Growth parameters for the three polycrystalline diamond samples studied and dry etching parameters (superscript denotes the sample on which the value was used)

Polycrystalline Diamond Film Growth		
Gas Flow Rate (sccm)	H ₂	100 ^{1,2,3}
	CH ₄	1 ^{1,2,3}
	TMB	4 ² ; 0 ^{1,3}
Temperature (°C)		780 ^{1,2} ; 600 ³
Microwave Plasma Power (kW)		2.0 ^{1,2,3}
MPCVD Gas Pressure (torr)		35 ^{1,2,3}
Seeding Diamond Powder Size (nm)		25 ^{1,2,3}
Dry Etching Parameters		
Gas Flow Rate (sccm)	CF ₄	1 ^{1,2,3}
	O ₂	30 ^{1,2,3}
Chamber pressure (mbar)		4x10 ⁻² ^{1,2,3}
DC Power (W)		400 ^{1,2,3}

Figure 3.1 shows the Raman spectra for three representative polycrystalline diamond films. It can be noticed that from the three samples, sample 1 has the best looking Raman peak at $\sim 1332 \text{ cm}^{-1}$. It has been reported how the doping of polycrystalline diamond films and the low temperature synthesis affect adversely the sp^3 to sp^2 ratio in polycrystalline diamond films [77]. This can also be seen from figure 3.1, where the sharpest diamond (sp^3 carbon-carbon bonding) peak corresponds to sample 1, which is the undoped film grown at the highest temperature (780°C).

3.4 Doping

If the micromechanical resonator is intended to be used in oscillator or filter applications, the resonator structural material needs to be conductive. The doping technique used in this work is done *in situ* using TMB. The boron doping of

polycrystalline diamond films using TMB has been investigated in the past as a function of TMB/CH₄ gas ratio, growth temperature and post growth anneal [40].

In this work, the diamond films that were heavily doped (e.g. sample 2) had a hole concentration around $1 \times 10^{17} \text{ cm}^{-3}$ and a resistivity of 0.15 $\Omega\text{-cm}$. This came as a result of a diamond growth gas mixture of 100:1:4 (H₂:CH₄:TMB).

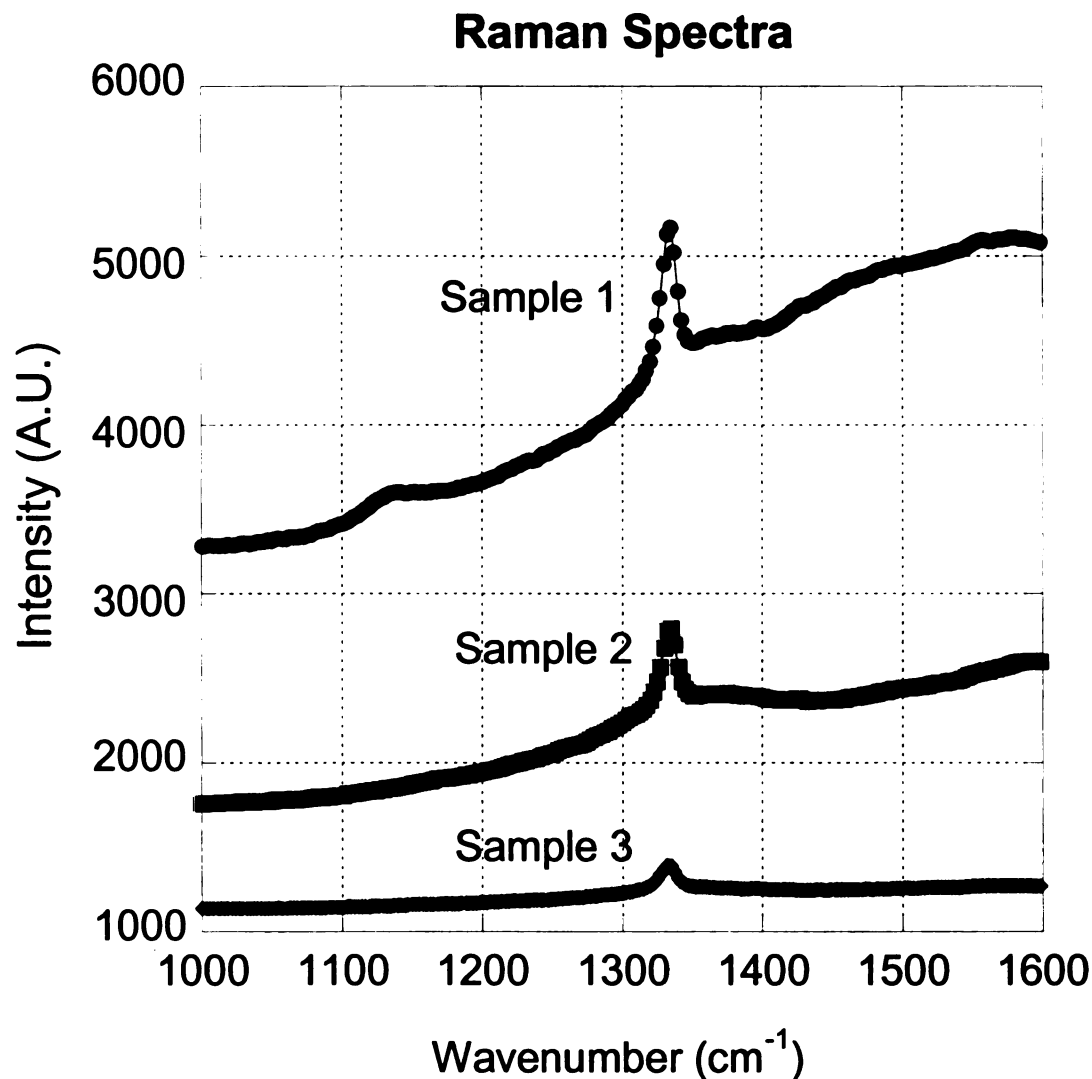


Figure 3.1 Raman spectra for the three samples studied

3.5 Patterning

As it was mentioned in the last chapter, due to chemical inertness of diamond, it can not be patterned using wet etching. The polycrystalline diamond patterning technique used in this work was dry etching using electron cyclotron resonance (ECR) assisted microwave plasma for the samples that were patterned at Michigan State University. For

the samples that were patterned at Sandia National Laboratories the dry etching was done using RF plasma. The dry etching system at Michigan State University etched polycrystalline diamond at an approximate rate of 0.05 $\mu\text{m}/\text{minute}$, while the polycrystalline diamond etch rate for the system at Sandia National Laboratories was about 0.03 $\mu\text{m}/\text{minute}$. Aluminum was used as a hard mask material in both cases for the selective dry etching of polycrystalline diamond. The etch rate for aluminum in both dry etching systems is much slower than the etch rate of polycrystalline diamond. For the dry etching system at Michigan State University, the aluminum was etched around 13 times slower than polycrystalline diamond [40], whereas for the system at Sandia National Laboratories the aluminum was etched around 4 times slower [13].

Some of the recipes for dry etching of polycrystalline diamond can cause aluminum sputtering over some areas of the diamond surface. When this happens, the plasma can not attack the diamond under the sputtered aluminum. As a result, one might end up getting “spikes” around the patterned structure after the dry etching of diamond is completed in the rest of the sample. This is called the *grass effect* (process shown in figure 3.2) and it has been reported in the past when deep reactive ion etching (DRIE) was used to pattern silicon-on-insulator wafers [78]. Figure 3.3-a shows SEM images of the *grass effect* noticed in the polycrystalline diamond structures patterned at Michigan State University with the spikes created by the *grass effect*. These spikes are likely to be polycrystalline diamond. Since the fabricated polycrystalline diamond resonator structures lie on top of the SiO_2 layer, when the structures are released, the spikes that are not attached to the structure are released as well. Figure 3.3-a shows areas where the spikes are still attached to the structure, and some of the released spikes. In order to

obtain these SEM images with the released diamond spikes, the samples did not go through the cleaning process after the release step, and they were loaded into the SEM right after release. Figure 3.3-b shows an SEM image of a patterned silicon structure showing also the spikes generated by the *grass effect* [78].

For the dry etching done at Sandia National Laboratories the gas mixture was a combination of oxygen plasma with CF_4 ($\text{O}_2:\text{CF}_4$; 30:1). This recipe etches Al at a faster rate and eliminated the *grass effect* by etching the sputtered aluminum which caused the diamond spikes. The samples that were patterned at Michigan State University had to go through a more vigorous rinsing process in order to eliminate the released diamond spikes from the sample.

Figure 3.4 shows SEM images of released polycrystalline diamond structures patterned at Michigan State University. Very clean surfaces and smooth sidewalls can be observed and the spikes discussed earlier are not noticed in these SEM images. For the patterning of these structures, the temperature inside the dry etching chamber was kept below 100 °C and the dry etching process was done for only 3 minutes. Since 3 minutes was not enough for etching the polycrystalline diamond film, the dry etching process was repeated until the polycrystalline diamond film was entirely removed. The dry etching system was not used for 30 minutes between each run. This suggests that a careful cleaning of the released samples together with a low temperature and short dry-etching intervals can also help reduce the sidewall roughness and lower the *grass effect*.

Figure 3.5 shows a comparison of the structures fabricated and patterned at Michigan State University and the very first set of results for polycrystalline diamond

resonators reported by [31]. The close up views of the structures show a comparable sidewall roughness.

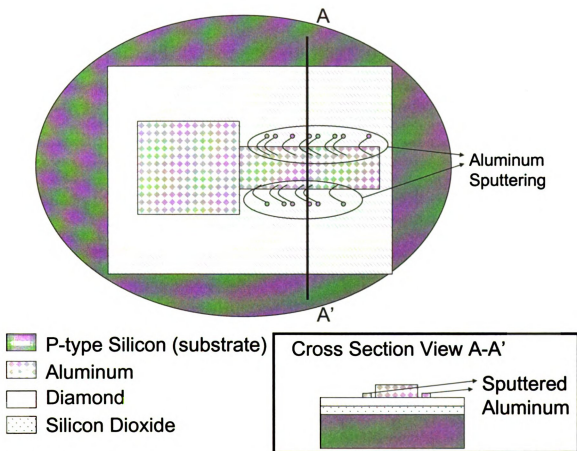


Figure 3.2 Grass effect diagram. The sputtering of aluminum during the dry etching of diamond prevents the plasma from etching the diamond under the sputtered aluminum.

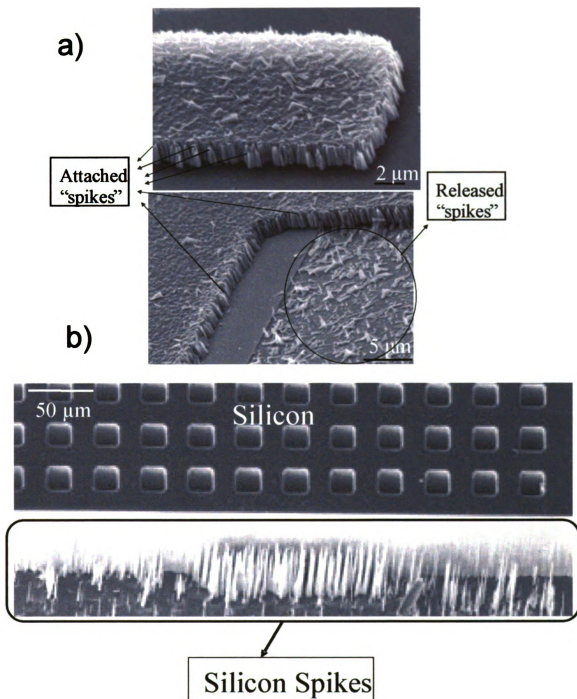


Figure 3.3 Evidence of the *grass effect* found on (a) the dry etching of the polycrystalline diamond resonators reported in this thesis and (b) the DRIE of silicon-on-insulator wafers [78].

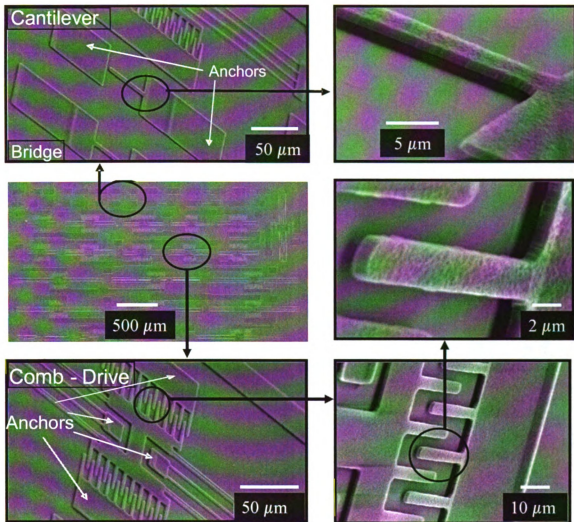


Figure 3.4 Released polycrystalline diamond structures (comb-drives and bridges) patterned at Michigan State University. No *grass effect* can be observed.

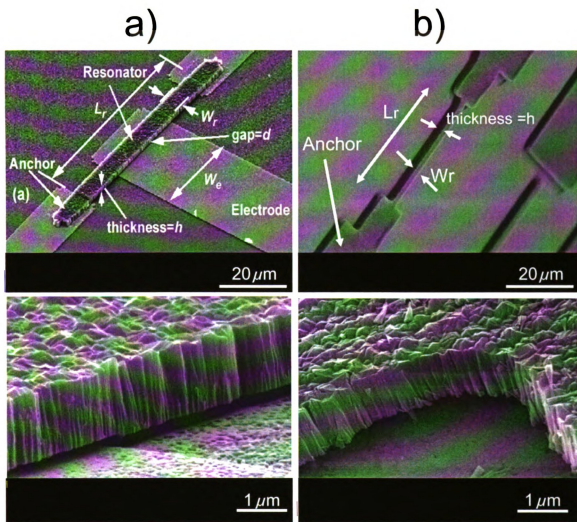


Figure 3.5 a) Fabricated and patterned polycrystalline diamond resonators from [31] and b) Michigan State University (reported in this thesis)

3.6 Surface Roughness

As it was mentioned in the previous chapter, researchers have found the surface roughness of a micromechanical resonator to influence the Q [19,23,26]. Randomly oriented polycrystalline diamond films (which are the ones used for this work), show very rough surfaces when compared to polycrystalline silicon films [79]. It is therefore important to have some control over the surface roughness in polycrystalline diamond films which are going to be used for micromechanical resonators. The results obtained in this work, show similar surface roughness for undoped films grown at 600 °C, and highly doped films grown at 780 °C (sample 2 and sample 3). Figure 3.6 shows AFM images of these two samples. The difference in surface roughness was only about 5 nm.

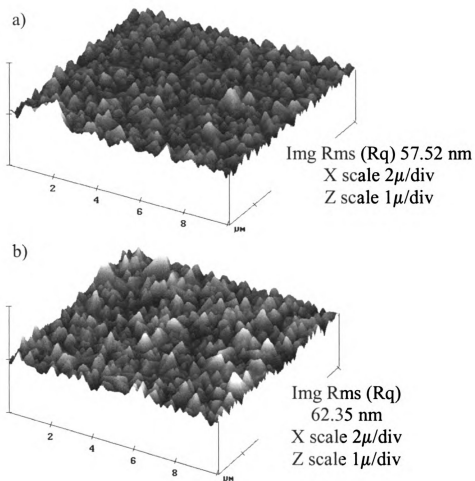


Figure 3.6 AFM images showing the polycrystalline diamond surface roughness of Sample 3 (a) and Sample 2 (b). The difference in the film roughness is about 5 nm.

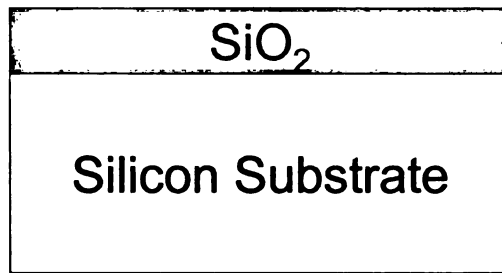


Figure 3.7 Starting substrate for the fabrication of polycrystalline diamond resonators

3.7 Microresonator Fabrication Process

The following section describes the fabrication process steps for the resonators used in this work.

3.7.1 Fabrication technology

In this work, two testing methods were used: 1) the electrostatic actuation and detection and 2) the piezoelectric actuation with optical detection. Depending on the testing method that will be used, micromechanical resonators can go through different fabrication steps. A device that has been fabricated for electrostatic actuation can be tested using either electrostatic or piezoelectric actuation with optical detection. However, if the device is going to be tested using only piezoelectric actuation with optical detection, the fabrication process can be simplified significantly. Both fabrication processes, begin with the same substrate which is shown in figure 3.7. It consists of a commercially available silicon wafer with a 2 μm thick thermal SiO_2 (wet grown) layer on top. The doping and orientation of the silicon wafer is not critical. In this thesis, a p-type (100) silicon wafer was used.

3.7.1.1 Samples for electrostatic testing

Figure 3.8 shows the fabrication process flow for a micromechanical resonator which is meant to be tested using electrostatic actuation and detection. The thermally grown SiO_2 layer that comes with the starting substrate is necessary to electrically isolate the devices from the substrate. The fabrication of these devices consists of a 3 mask fabrication process.

The first step for the fabrication of a micromechanical resonator that will be tested using electrostatic actuation and detection (after the starting substrate was cleaned using standard RCA cleaning process [74]) is the deposition of a thin (~ 300 nm) layer of silicon nitride (Si_3N_4). The deposition of this layer prevents the etching of the underlying SiO_2 layer at the time of release. The justification of this Si_3N_4 layer is explained in more detail later on, when the releasing of the structure is discussed. Since the purpose of this layer is to simply isolate the underlying SiO_2 layer from the future wet processing of the sample, the details about its deposition are not critical.

The second step is the deposition and patterning of the layer that will serve for making the electrical connections for testing (mask #1). Highly doped polycrystalline silicon has been used for this layer in the past. However, a metal had to be deposited over it, in order to decrease the contact resistivity [80]. In the work reported in this thesis, a single layer of chromium (100 nm thick) was deposited and patterned for electrical connections.

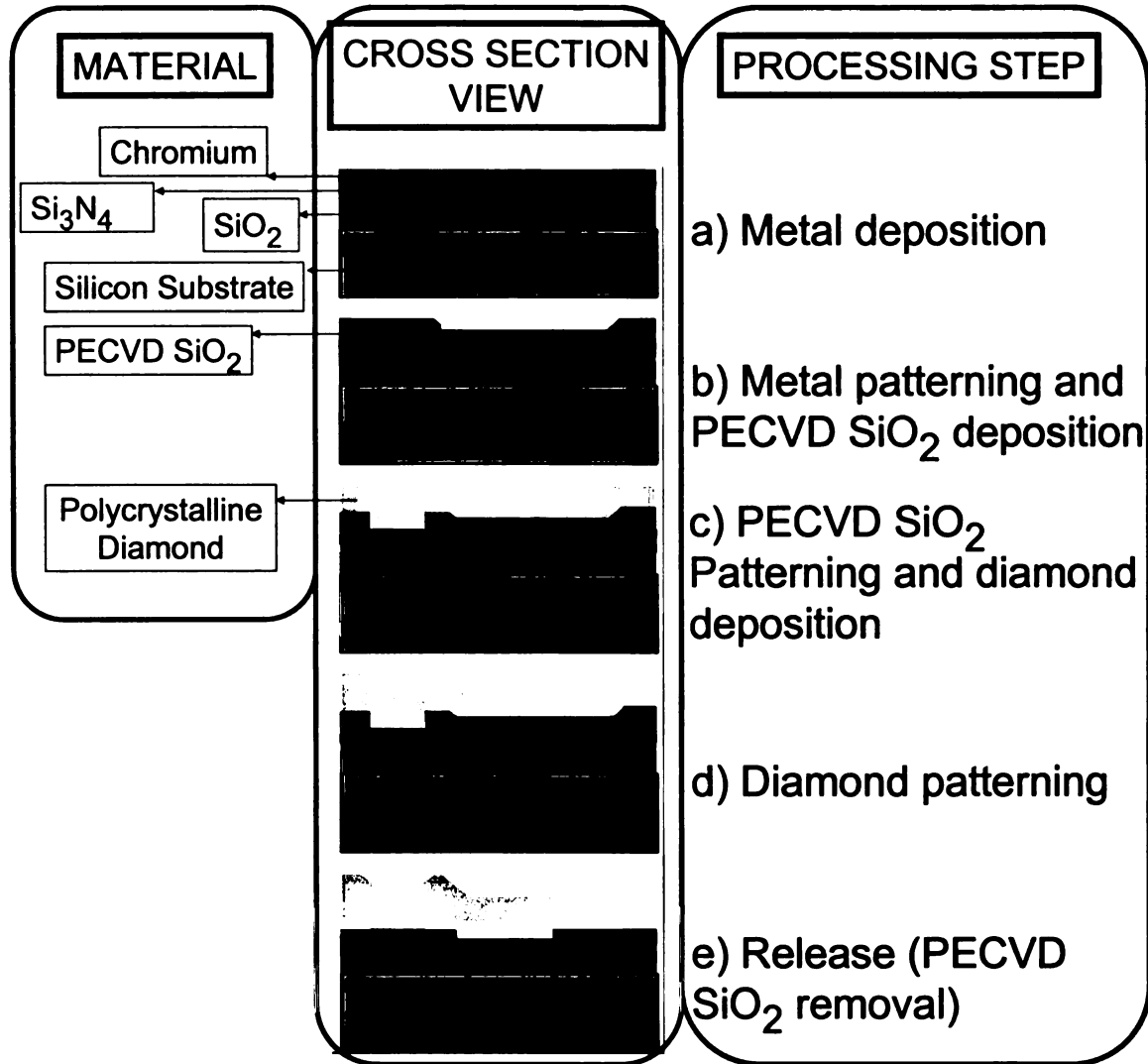


Figure 3.8 Fabrication process flow for electrostatically tested resonators

After this metal layer was deposited and patterned, it follows to deposit the material that will serve as a sacrificial layer. In this work, SiO₂ was deposited via PECVD and used as the sacrificial layer.

This layer will be removed entirely at the last step of the process (releasing step). The thickness of this layer will dictate the electrode to resonator gap. The gap value used in this work is 200 +/- 100nm. This range of values is very crucial for the electrostatic operation of polycrystalline resonators. As the gap increases, the *electromechanical transduction factor* (η) discussed in chapter 2 decreases. When this factor decreases, the output current also decreases, limiting the detection capability. If it is too thin, it can get completely etched away by the plasma in the diamond growth step, leaving a short circuit between the beam and the bottom electrode. A thickness around 200 nm has been successfully used in the past [81]. After this sacrificial layer has been deposited, it has to be patterned to create the contact areas where the resonator will be in contact with the metal layer underneath (mask #2). These areas are commonly called “anchors”. Once the anchors are patterned, the sample is ready for diamond seeding and growth (sections 3.3 and 3.3). A device that will be tested using electrostatic techniques needs to be conductive. For achieving this, *in situ* doping was done (section 3.4). For patterning the diamond (mask #3), dry etching was used (section 3.5). After the diamond film has been patterned, the exposed areas of the sample are SiO₂ and diamond. Now the devices are ready for releasing. In the release step, the purpose is to remove the entire sacrificial SiO₂ layer. This is done by submerging the sample in a 5:1 BHF solution (5 40% NH₄F :1 49% HF). This solution typically etches the PECVD SiO₂ at a rate between 250 nm/min and 500 nm/min [82]. The time that it will take for the solution to remove entirely the sacrificial layer depends on how large is the area under the resonator structures. This

etching solution (5:1 BHF) is isotropic. Therefore, if a 10 μm wide cantilever needs to be released, it will take the solution at least 20 minutes to etch 5 μm from each side and completely release the structure. If a faster releasing is desired, a solution with higher HF concentration can be used or even pure HF (49% by weight, remainder water). Both etching solutions remove the aluminum that was used to mask the diamond.

If the Si_3N_4 layer was not deposited, the SiO_2 etching solution (BHF or HF) will etch parts of the 2 μm thick thermal SiO_2 that came with the starting substrate. If this happens, the corner areas of the metal interconnect layer, which in this case would be over the thermally grown SiO_2 layer, would be partially released as well. This could lead to metal peeling off. Also, the undercutting of this metal layer will affect the resonator Q since the rigidity of the anchor can be affected. The Si_3N_4 isolates the thermally grown SiO_2 from the sacrificial PECVD SiO_2 in the release step, which avoids this problem and also gives more flexibility for the releasing time.

3.7.1.2 Samples for piezoelectric/optical testing

The fabrication process for a micromechanical resonator that is going to be tested using piezoelectric actuation and optical detection is much simpler. There are fewer processing steps and restrictions on the design. These include:

- 1) The underlying electrode required by the electrostatic method is not necessary.
- 2) The material does not need to be doped
- 3) The resonator gap is not critical.

Figure 3.9 shows the fabrication process flow for devices to be used using piezoelectric actuation and optical detection. Since there will be no current flow across the resonator and no time varying capacitance needs to be formed, metal electrodes are not necessary and the resonator does not need to be conductive. Since there is no capacitance formed or *electromechanical transduction factor* (η) to keep high, the gap between the beam and the substrate is not critical. In this work, the 2 μm thick SiO_2 layer that comes with the commercially available sample (figure 3.7) was used as the sacrificial layer. This would lead to a resonator to substrate gap of 2 μm .

The fabrication consists of a two mask fabrication process. The processing for a micromechanical resonator that will be tested using piezoelectric actuation and optical detection starts with the standard RCA cleaning of the substrate. Then mask #1 is used to pattern the thermally grown SiO_2 layer that comes with the starting substrate and form the anchors. Now the sample is ready for diamond seeding and growth (sections 3.2 and 3.3). The second and final mask is used to pattern the material (aluminum for purposes of this thesis) that will be used to mask and pattern the diamond (section 3.5).

The releasing step is the same used for the releasing of devices for electrostatic testing. The difference is that now the sacrificial thermal SiO_2 (wet grown) etches at a much slower rate in the BHF solution (100 nm/min) than the PECVD SiO_2 . Therefore, the releasing time will be longer. It will now take at least 50 minutes to completely release a 10 μm wide cantilever beam.

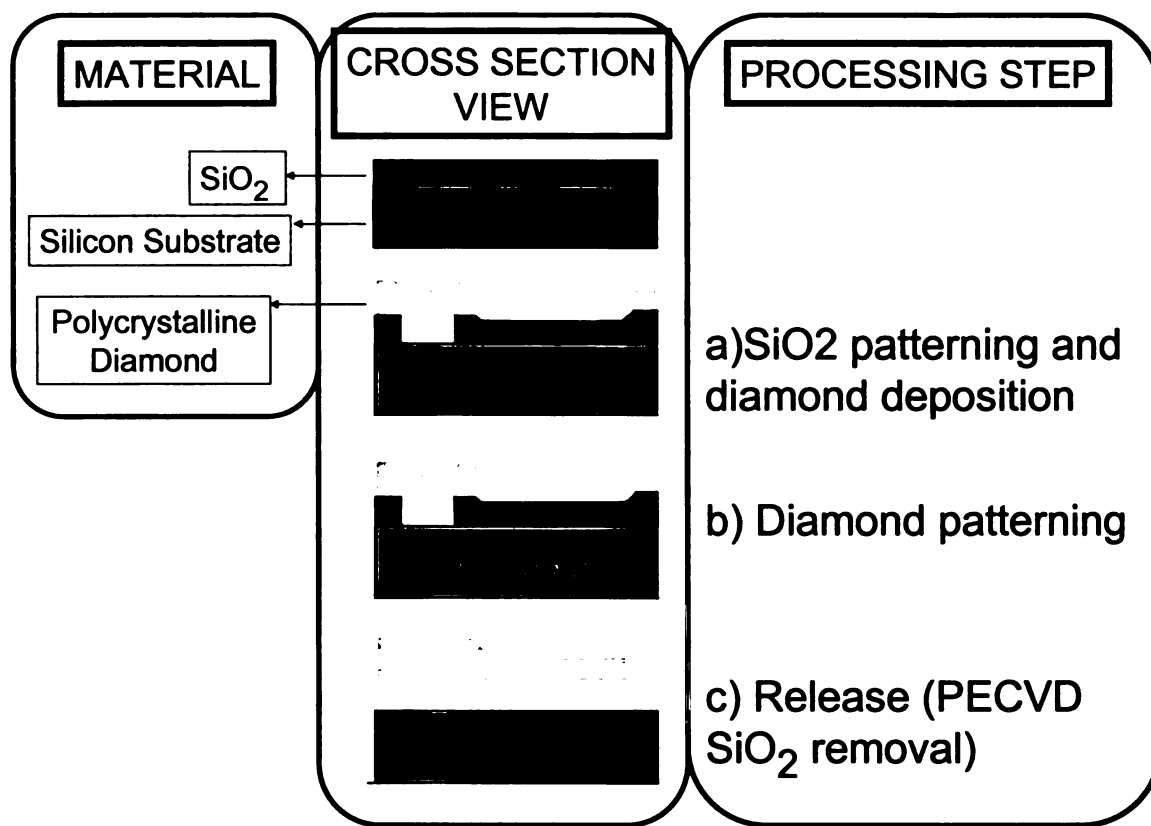


Figure 3.9 Fabrication process flow for resonators to be tested using piezoelectric actuation and optical detection

3.7.2 Post-processing

After the samples are released, some cleaning and drying steps were made. The samples that were tested at Michigan State University (tested electrostatically) could not go through standard RCA cleaning or any other cleaning process that involved hydrogen peroxide (piranha cleaning for example). This is because the metal layers present in such samples could suffer oxidation or be removed. After the sample was released, it was submerged in acetone for 5 minutes, then rinsed in a beaker with running DI water for 5 minutes and then submerged in methanol for 5 minutes. Since there might be released diamond spikes to be removed, the sample was then rinsed again with running DI water

for about 10 minutes. Finally, the sample was then heated in a hot plate to 100 °C and then annealed to 500 °C in a nitrogen environment for removing any moisture.

The samples that were processed and tested at Sandia National Laboratories (piezoelectric actuation and optical detection) went through a different post processing. After the sample was released, it was taken into an ultraviolet ozone cleaning system to remove the organic residues, and finally it was heated to 800 °C in an argon atmosphere using rapid thermal annealing to remove any residual moisture.

Chapter 4

Resonator Testing Methods

4.1 Introduction

As it was explained in chapter 2, there are several methods for testing micromechanical resonators. In this thesis, two different techniques were used to test similar resonator structures. The two methods used are the electrostatic testing and the piezoelectric actuation with optical detection.

4.2 Electrostatic Testing

This section describes the equipment set-up for the electrostatic testing system and the measurement results of polycrystalline diamond resonator structures. The equipment for electrostatic actuation was set-up at Michigan State University for the first time.

4.2.1 Electrostatic testing equipment set-up

Figure 4.1 shows a diagram of the testing system and the connections to the resonator structure. The system consists of a Low Temperature Microprobe vacuum chamber supplied by MMR Technologies capable of reaching a vacuum level of 10 mtorr. The chamber had four probes with electrical connections to the outside of the chamber by SMA (Sub-Miniature A) connectors. By using these SMA connectors, the network analyzer and the dc-voltage supply were connected to the probes inside the chamber and consequently to the resonator structure. The network analyzer was used to

supply the input ac signal and to constantly monitor the output current. A bias tee was used to isolate the dc-bias from the network analyzer. As soon as the beam starts vibrating, a change in the output current flow will be detected by the spectrum analyzer and it will show a maximum value at the resonant frequency. For purposes of this work a Hewlett-Packard/Agilent 8753B Network Analyzer (300KHz – 3GHz) was used. The dc-voltage supply was used to apply the dc-bias needed in order to increase the output current and get a more noticeable peak. A more detailed explanation of the theory involved in electrostatic testing can be found in section 2.2.3.1.

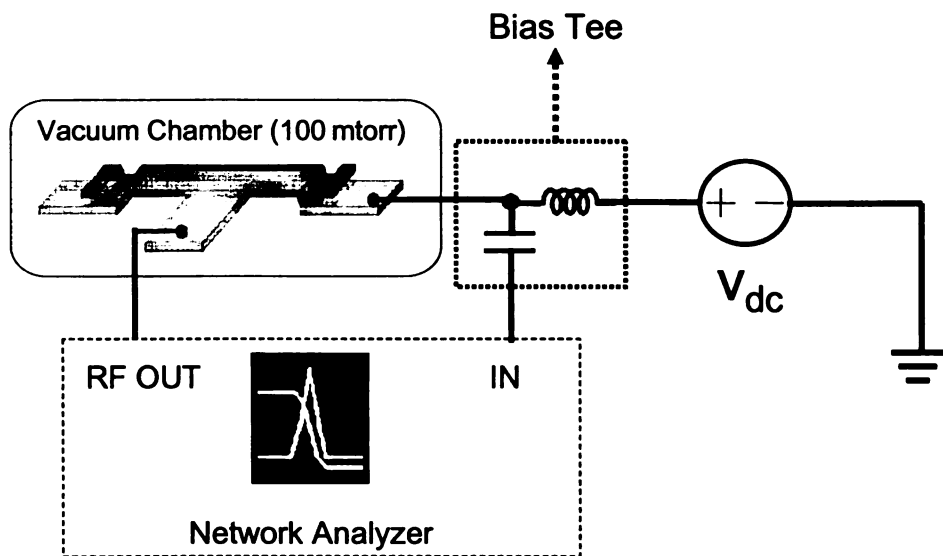


Figure 4.1 Connections to the resonator structure for electrostatic testing. In order to measure only the change in current across the resonator, a bias tee is used to isolate the dc- bias from the IN-port of the network analyzer.

4.2.2 Electrostatic testing measurement results

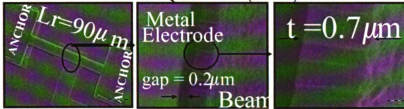
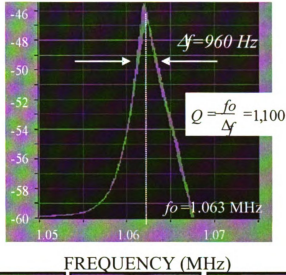
Different resonator structures were tested electrostatically. The results obtained were on bridge, comb-drive and cantilever resonator structures tested at a vacuum level

of 100 mtorr. Figure 4.2 shows the measurement results for a bridge and comb-drive structure tested using a dc-bias voltage of 30 V and SEM images of the tested structures. It can be noticed how the resonant peak shows a slight non-symmetry with respect to the resonant frequency point. This could be due to a non-linear effect caused by over driving the resonator structure. This problem has been found in the past by Kaajakari [83].

a)

$|S_{21}|$

(dB)



b)

$|S_{21}|$

(dB)

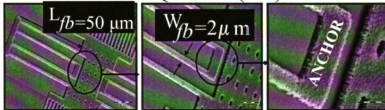
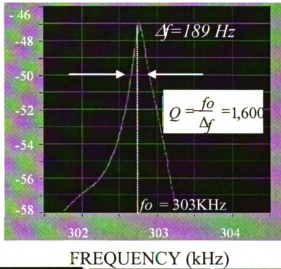


Figure 4.2 Electrostatic measurements on polycrystalline diamond resonators: a) bridge structure, b) comb-drive. The resonant frequency (f_0) was calculated by finding the frequency at maximum magnitude and the Q was calculated using this f_0 value and the 3dB bandwidth (Δf)

4.3 Piezoelectric actuation with optical detection

The piezoelectric actuation and optical detection was done using the measurement system that was already built at Sandia National Laboratories. The basic idea of the piezoelectric actuation method is to drive the resonator into vibration by using a piezoelectric transducer, which is in contact with the sample that contains the resonator structure. This piezoelectric transducer is driven into vibration at a frequency determined by the output of a network analyzer. For the optical detection, a laser is focused on the vibrating beam and the reflected signal is used to determine the frequency of vibration. A more detailed explanation is given in section 2.2.3.2.

4.3.1 Piezoelectric actuation and optical detection results

The tested structures were cantilevers and torsional resonators. The cantilevers reported in this section had lengths ranging from 50 μm to 100 μm , and they all had a width of 10 μm . The thickness varied from 0.45 μm to 0.7 μm . The table 4.1 summarizes the set of results obtained for these cantilevers made from the sample 1 described in chapter 3.

Researchers have found different values for the Young's modulus of polycrystalline diamond at room temperature [84]. The Young's modulus of the polycrystalline diamond resonators fabricated and tested was checked using the data shown in Table 4.1 and the following equation for the resonant frequency of a cantilever [10].

$$f_O = 0.1615 \sqrt{\frac{E}{\rho}} \frac{h}{L_r^2} \quad (4.1)$$

Table 4.1 Results for piezoelectrically-actuated cantilever beams (first vibration mode) made from sample 1.

Cantilever Length (μm)	Performance	
	f_o (Hz)	Q
100	258,900	9,970
95	276,400	7,540
90	325,500	14,470
85	346,300	10,070
80	384,900	15,260
75	443,500	8,240
70	503,800	6,390
65	570,900	3,550
60	654,300	5,390
50	856,500	6,726

where E and ρ are the Young's modulus and density of polycrystalline diamond respectively. The constants L_r and h are the beam length and thickness respectively.

Figure 4.3 shows a plot of the data shown in table 4.1. Since the plot in figure 4.3 shows the frequency (f_o) on the y-axis and the inverse of the cantilever length squared ($\frac{1}{L_r^2}$) in

the x-axis, equation (46) can be fit with a linear equation by taking $x = \frac{1}{L_r^2}$, $y = f_o$

and $m = 0.1615 \sqrt{\frac{E}{\rho}} h$. This would lead to:

$$\underbrace{f_o}_y = \underbrace{0.1615 \sqrt{\frac{E}{\rho}} h}_m \underbrace{\left(\frac{1}{L_r^2} \right)}_x \quad (4.2)$$

The Young's modulus can be calculated by using the expression for the slope

$$m = 0.1615 \sqrt{\frac{E}{\rho}} h.$$

The linear fit to the data shown in figure 4.3 shows a slope (m) of $0.002 \text{ Hz-}\mu\text{m}^2$.

The value for the film thickness (h) can be approximated from the SEM images to be 0.7

μm and the value for ρ is commonly know to be 3520 kg-m^{-3} . Since the variables h , ρ ,

and m are known, the Young's modulus for the polycrystalline diamond film (E) was calculated to be $1,000 \text{ GPa}$. This value is close to the accepted value of the Young's modulus for bulk single crystal diamond, which is about $1,050 \text{ GPa}$ [85]. The inset in figure 4.3 shows the resonant peak of the $95 \mu\text{m}$ long cantilever beam.

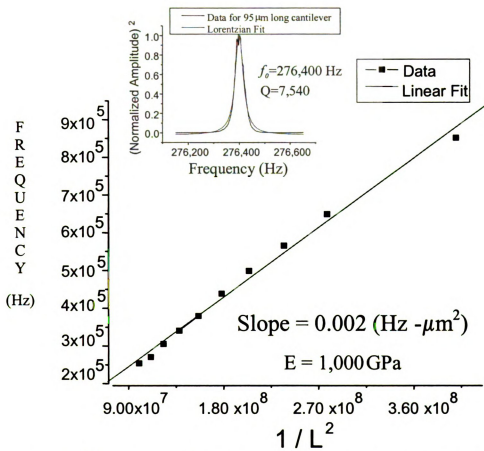


Figure 4.3 Young's modulus of sample 1 was calculated from a linear fit done to the measured data.

4.4 Comparison of results

Polycrystalline diamond cantilever beams were tested using both methods in order to compare the resonator performance. The cantilever beams that were tested using both methods came from polycrystalline diamond films grown at 780 °C. The sample tested electrostatically came from a highly doped ($5 \times 10^{19} \text{ cm}^{-3}$) polycrystalline diamond film. Table 4.2 shows the polycrystalline diamond film growth parameters for the sample tested using electrostatic and piezoelectric actuation.

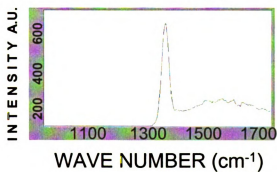
Table 4.2 Polycrystalline diamond growth parameters for the sample tested electrostatically and piezoelectrically

Polycrystalline Diamond Film Growth		
Gas Flow Rate (sccm)	Sample	
	Electrostatic	Piezoelectric
H₂	100	100
CH₄	1	1
TMB	4	0
Temperature (°C)	780	780
Microwave Plasma Power (kW)	2.0	2.0
MPCVD Gas Pressure (torr)	35	35
Seeding Diamond Powder Size (nm)	25	25

The seeding process was the same for both samples. For the sample used in electrostatic actuation, the gap between the structure and the bottom electrode was 0.2 μm , while for the piezoelectrically actuated the gap spacing was 2 μm . Figure 4.4 shows the Raman spectra of both samples. It can be seen that the doped sample has a higher background at higher wavenumber. This probably is due to fluorescence noise [86].

a)

Raman



b)

Raman

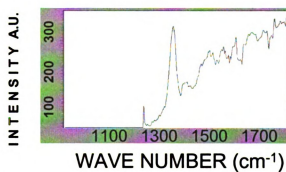
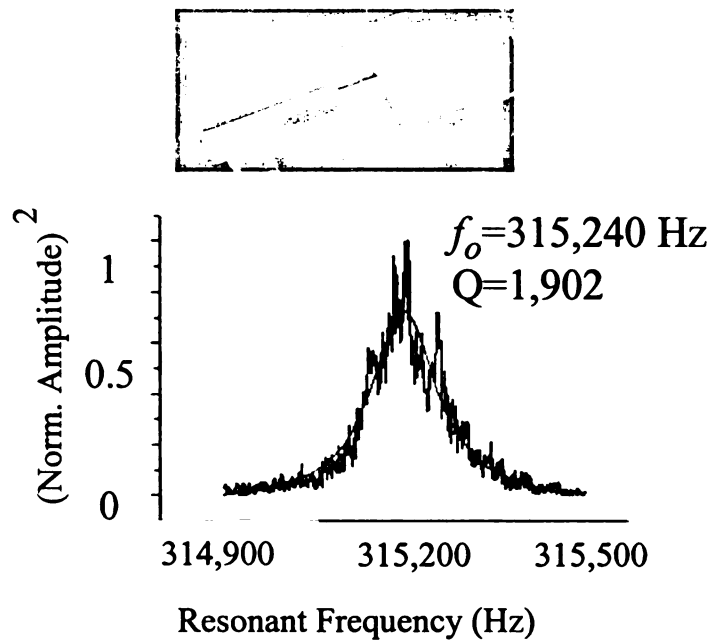


Figure 4.4 Raman spectra for samples measured using different actuation methods: a) piezoelectric b) electrostatic

Figure 4.5 shows the comparison of two cantilevers with the same length (90 μm) and tested using the two different testing methods. Although the difference in resonant frequencies of the two samples is on the order of 3%, the Q for piezoelectric actuation is 8 times higher than that for electrostatic actuation. The most likely reason for the decrease in resonance frequency for the electrostatically actuated beam could be the effect of an electrical spring constant k_e that subtracts from the mechanical spring constant of the beam, k_m , lowering the overall spring stiffness $k_r = k_m - k_e$ [11]. The dc-bias voltage used for this measurement was 5 volts. The gap spacing was 0.2 μm , the electrode and beam overlap was 20 μm and the beam length and width were 90 μm and 10 μm respectively. This gives rise to a $\left\langle \frac{k_e}{k_r} \right\rangle$ ratio of 0.045. This ratio means that the measured resonant frequency of this device using electrostatic actuation will be (theoretically) 95.5% of the resonant frequency that would be measured using a testing method which does not affect the resonator spring constant. The resonant frequency measured using electrostatic actuation was 315,240 Hz which is 96% the resonant frequency measured using piezoelectric actuation and optical detection (325,560 Hz). Another possible reason for the difference in frequency is a film thickness difference between the two polycrystalline diamond films from which the resonators were fabricated.

a) Electrostatic Actuation



b) Piezoelectric Actuation

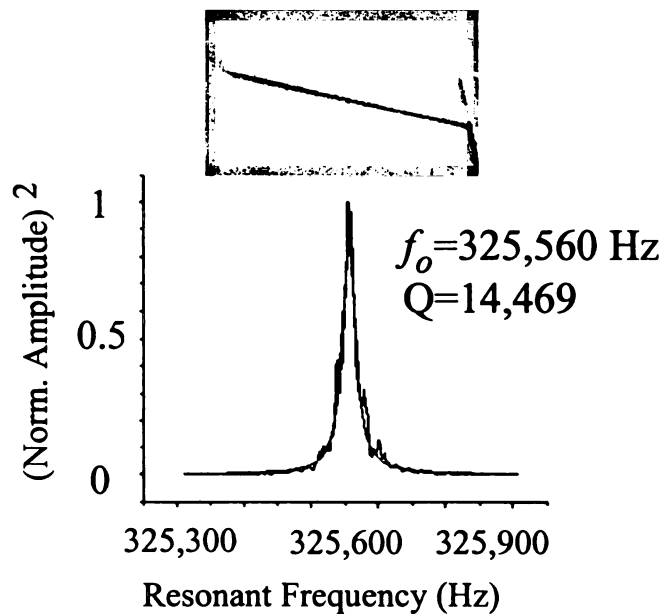


Figure 4.5 Testing results on two similar polycrystalline diamond cantilevers using different actuation and detection methods.

Also, although both films were fabricated under similar conditions (table 4.2), their thickness could still be slightly different due to possible fluctuations in temperature at the polycrystalline diamond growth step.

The difference in Q is likely not related to the method of actuation or the properties of the polycrystalline diamond film, but rather due to the different measurement pressures used in the two methods, 100 and 0.001 mtorr for electrostatic and piezoelectric actuations, respectively. The pressure of 100 mtorr reflects a low vacuum and, thus, represents what would be readily achievable in a packaged device [87]. At 0.001 mtorr there should be negligible air damping, and the Q should reflect the true mechanical Q of the structure. The effect of air damping on Q can be readily estimated. At 100 mtorr, the Q is limited by the exchange of energy between the mechanical structure and gas molecules. This is in the molecular flow regime, and the magnitude of Q can be calculated according to the following equation [22]:

$$Q = \frac{2\pi f_n h \rho}{k_m P} \quad (4.3)$$

where f_n is the resonance frequency of the n^{th} vibrational mode, ρ is the density, P is the gas pressure, and $k_m = [(32M)/(9\pi RT)]^{1/2}$, where M is the molecular weight of the gas, R is the gas constant, and T is the temperature.

The molecular flow regime extends down to about 10 mtorr, and below this point air damping is negligible. Therefore, decreasing the pressure from 100 mtorr to pressures less than 10 mtorr should result in an increase in Q of about a factor of 10. For the cantilever structures tested using electrostatic and piezoelectric actuation, the measured Q values were in the range of 1,000-2,000 and 3,550-15,260 respectively. The low quality

factors of the electrostatically structures are consistent with the Q being limited by air damping, and the quality factors of these structures are representative of what can be achieved for structures of these dimensions in a low vacuum package [87]. The piezoelectrically-actuated structures in high vacuum should not be limited by air damping.

Similar resonator structures also made from polycrystalline diamond were tested electrostatically under 50 mtorr by Wang [31]. Their reported Q values range from 2,000 – 6,000. Later results, also on similar polycrystalline diamond resonators tested electrostatically under 50 μ torr [32], showed Q values in the range of 6,225 – 36,460. Since the molecular flow regime extends down to about 10 mtorr, and below this point air damping is negligible, a decrease in pressure from 50 mtorr to any pressure below 10 mtorr would represent an increase of Q by a factor of 5. The results obtained in [31] and [32] show an improvement of Q close to a factor of 5 when the pressure in the chamber is lowered from 50 mtorr to 50 μ torr.

Based on the measured resonant frequencies and the dimensions of the structures, an acoustic velocity of $16,100 \text{ ms}^{-1}$ was found for the doped film and 15,900 for the undoped one. Assuming a density of $3,500 \text{ kg-m}^{-3}$, the resulting Young's modulus for the polycrystalline diamond films are 883 GPa for the doped sample and 907 GPa for the undoped one. The slightly lower moduli found here could be due to a slightly lower density for the polycrystalline diamond films or an error in the estimation in the polycrystalline diamond film thickness.

Chapter 5

Study of Q and Frequency Shifts in Polycrystalline Diamond Resonators

5.1 Introduction

Two very important characteristics of micromechanical resonators are resonant frequency and Q. This chapter discusses the Q and resonant frequency shifts due to varying testing temperature for polycrystalline diamond resonators. The data obtained during this study showed the measurement of the highest quality factor (116,000) for polycrystalline diamond resonators and for cantilever beams made of any polycrystalline material [33].

5.2 Quality Factor Limitations

As it was discussed in chapter 2, there are different mechanisms that can limit the Q. Figure 5.1 shows the effect of different energy loss mechanisms as a function of resonant frequency for polycrystalline silicon and polycrystalline diamond computed for a 1 μm thick cantilever beam. The corresponding cantilever beam length for each frequency and material appears on the top axis. The parameters used for plotting the dissipation curves [25] in figure 5.1 are shown in the Table 5.1. It is interesting to note that the increase of resonant frequency achieved by reducing the length of the beam leads to a substantial decrease in Q because the anchor losses are dominant mechanisms in the whole frequency range. In other words, Q can be substantially increased by minimizing anchor losses. However, in that case, the maximum achievable Q will be determined by

other energy loss mechanisms as shown in figure 5.1. As most applications require a Q of at least 10,000, the anchor losses will limit the frequencies to less than 10 MHz. Thus, for applications requiring frequencies above 10 MHz, if the clamping losses can be minimized, the losses due to other mechanisms will allow Q values of 10,000 as seen in figure 5.1.

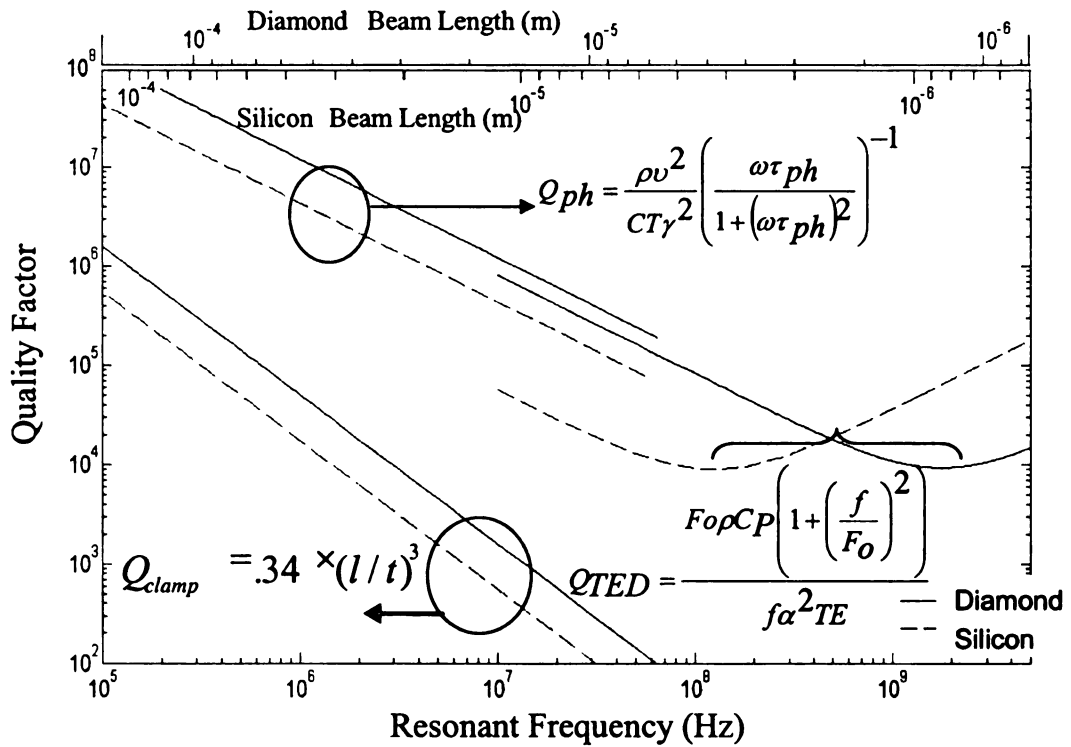


Figure 5.1 Energy loss mechanism curves for a 1 μm thick polycrystalline diamond and polycrystalline silicon cantilever beam

Table 5.1 Polycrystalline diamond and polycrystalline silicon properties used for plotting the dissipation curves in figure 5.1

Parameter	Polycrystalline Silicon	Polycrystalline Diamond
Thermal Expansion Coefficient, $\alpha (\times 10^{-6} \text{ }^{\circ}\text{C}^{-1})$	2.67	1.1
Young's Modulus, $E (\text{GPa})$	170	1,050
Density, $\rho (\text{kg m}^{-3})$	2329	3520
Specific Heat Capacity, $C_p (\text{J kg}^{-1} \text{K}^{-1})$	700	502
Heat Capacity per Unit Volume, $C (\text{J m}^{-3} \text{K}^{-1})$	1.63	1.767
Thermal Conductivity, $\kappa (\text{W m}^{-1} \text{K}^{-1})$	130	1500
Gruneisen's Constant, γ	1	1
Velocity of longitudinal and transverse sound waves in the material $v_l ; v_t (1 \times 10^3 \text{ ms}^{-1})$	9 ; 5.5	18 ; 13.1

5.3 Quality Factors in Polycrystalline Diamond Resonators

This section shows the results obtained for polycrystalline diamond cantilever beams with widths of 10 μm , and lengths and thicknesses varying from 100 μm - 500 μm , and 0.45 μm - 0.8 μm respectively. Piezoelectric actuation and optical detection was used as the testing method for all the results reported in this chapter. The samples were tested at a vacuum level of 1×10^{-5} torr. The performance of the resonators (frequency and Q) was obtained from the Lorentzian fits done to the obtained data. The frequencies of the tested resonators were all in the KHz range (8 KHz – 800 KHz), and the Q values varied significantly from sample 1, where a Q of 116,000 was obtained, to the other two samples (sample 2 and 3), where the Q values did not exceed 50,100.

Figure 5.2 shows some of the Q limiting curves in polycrystalline diamond resonators (solid lines) and the measured data (experimental points) on all the samples. These curves apply to a 0.7 μm thick polycrystalline diamond cantilever beam. The clamping curve does not depend on the cantilever temperature, and this is why figure 5.2

shows only one curve for clamping losses. The curves for Q_{TED} and Q_{ph} will be shifted in the y-axis by the cantilever temperature. Figure 5.2 shows 2 curves for each of these temperature dependent dissipation mechanisms. They are plotted to include the lowest and highest temperature at which the samples were tested (30 °C and 400 °C).

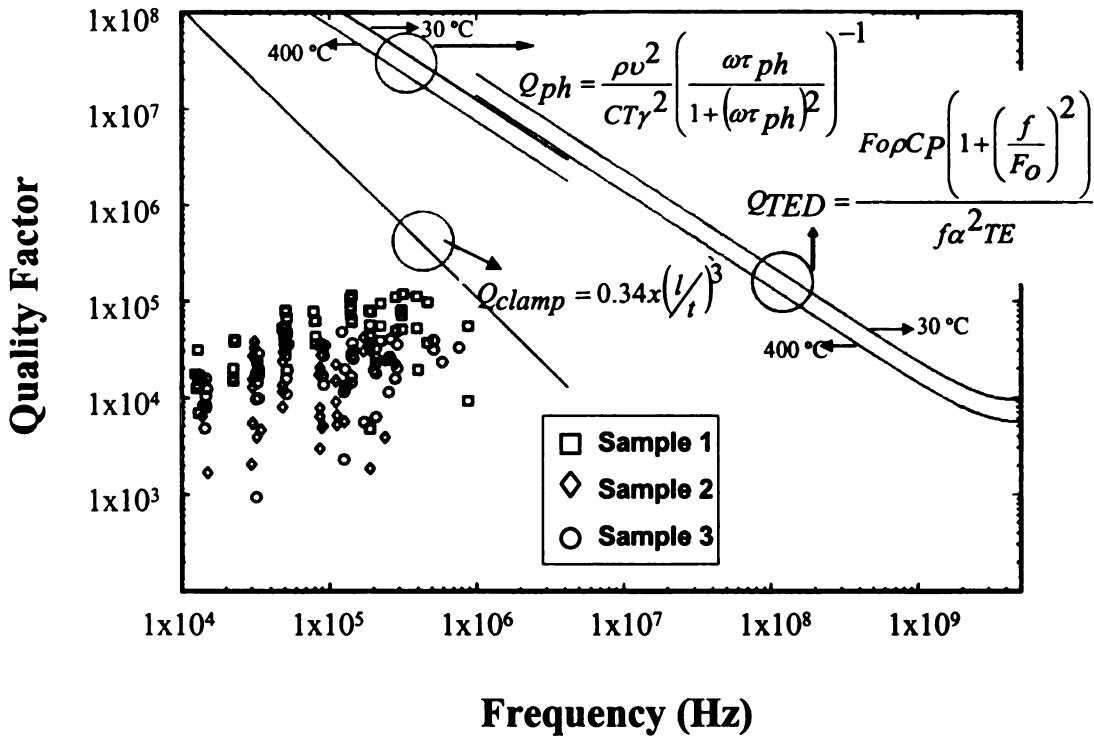


Figure 5.2 Q value limiting curves for a 0.6 μm polycrystalline diamond cantilever beam and measured data for the three samples.

All the Q factors measured in this work are below any of the dissipation curves, suggesting that the Q values are not limited by any of these mechanisms. The most likely mechanisms for limiting Q values in polycrystalline diamond are mechanical relaxation processes at defects in the films, such as vacancy or impurity motion, grain boundary sliding, etc [13]. A study of the temperature dependence of Q in polycrystalline diamond resonators together with the study of the polycrystalline diamond microstructure will allow a better understanding of these mechanisms.

Figure 5.3 shows a plot of the obtained Q values for the three samples (same experimental points shown in figure 5.2) in a range of frequency where the data can be observed clearly. It also shows the resonant peak with the highest Q value for each sample.

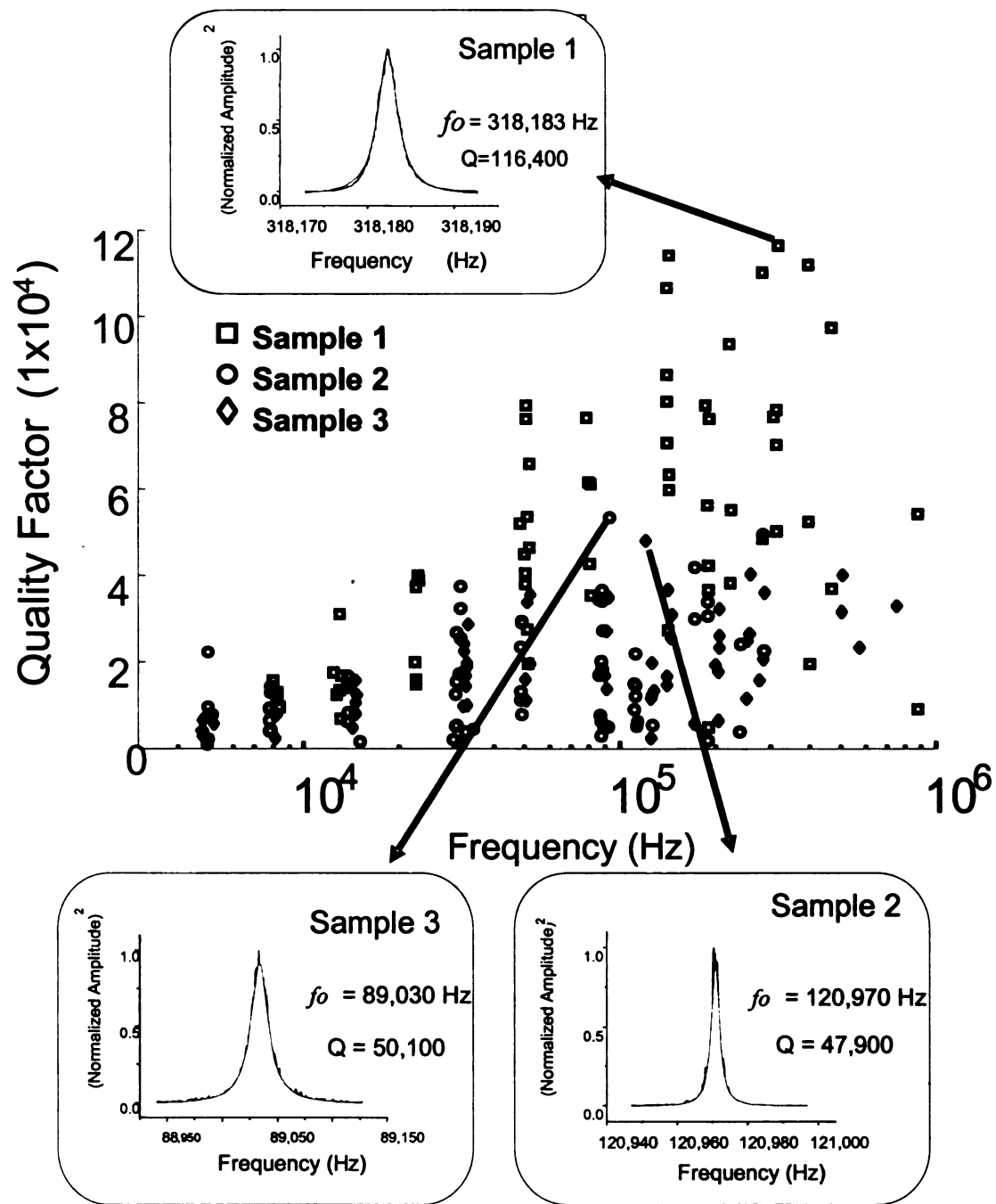


Figure 5.3 Measured Q values as a function of frequency for the three studied samples. Resonant peaks show the highest Q value for each sample.

5.4 Polycrystalline Diamond Film Microstructure

In order to characterize the different polycrystalline diamond films, TEM images of the cross sections from one piece of each sample were taken. The cross sections were obtained by using the focused ion beam (FIB) technique, which uses an ion beam to raster over the surface allowing the milling of small holes in the sample at well localized sites, so that cross-sectional images of the structure can be obtained. From the TEM images, the polycrystalline diamond film can be studied in more detail including the nucleation layer (*seeding* layer) that is necessary for polycrystalline diamond growth. This nucleation layer is typically formed of small grains (~30 nm in diameter).

Figure 5.4 shows how the grain sizes from the studied polycrystalline diamond films increases from the nucleation layer up, showing a larger percentage of the film composed of small grains for the sample 2. As the polycrystalline diamond films contain sp and sp^2 carbon-carbon bonds leading to non-diamond phases at the grain boundaries, their properties can be affected adversely in this nucleation layer. According to figure 5.3 the Q values are larger for the polycrystalline diamond film with less percentage of the film composed by the *seeding* layer (sample 1). This preliminary result suggests a relation between Q and the nucleation layer in polycrystalline diamond resonators. The characteristics of this nucleation layer (thickness, grain sizes, nucleation density, etc.) can be controlled by the growth process.

Polycrystalline diamond films can be divided into two layers: 1) The *seeding* layer and 2) The *film* layer.

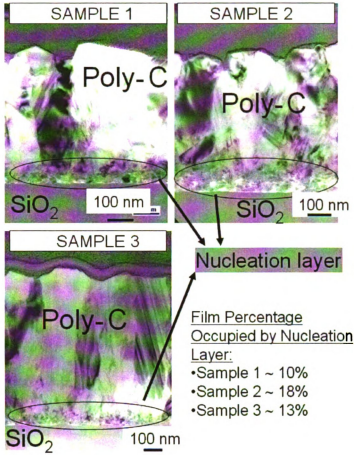


Figure 5.4 Cross section TEM images of the three studied polycrystalline diamond samples.

5.4.1 Seeding Layer vs. Film Layer

If a cantilever beam is treated as a two layer structure across its thickness [88], where the two layers are the *seeding* and *film* layer, the total dissipation can also be thought of as the combination of the dissipation in these two layers. In other words, the total dissipation in the cantilever beam would be partially due to the *seeding* layer, and partially due to the *film* layer. The total dissipation can then be expressed as [89]:

$$\frac{1}{Q_{tot}} = \frac{t_s / t_{tot}}{Q_s} + \frac{t_f / t_{tot}}{Q_f} \quad (5.1)$$

where t_s , and t_f , are the thicknesses of the seeding and film layer respectively and $t_{tot} = t_s + t_f$. The values $1/Q_s$ and $1/Q_f$, are the dissipation due to the seeding and film layer respectively, and $1/Q_{tot}$ is the total dissipation in the cantilever structure. The purpose of this analysis is to find if there is a common dissipation among all the polycrystalline diamond films (Samples 1, 2 and 3) due to the *seeding* layer $1/Q_s$ and another due to the film $1/Q_f$.

For this analysis, the values for t_s , and t_f were obtained directly from the TEM images. For estimating the Q_{tot} for each film, the arithmetic average of the 15 higher measured Q values of each sample was calculated. The 15 higher Q values for each sample were in the following ranges for each sample:

- 1) Sample 1: 76,560 – 116,000
- 2) Sample 2: 31,596 - 47,900
- 3) Sample 3: 23,544 - 50,100

The obtained values for t_s / t_{tot} , t_f / t_{tot} and the average of the 15 higher Q values for each sample ($\overline{Q_{tot}}$) are shown in table 5.2. Now that these variables are known, they can be substituted in equation (5.1) for each of the three films. The result of this substitution is shown in equations (5.2), (5.3), and (5.4).

Table 5.2 Ratio of seeding and film thickness to total thickness for each sample and the average of the 15 higher measured Q values for each sample ($\overline{Q_{tot}}$).

Sample/Parameter	t_s/t_{tot}	t_f/t_{tot}	$\overline{Q_{tot}}$
Sample 1	0.1	0.9	96,000
Sample 2	0.18	0.82	35,000
Sample 3	0.13	0.87	30,000

$$\frac{1}{96,000} = \frac{0.1}{Q_s} + \frac{0.9}{Q_f} \Rightarrow \text{Sample}_1 \quad (5.2)$$

$$\frac{1}{35,000} = \frac{0.18}{Q_s} + \frac{0.82}{Q_f} \Rightarrow \text{Sample}_2 \quad (5.3)$$

$$\frac{1}{30,000} = \frac{0.13}{Q_s} + \frac{0.87}{Q_f} \Rightarrow \text{Sample}_3 \quad (5.4)$$

Now, if equation 5.1 is rearranged in the following way

$$\frac{1}{Q_{tot}} = \frac{1}{Q_f} + \frac{t_s}{t_{tot}} \left(\frac{1}{Q_s} - \frac{1}{Q_f} \right) \quad (5.5)$$

the values for the Q_{tot} can be plotted as a function of t_s/t_{tot} and from the slope of a linear fit and the intercept in the y-axis, the values for Q_s and Q_f can be obtained. The resulting plot is shown in figure 5.5. From the slope and intercept values, the calculated Q_f and Q_s values are: $Q_f=66,000$ and $Q_s=4,737$

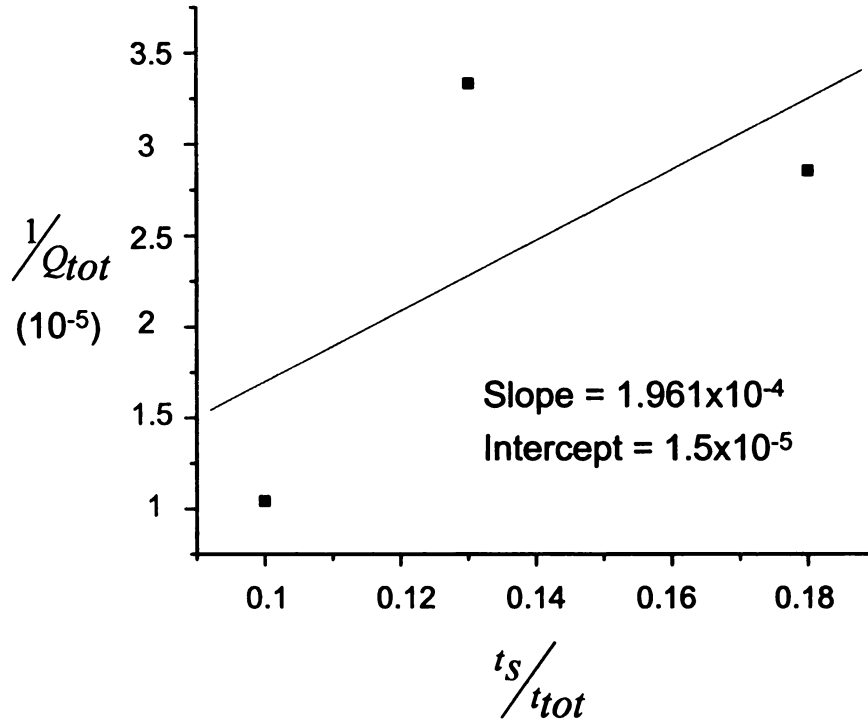


Figure 5.5 Plot of $1/Q_{tot}$ as a function of t_s/t_{tot} . The values for Q_f and Q_s are obtained from the slope and intercept of the linear fit.

Another way to find the range of values for Q_f and Q_s , would be to plot the Q_f as a function of Q_s by using the functions shown in equations 5.2-5.4 and then approximate the minimum space which contains a set of values for Q_f and Q_s which satisfy each of the equations in the system. One possible way and find this minimum area or space of solution is to find a rectangle that contains at least one set of values for Q_f and Q_s , which belong to each of the curves. This is similar to what was done by [90] and [91]. The horizontal line that would describe this rectangle (*HOR*) is the difference in Q_s from

sample 1 and sample 3. The vertical line that would describe this rectangle (*VER*) is the difference in Q_f from sample 1 and sample 3. Using equations (5.2) and (5.4), these lines can be taken as:

$$HOR = \frac{9,600Q_f}{Q_f - 86,400} - \frac{3,900Q_f}{Q_f - 26,100} \quad (5.6)$$

$$VER = \frac{86,400Q_s}{Q_s - 9,600} - \frac{26,100Q_s}{Q_s - 3,900} \quad (5.7)$$

In order to minimize the area of the rectangle, it would be necessary to minimize the product of equations (5.6) and (5.7). An approximation of this minimization was obtained graphically by plotting the product of equations (5.6) and (5.7) in terms of Q_s and Q_f and obtaining the values for Q_s and Q_f at which the area of the rectangle is minimum. Fig 5.6 shows a plot of the obtained rectangle. The range of values for Q_f and Q_s that are defined by the rectangle are:

$$\begin{aligned} Q_f &= 70,500 \pm 30,000 \\ Q_s &= 30,250 \pm 19,750 \end{aligned} \quad (5.8)$$

These values suggest that the Q of a polycrystalline diamond film consisting entirely of the seeding layer would be about 30,000 +/- 20,000 whereas a polycrystalline diamond film having no seeding layer would have a Q of about 70,000 +/- 30,000. The Q of a polycrystalline diamond film containing both a seeding layer and a film layer can be estimated using equation 5.1.

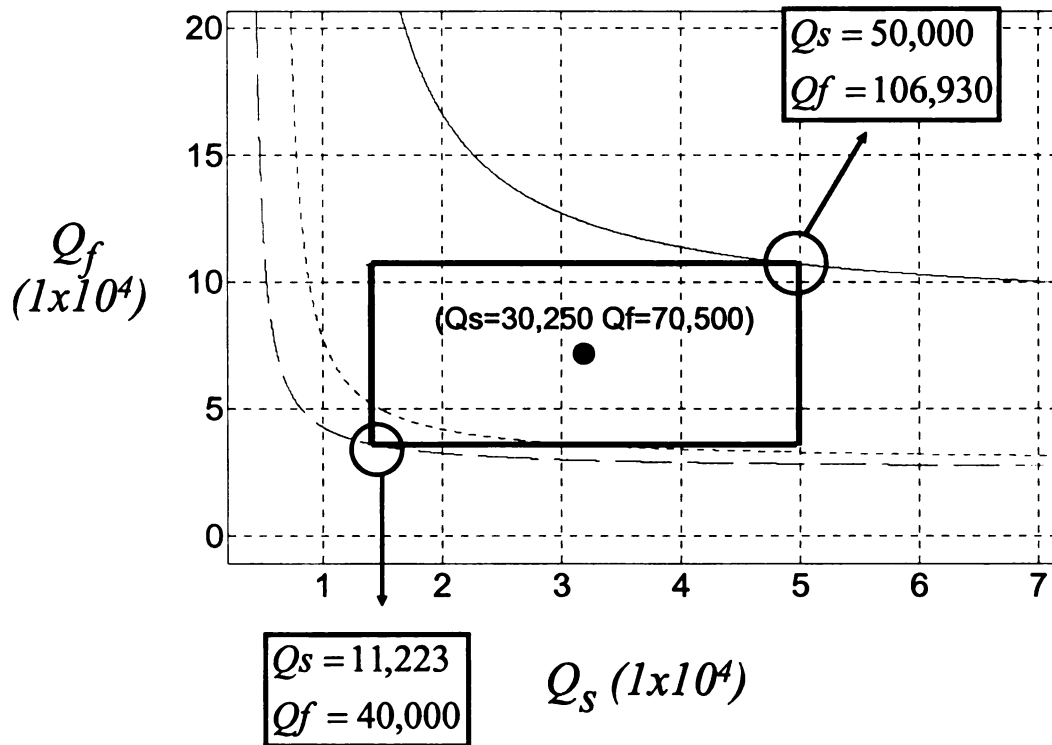


Figure 5.6 The approximation for the minimum space of solutions is determined by the rectangle, which touches all the curves at least in one single point.

5.5 Temperature dependence

It is important to guarantee the micromechanical resonator thermal stability in order to make the device suitable for high temperature applications. Since the elastic properties of most polycrystalline materials change at different temperatures, the performance of resonators made from such films also varies with temperature. Also, it is important to be able to predict the shift in resonant frequency of a mechanical resonator when the ambient pressure changes.

5.5.1 Young's modulus and frequency temperature dependence

As it has been pointed out earlier, for most resonators the frequency depends on the Young's modulus of the material the resonator is made of. Most polycrystalline materials have a temperature dependent Young's modulus. Consequently, there is a frequency shift on polycrystalline resonators when they are operated at different temperatures. The Young's Modulus of polycrystalline diamond decreases with temperature [92] and so does the frequency of resonators made of polycrystalline diamond.

In this work, cantilever beams made from the three different polycrystalline diamond films (described in section 3.3) were tested at different temperatures. The temperature dependence of the polycrystalline diamond Young's modulus was obtained from the measured frequency values at different temperatures and using a linear fit analysis similar to the one used in section 4.3.1. Figure 5.7 shows the variation of the Young's modulus for the three polycrystalline diamond films. In the studied temperature range (30 °C – 400 °C) the samples show a Young's modulus decrease of 2.5% (sample 1), 3.8% (sample 2) and 2.6% (sample 3).

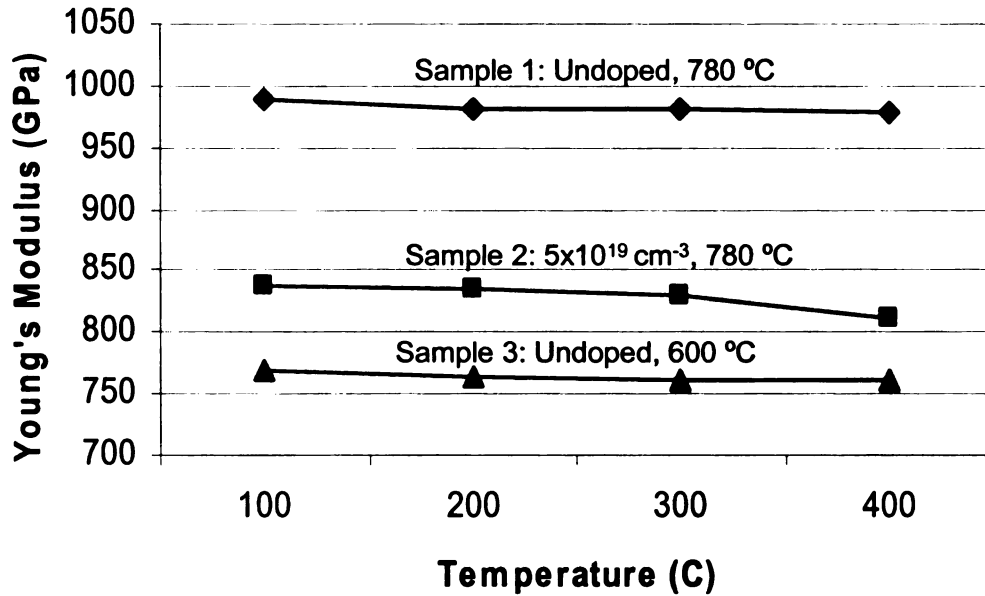


Figure 5.7 Young's modulus temperature dependence for the three samples. The three samples have very similar slopes and the sample 1 showed the highest Young's modulus at room temperature.

This decrease in Young's modulus is reflected in a resonant frequency shift of resonators made from these films. The shifts in resonant frequency due to changes in temperatures are measured by the temperature coefficient (TC_f). This temperature coefficient represents the resonant frequency shift in relation to the room temperature resonant frequency ($\Delta f / f_0$) by degree centigrade.

Figures 5.8 - 5.10 shows the frequency shift $\Delta f / f_0$ for 300 μm and 400 μm long cantilever beams made from the three different samples when operated in their first two flexural modes. The resonant frequency shift by degree centigrade was obtained by calculating the slopes of linear fits done to the measured data. The range of the obtained

temperature coefficients (TC_f) for the three types of polycrystalline diamond structures go from $-1.59 \times 10^{-5} \text{ }^\circ\text{C}^{-1}$ to $-2.56 \times 10^{-5} \text{ }^\circ\text{C}^{-1}$ ($-15.9 \text{ ppm}/^\circ\text{C}$ to $-25.6 \text{ ppm}/^\circ\text{C}$). These ranges are comparable to those obtained for poly-Si structures ($-12.5 \text{ ppm}/^\circ\text{C}$ to $-16.7 \text{ ppm}/^\circ\text{C}$) in a shorter temperature range ($30 \text{ }^\circ\text{C} - 247 \text{ }^\circ\text{C}$) [11], but are far from values obtained for geometrically compensated poly-Si structures ($-2.5 \text{ ppm}/^\circ\text{C}$ to $-0.24 \text{ ppm}/^\circ\text{C}$) [93,94] in a shorter temperature range ($30 \text{ }^\circ\text{C} - 107 \text{ }^\circ\text{C}$).

5.5.2 Quality factor temperature dependence

Most of the extrinsic internal dissipation mechanisms that cause Q degradation in polycrystalline materials are associated with atomic motion or with structural reconfiguration. The motion of vacancies or substitutional impurities, interstitial motions, dislocation, grain boundary sliding cause a resonant Debye-like relaxation, which limits the Q value according to the following equation [25]:

$$Q_{\text{defect}} = A \times \left[\frac{\omega \tau^*}{1 + (\omega \tau^*)^2} \right]^{-1} \quad (5.9)$$

where A is known as the “intensity” of the relaxation process, τ^* is the relaxation time for the defect motion and ω is the resonator vibrational angular frequency ($\omega = 2\pi f_0$). It can be noticed from (5.9) that when a defect is limiting the Q, then its value (Q_{defect}) will be minimum at $\omega \tau^* = 1$. Since there is atomic motion involved, τ^* is thermally activated and has the following functional form [25]:

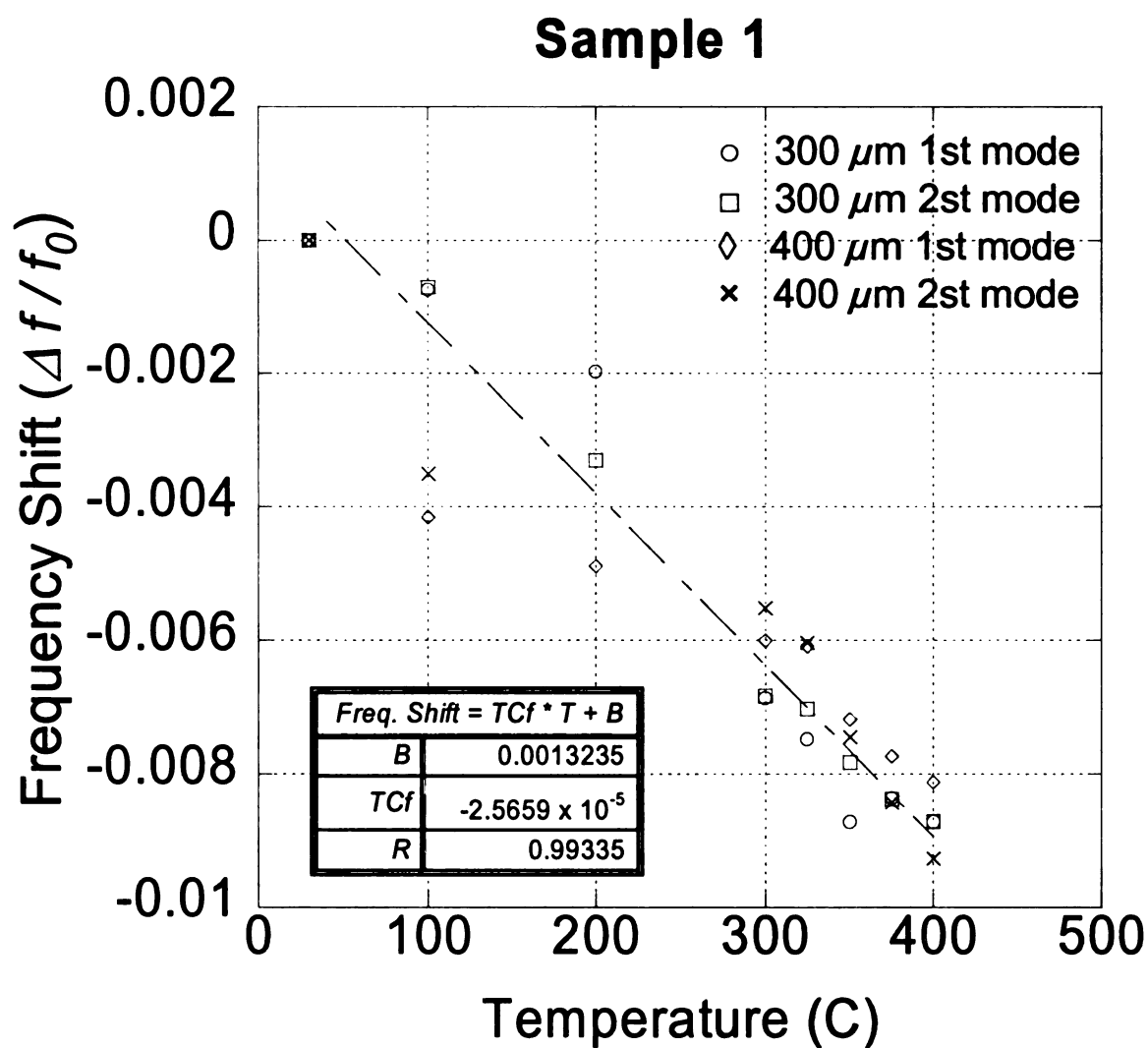


Figure 5.8 Frequency shift as a function of testing temperature for sample 1

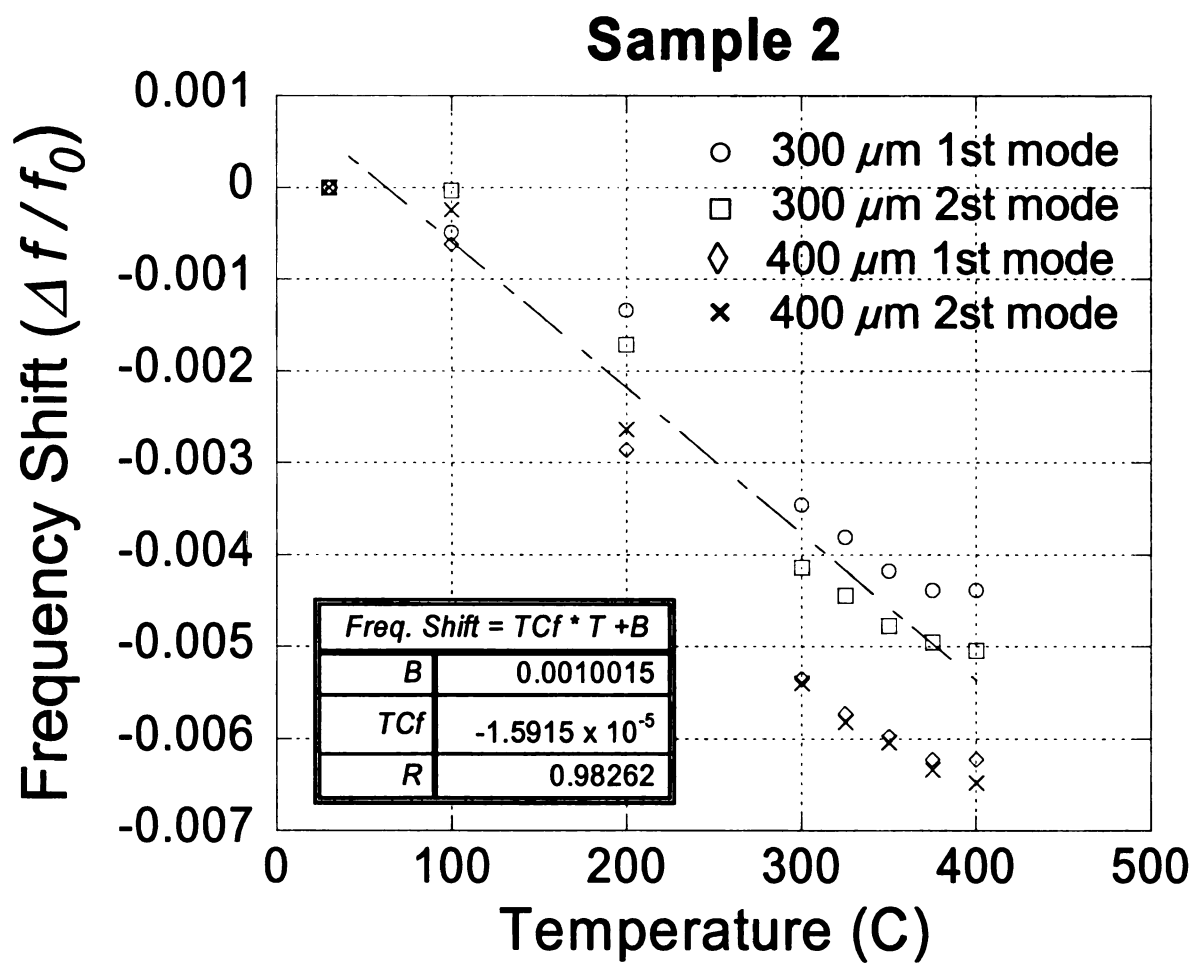


Figure 5.9 Frequency shift as a function of testing temperature for sample 2

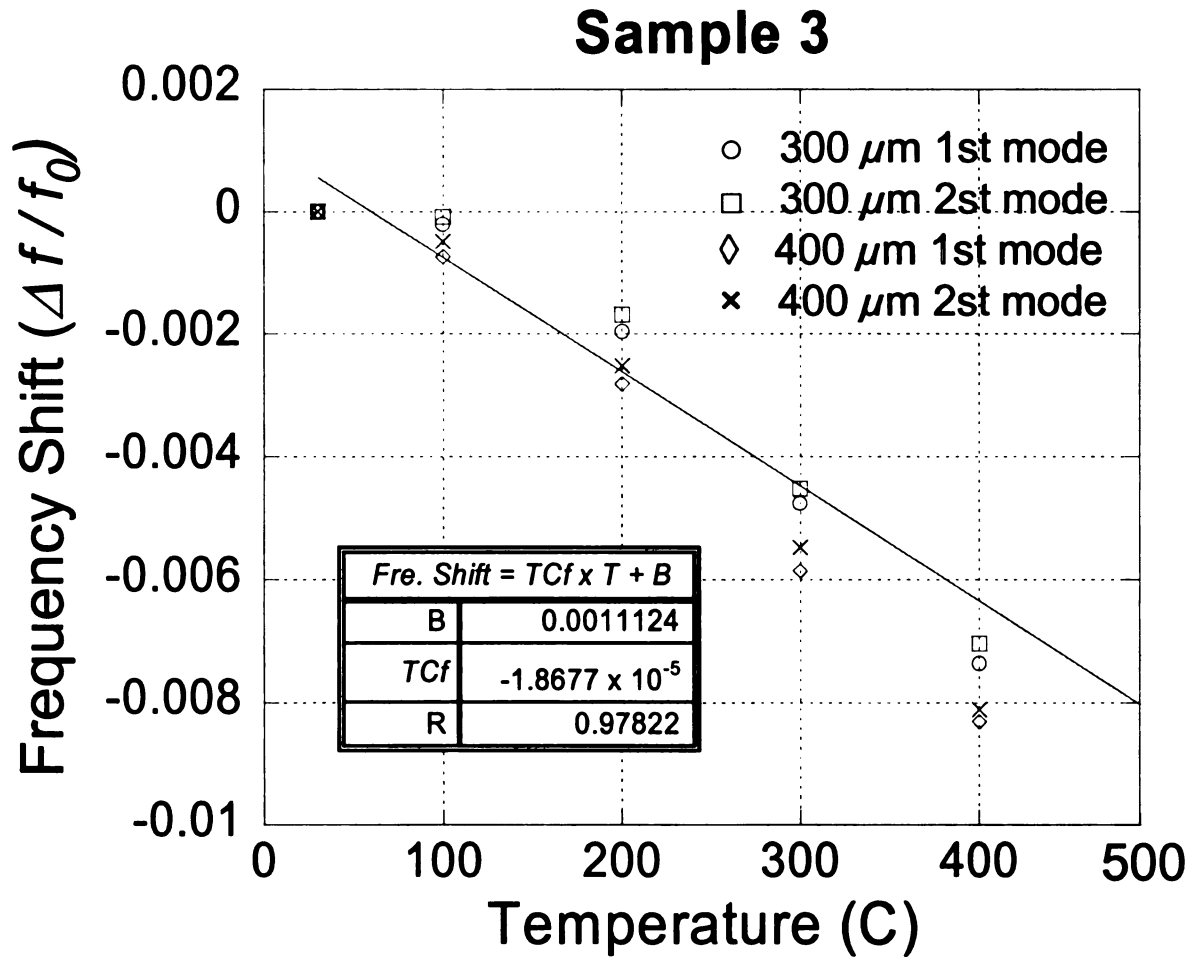


Figure 5.10 Frequency shift as a function of testing temperature for sample 3

$$\frac{1}{\tau^*} = \frac{1}{\tau_0} e^{\left(\frac{-E_a}{k_b T} \right)} \quad (5.10)$$

where $1/\tau_0$ is the characteristic atomic vibration frequency (on the order of 10^{13} Hz), E_A is the activation energy for the relaxation process, and k_B is the Boltzmann's constant. If a single defect type dominates, then there will be a maximum in internal dissipation (a minimum in Q) at the frequency in which $\omega\tau^* = 1$

The Q values of a resonator can be measured as a function of temperature. Then the activation energy for the relaxation process can be identified by finding the temperature at which the Q degradation is maximum and using equation (5.10). Figure 5.11 (a) shows the Q values as a function of temperature for the three samples. It can be noticed in figure 5.11 (b) how the Q values for the sample 2 reached a minimum value at around 350 °C. This suggests the presence of a thermally activated relaxation mechanism responsible to limit the Q in highly doped polycrystalline diamond resonators or at least the existence of a higher concentration of defects having an activation energy corresponding to the measurement temperature of 350 °C.

The data for the 3 samples was then plotted as a function of the activation energy by using (5.10). The activation energy axis was divided in ranges of 0.2 eV and the measured Q values for each polycrystalline diamond film that were inside each subdivision were averaged and represented by one single point. Figure 5.12 shows the results from this analysis, where it can be noticed – in addition to the higher Q values for sample 1 – the minimum in Q value for two of the three samples at an activation energy around 1.9 eV.

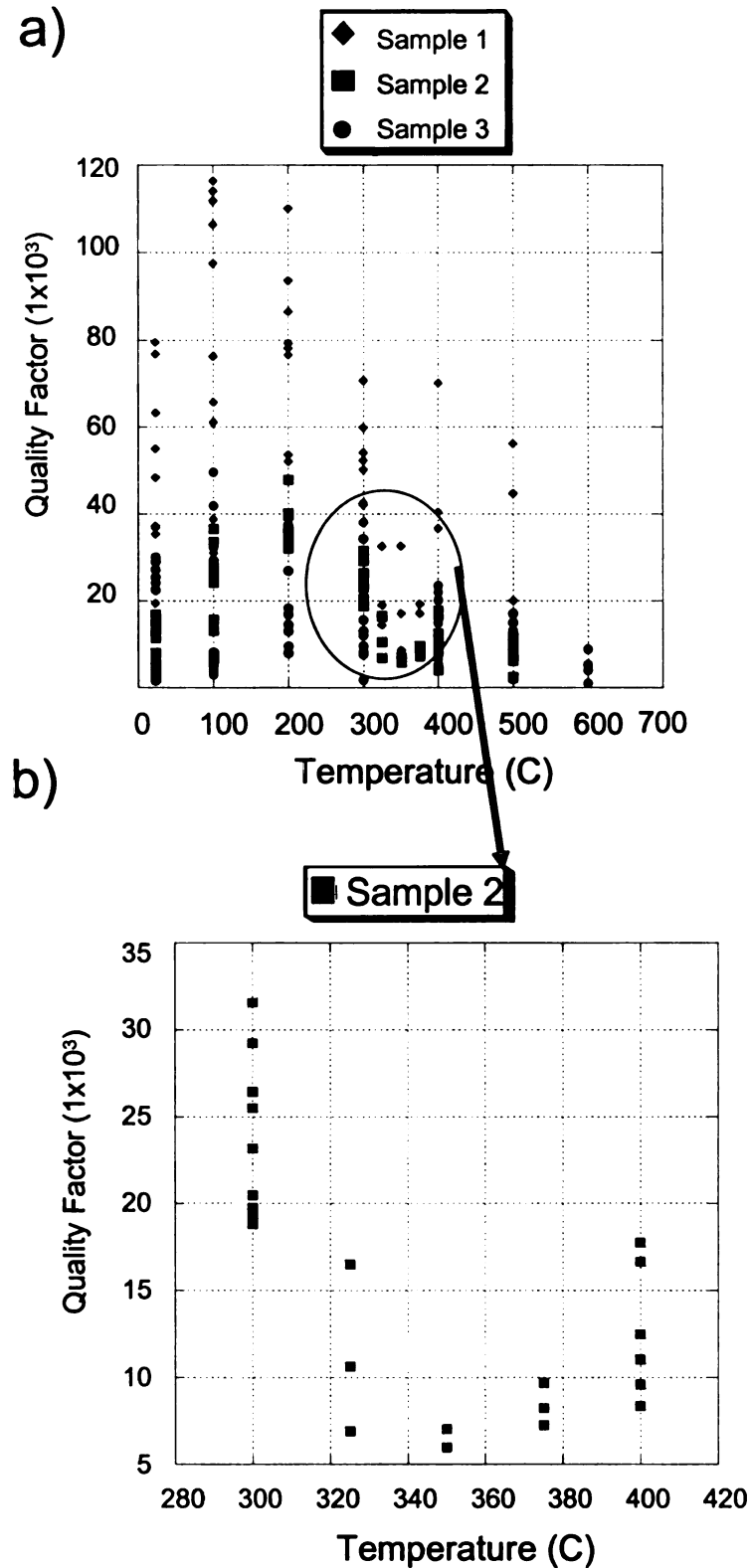


Figure 5.11 Measured Q values vs. temperature a) Three samples plotted in the entire testing temperature range; b) Sample 2 in the range of temperature where a minimum in Q was observed.

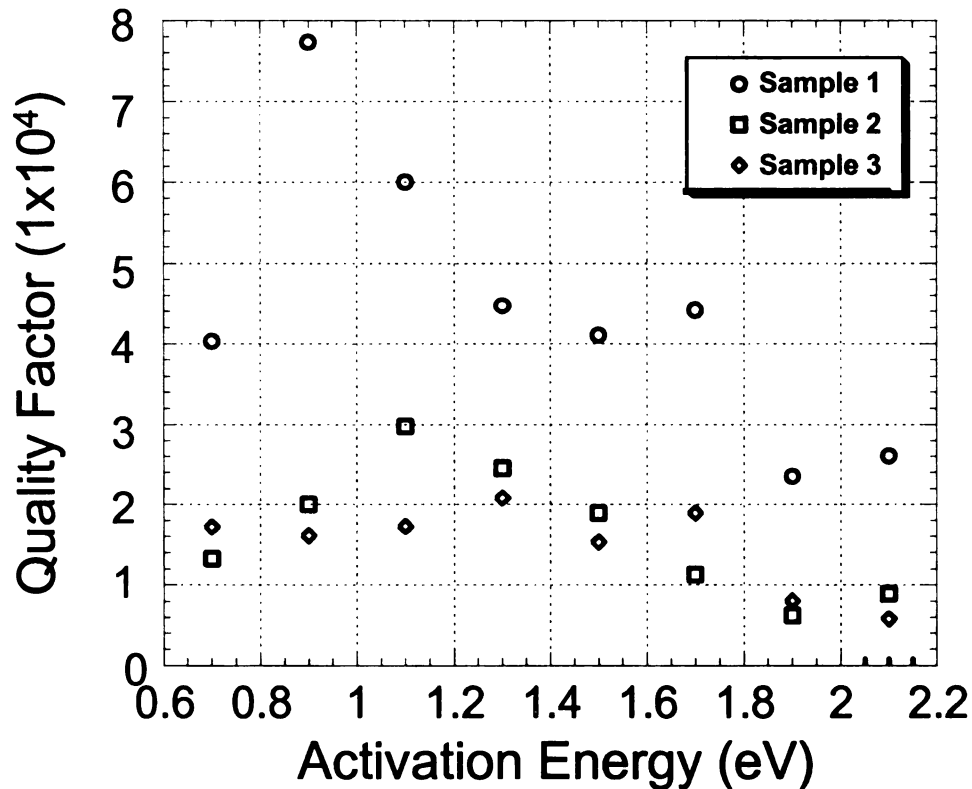


Figure 5.12 Measured Q values vs. activation energy for the three samples. A minimum in Q was observed for two of the three samples at an activation energy around 1.9 eV.

The data suggests there are some defects or a higher concentration of defects that give rise to mechanical relaxation that have an activation energy for defect relaxation around 1.9 eV. This activation energy can be compared to the activation energies for self-interstitial or vacancy diffusion in crystalline diamond (about 1.3 eV and 2.3 eV, respectively). A comparison to diffusional activation energies was made because many defect relaxation processes, e.g. grain boundary sliding, are limited by diffusional processes.

Chapter 6

Polycrystalline Diamond Nanoresonators

6.1 Introduction

This chapter reports on the fabrication technology and testing of polycrystalline diamond resonators with dimensions in the nanometer range (nanoresonators). These are the first fabricated and measured structures of this type reported. The fabricated and tested nanoresonators include torsional and cantilever structures.

6.2 Fabrication of Nanoresonators

Electron beam (e-beam) lithography has been used in the past to fabricate nanoresonators in single crystal silicon [95]. E-beam lithography is also used in this work to pattern polycrystalline diamond nanoresonators. The fabrication process of the polycrystalline diamond nanoresonators was the same used for the fabrication of the cantilevers reported in chapter 5 up to the polycrystalline diamond deposition step. A special high resolution photoresist commonly used in e-beam patterning called “PMMA” (Poly Methyl MethAcrylate) was deposited (200 nm thick) on top of the polycrystalline diamond film. After this photoresist has been patterned, a 100 nm thick Al film was deposited and patterned via lift-off. This aluminum film was used as a hard mask to pattern the polycrystalline diamond film using dry etching to form the torsional resonators and nanocantilevers.

The fabricated nanoresonator structures included cantilever structures patterned to have widths as small as 100 nm, and torsional paddle resonators with a support beam

width of 0.5 μm . The performance of these structures shows resonant frequencies and Q values in the range of 23 KHz – 805 KHz and 9,500 – 103,600 respectively. All the torsional resonators were fabricated from the the 3 types of polycrystalline diamond samples described in chapter 3, whereas the nanocantilevers were fabricated from the sample 1.

6.3 Torsional Resonators

The torsional paddle resonator structures consisted of a proof mass (paddle) with a mass close to 6.16×10^{-13} kg in a rectangular shape suspended by a 0.5 μm wide, 20 μm long polycrystalline diamond beam. The paddles were supported perpendicular to the largest side of the paddle in either one side (single) or both (double). Figure 6.1 shows an SEM image of a single torsional paddle with its dimensions. The resonant frequency of this type of resonator structure (when it is operated in its torsional vibration mode) can be calculated using the following equation [96]:

$$f_0 = \sqrt{\frac{0.0522 \times G \times b^3}{\rho \times w \times L \times d^3}} \quad (6.1)$$

where the variables b , w , L and d are the resonator dimensions shown in figure 6.1. The variable ρ and G are the polycrystalline diamond density (3520 Kg-m^{-3}) and shear modulus (480 GPa) respectively. Equation (6.1) applies to a single torsional resonator. For a double torsional resonator, the equation differs only on the constant inside the radical (0.1 is used instead of 0.0522) [96].

In order to excite a torsional movement, the paddle support had to be off the center of the paddle. Otherwise, the beam would vibrate in a flexural mode similar to a

cantilever beam. Figure 6.2 shows a diagram of this structure and the excitation mode of vibration.

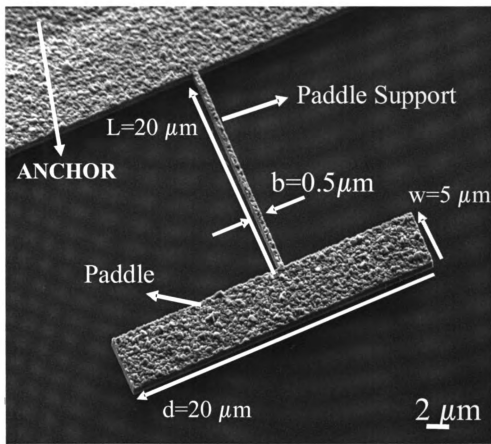


Figure 6.1 SEM image of polycrystalline diamond single torsional resonator

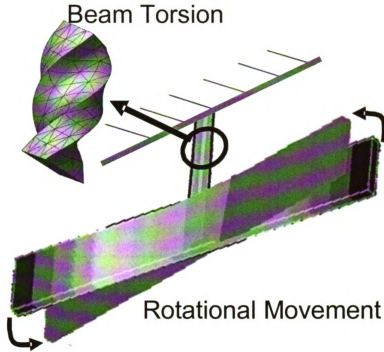


Figure 6.2 Excitation of torsional resonator. The offset of the paddle support from the center of the paddle causes a torsional vibration mode.

The patterning of the torsional resonators had to be done using e-beam lithography since the thin support ($0.5\text{ }\mu\text{m}$ wide) of the torsional paddle would have been hard to produce using optical lithography. The tested torsional resonators had a fixed width (w) of $5\text{ }\mu\text{m}$, and their lengths (d) varied from $50\text{ }\mu\text{m}$ to $20\text{ }\mu\text{m}$.

6.3.1 Testing of torsional resonators

The measurement results from the torsional resonator structures are shown in Table 6.1. As it can be noticed from the testing results, the measured Q values did not show a dependence on the number of supports of the torsional resonator, or paddle length (d). However, sample 1 shows higher Q values than the other 2 samples. This result suggests a dependence of resonator Q on the type of polycrystalline diamond film. This

same observation was made on the results shown in chapter 5 of this thesis. The measured resonant frequencies for the torsional resonators ranged from 269,645 Hz – 805,415 Hz and the Q values ranged from 17,152 – 86,603. The range of obtained frequencies are lower than those obtained on torsional paddles made of nanocrystalline diamond (13 MHz – 640 MHz) [14,34], but the measured Q values are much larger (2,500 – 10,000) [14,34].

Table 6.1 Measurement results for single and double torsional resonators

Torsional Paddles						
Single						
Length (μm)						
30		40		50		
Sample	f_0 (Hz)	Q	f_0 (Hz)	Q	f_0 (Hz)	Q
1	490,446	68,498	361,632	78,106	269,645	65,132
2	506,005	17,152	364,146	17,815	295,844	19,387
3	529,678	35,311	353,149	28,388	274,199	31,553
Double						
Length (μm)						
30		40		50		
Sample	f_0 (Hz)	Q	f_0 (Hz)	Q	f_0 (Hz)	Q
1	805,415	86,603	527,934	76,958	384,070	70,471
2	706,756	23,796	462,139	32,209	329,973	25,382
3	752,627	22,953	461,704	46,170	327,282	27,273

6.4 Nanocantilevers

For the first time, polycrystalline diamond resonators have been successfully patterned using e-beam lithography to have dimensions as small as 100 nm. The results of the patterning show sharp and smooth sidewalls as can be noticed from figure 6.3.

The mask used for the e-beam patterning was designed to include cantilevers with widths and lengths ranging from 100 nm - 1 μm and 500 nm - 200 μm respectively.

The cantilevers reported in chapter 5 had a thickness of $0.7\ \mu\text{m}$, which was much smaller than the resonator width ($10\ \mu\text{m}$). Consequently the cantilever spring constant for a vibration perpendicular to the substrate is smaller than that for a vibration parallel to the substrate. This is why the cantilever vibration was perpendicular to the substrate for the cantilevers reported in chapter 5. However, for the nanocantilevers reported in this chapter, the width ($100\ \text{nm} - 500\ \text{nm}$) is smaller than the film thickness ($\sim 0.7\ \mu\text{m}$). In this case, the cantilever spring constant for a vibration parallel to the substrate is smaller than that for a vibration perpendicular to the film substrate. As a result, the nanocantilevers reported in this chapter vibrate parallel to the substrate. The vibration detection is done by monitoring the change in the reflected beam for both cases.

Figure 6.4 shows a diagram of the vibration mode of cantilevers with a width larger (figure 6.4-a) or smaller (figure 6.4-b) than the film thickness. Figure 6.5 shows SEM images of a $100\ \text{nm}$ wide polycrystalline diamond cantilever.

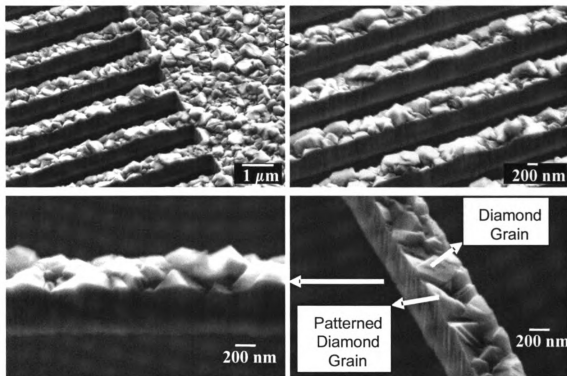
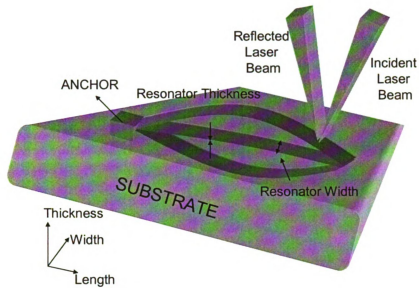


Figure 6.3 Smooth sidewalls of polycrystalline diamond nanocantilevers fabricated using e-beam lithography.

a)



b)

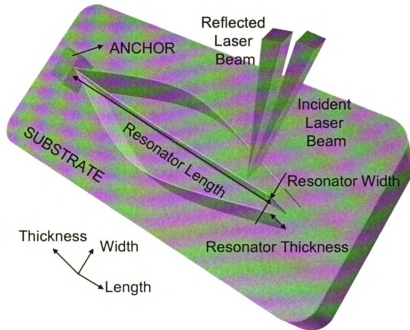


Figure 6.4 Use of Piezoelectric actuation and optical detection for a cantilever with vibration perpendicular to the substrate (a) and parallel to the substrate (b). The vibration will be in the direction parallel to the smallest dimension of the cantilever.

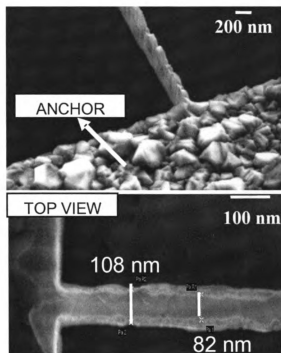


Figure 6.5 100 nm wide polycrystalline diamond cantilever. The top view shows that the width of the cantilever is not uniform along the beam length

6.4.1 Testing of nanocantilevers

The most noticeable result was the measurement of the highest Q value (103,000) found for a nanoresonator made from any polycrystalline material. (Higher Q values (~250,000) have been found in nanoresonators made of single crystal silicon [22]). This value was found for a 500 nm wide, 50 μm long cantilever. Figure 6.6 shows an SEM image of this structure and the resonant peak obtained. The tested cantilever with the smallest width was a 100 nm wide, 25 μm long cantilever beam. This structure had a resonant frequency of 475 KHz and a Q of 14,600. SEM images of this cantilever and the testing results are shown in figure 6.7.

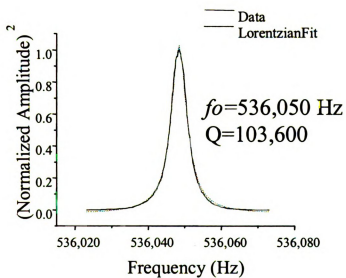
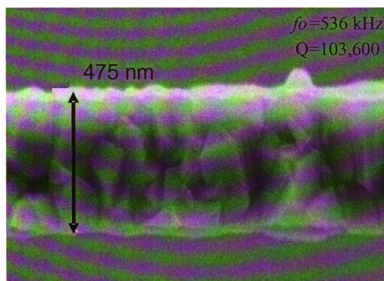


Figure 6.6 SEM image and performance of the nanocantilever with the highest measured Q .

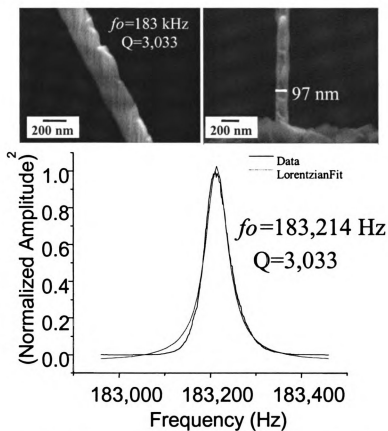


Figure 6.7 SEM image and performance of a 100 nm wide polycrystalline diamond nanocantilever

Table 6.2 shows some of the measurements of nanocantilevers. The resonant frequencies for the nanocantilevers were calculated using the equation:

$$f_o = 0.1615 \sqrt{\frac{E}{\rho}} \frac{h}{L_r^2} \quad (6.2)$$

where E and ρ are the film Young's modulus and density respectively, h is the resonator thickness, L_r is the beam length and f_o is the resonant frequency. The values for the nanocantilever width and film thickness were used as the resonator thickness in equation (6.2) to calculate the resonant frequency of the nanocantilevers. The results are shown in table 6.2. The measured resonant frequencies are closer to the calculated values using the resonator width as the resonator thickness, which indicates that the cantilevers are moving parallel to the substrate as it was expected since the beam width was smaller than the film thickness. The difference between the measured and calculated frequency values could be due to the non-uniformity of the nanocantilevers width along the beam direction as shown in figure 6.5.

Figure 6.8 shows a plot of the measured Q values on 200 nm thick cantilever beams made of single crystal silicon [26], silicon nitride [26], and polycrystalline diamond (reported in this work). The testing method for all these samples consisted of piezoelectric actuation with optical detection. A direct relationship between the measured Q values and the beam length can not be observed for any of the samples. This suggests that the dominant energy dissipation mechanism is not related to clamping losses, since the clamping losses are directly proportional to the beam length (see equation 2.32). The measured Q values for polycrystalline diamond seem to vary much more with beam length than the measured Q values for silicon nitride and single crystal silicon. One of the

possible reasons for the larger variations in Q for polycrystalline diamond could be related to the material itself. The single crystal silicon and silicon nitride nanocantilevers consist of only one uniform film. On the other hand, as it was pointed out in chapter 5, polycrystalline diamond consists of a *seeding layer* composed mainly by small diamond grains (~ 30 nm in diameter) and a *film layer* composed by much larger grains (~ 0.5 μm). The measured Q values on a structure made of two layers will depend on the thickness of each layer [14,89]. The *seeding* and *film* layer could vary in their thickness among different polycrystalline diamond nanocantilevers structures, leading to differences in Q . Another possible reason for this large variation could be the low yield that was obtained in the fabrication process of the polycrystalline diamond nanocantilevers. Due to this low yield, the number of measurements on a nanocantilever with specific dimensions was not larger than two. Although the yield was never mentioned in [26], it is possible that several measurements were taken on each nanocantilever, and the reported results was the one with the highest Q . This technique is completely valid since there are many processes that can decrease the Q , and the measurement with the highest Q would be the closest to the real Q of the device.

It is interesting to notice how the average of the measured Q values for the polycrystalline diamond nanoresonators plotted in figure 6.8 ($\sim 21,000$) is larger than that of single crystal silicon ($\sim 17,000$) and silicon nitride ($\sim 11,500$).

Table 6.2 Results of polycrystalline diamond nanocantilevers fabricated from sample 1. The resonant frequencies were calculated using the width as the resonator thickness (a), and the film thickness as the resonator thickness (b). M* represents the number of measurements taken from each structure (the values shown in the table correspond to the measurement with the highest measured Q).

NANOCANTILEVERS									
Dimensions	Width = 200 nm				Width = 500 nm				Film Thickness $t = 0.7 \mu\text{m}$
Length (μm)	Meas. f_0 (Hz)	Q	Calc. ^a f_0 (Hz)	M*	Meas. f_0 (Hz)	Q	Calc. ^a f_0 (Hz)	M*	Calc. ^b f_0 (Hz)
50	210,023	21,003	219,640	1	536,050	103,600	549,100	2	768,740
75	77,506	14,850	97,617	1	243,725	9,580	244,044	1	341,166
100	50,907	28,125	54,910	1	136,558	10,115	137,275	1	192,185
150	23,240	20,100	24,404	2	56,090	22,987	61,011	1	85,415

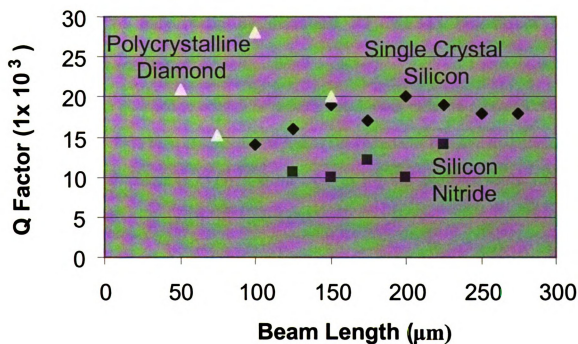


Figure 6.8 Plot of measured Q values on cantilever beams made of silicon nitride [26], single crystal silicon [26] and polycrystalline diamond (reported in this work). All the cantilevers had a thickness between 170 nm and 200 nm

Chapter 7

Conclusions and Future Research

7.1 Summary and Conclusions

- **Testing of polycrystalline diamond RF MEMS resonators using different methods**

Polycrystalline diamond resonators have been tested using different actuation methods, and the results have been compared. The results showed similar resonant frequencies, and a significant difference in Q (by a factor close to 10) was attributed to the resonator testing pressure.

- **Measured the highest Q values**

A Q of 116,000 has been measured on a cantilever beam made of an undoped polycrystalline diamond film grown at 780°C. Highly doped ($5 \times 10^{-9} \text{ cm}^{-3}$) polycrystalline diamond films grown at 780 °C and undoped polycrystalline diamond films grown at 600 °C had about half the Q values obtained from undoped polycrystalline diamond films grown at 780 °C.

- **Study of frequency thermal stability of polycrystalline diamond resonators.**

The performance of polycrystalline diamond resonators at elevated temperatures showed thermal coefficient values ranging from $-1.59 \times 10^{-5} / ^\circ\text{C}$ to $-2.56 \times 10^{-5} / ^\circ\text{C}$. for different polycrystalline diamond films.

- **Study of energy dissipation mechanisms in polycrystalline diamond resonators.**

The measured Q values on different polycrystalline diamond films were not limited by clamping losses, thermoelastic dissipation or phonon-phonon interaction. In order to identify the mechanism responsible for limiting the highest possible achievable Q, the Q values were measured as a function of temperature and an apparent thermally activated relaxation mechanism was identified with an activation energy around 1.9 eV.

- **Design, fabrication and testing of polycrystalline diamond nanoresonators**

Polycrystalline diamond films have been patterned to fabricate cantilever structures with widths as small as 100 nm. The measured data does not show a relationship between the Q values and the cantilever beam length.

7.2 Future Research

Some areas of future research are:

1. Polished polycrystalline diamond films: This film can be used to produce polycrystalline diamond resonator structures with smooth surfaces. This would be very significant for the fabrication of polycrystalline diamond nanoresonators.

2. Improvement of the yield in the fabrication of polycrystalline diamond nanoresonators: Modifications to the fabrication process of polycrystalline diamond resonators could lead to an increase in the yield of such devices. By increasing the yield, the characterization and the performance of polycrystalline diamond nanoresonators can be studied in more detail.

BIBLIOGRAPHY

BIBLIOGRAPHY:

- [1] C. T.-C. Nguyen, "Microelectromechanical devices for wireless communications (invited)," *Proceedings*, 1998 IEEE International Micro Electro Mechanical Systems Workshop, Heidelberg, Germany, Jan. 25-29, 1998, pp. 1-7.
- [2] C. T.C. Nguyen, "Transceiver front-end architectures using vibrating micromechanical signal processors (invited)," *Dig. Of Papers*, Topical Meeting on Silicon Monolithic Integrated Circuits in RF Systems, Sept. 12-14, 2001, pp.23-32
- [3] R. T. Howe and R. S. Muller, "Resonant microbridge vapor sensor," *IEEE Trans. Electron Devices*, vol. ED-33, pp. 499-506, 1986.
- [4] N. M. Nguyen and R. G. Meyer, "Si IC-compatible inductors and LC passive filters," *IEEE J. of Solid-State Circuits*, vol.SC-25, no. 4, pp. 1028-1031, Aug. 1990.
- [5] N. M. Nguyen and R. G. Meyer, "A 1.8-GHz monolithic LC voltage-controlled oscillator," *IEEE J. of Solid-State Circuits*, vol. SC-27, no. 3, pp. 444-450.
- [6] S. V. Krishnaswamy, J. Rosenbaum, S. Horwitz, C. Yale, and R. A. Moore, "Compact FBAR filters offer low-loss performance," *Microwaves & RF*, pp. 127-136, Sept. 1991.
- [7] Jing Wang, James E. Butler, Tatyana Feygelson and Clark T.-C. Nguyen "1.51-GHz Nanocrystalline diamond micromechanical disk resonator with material-mismatched isolating support" To be published in *IEEE Transducers '04*.
- [8] Clark T.-C. Nguyen, "Vibrating RF MEMS for low power wireless communications (invited)," *Proceedings*, 2000 Int. MEMS Workshop (iMEMS'01), Singapore, July 4-6, pp.21-34
- [9] L. Meirovitch, *Analytical Methods in Vibrations*. New York: Macmillan Publishing Co, Inc. 1967
- [10] W. Weaver, S. P. Timoshenko, and D. H. Young, *Vibration Problems in Engineering*, 5th ed: Wiley Publishers, 1990
- [11] Kun Wang, Ark-Chew Wong, Clark T.-C. Nguyen "VHF Free-Free Beam High-Q Micromechanical Resonators" *IEEE Journal of Microelectromechanical Systems*, Vol 9. No.3 (2000) pp. 347-360
- [12] P. J. Petersan and S. M. Anlage, "Measurement of resonant frequency and quality factor of microwave resonators: Comparison of methods" *Journal of Applied Physics*, vol. 84, pp. 3392-3402, 1998
- [13] D. Czaplewski, J.P. Sullivan, T.A. Friedmann, D.W. Carr, B.E.N. Keeler and J.R. Wendt; *J. Appl. Phys.* 97, 023517 (2005).

- [14] A.B. Hutchinson, P.A. Truitt and K.C. Schwab, L. Sekaric, J.M. Parpia, H.G. Craighead and J.E. Butler; *Appl. Phys. Lett* 84 (6) 2004, 972
- [15] J. R. Clark, W.-T. Hsu, and C. T.-C. Nguyen, "Measurement techniques for capacitively-transduced VHF-to-UHF micromechanical resonators" *Digest of Technical Papers*, the 11th Int. Conf. on Solid-State Sensors & Actuators (Transducers'01), Munich, Germany, June 10-14, 2001, pp. 1118-1121.
- [16] P. Mohanty, D. A. Harrington, K. L. Ekinci, Y. T. Yang, M. J. Murphy, and M. L. Roukes, "Intrinsic dissipation in high-frequency micromechanical resonators," *Physical Review B*, vol. 66, pp. 085416 1-15, 2002.
- [17] P.M. Osterberg and S.D. Senturia, "M-Test: A test chip for MEMS material property measurement using electrostatically actuated test structures" *J. Microelectromechanical Systems*, vol. 6 pp. 107-118, 1997.
- [18] R. H. Blick, A. Erbe, H. Krömmner, A. Kraus, J. P. Kotthaus, *Phys. E* 6, 821 (2000)
- [19] D. W. Carr, *Nanoelectromechanical Resonators*, Ph.D. thesis Cornell University 2000
- [20] Stephen D. Senturia *Microsystem Design*; Kluwer Academic Publishers 2001
- [21] E. Buks, M.L. Roukes, *Europhys. Lett.* 54, 2220 (2001) and E. Buks, M.L. Roukes, *Phys. Rev. B.* 63, 033402 (2001)
- [22] J. Yang, T. Ono and M. Esashi, *IEEE J. Microelectromech. Sys.* 11(6) Dec. 2002, 775
- [23] F.R. Blom, S. Bowstra, M. Elwenspoek, J.H.J. Fluitman "Dependence of the quality factor of micromachined silicon beam resonators on pressure and geometry" *J. Vac. Sci. Technol. B* 10(1), Jan/Feb 1992.
- [24] T. V. Roszart, "The effect of thermoelastic internal friction on the Q of micromachined silicon resonators," in *Tech. Dig. Solid-State Sens. Actuator Workshop*, Hilton Head, SC, 1990, pp. 13-16.
- [25] V. B. Braginsky, V. P. Mitrofanov, V. I. Panov, K. S. Thorne, *Systems with Small Dissipation*, The University of Chicago Press, 1985
- [26] K.Y. Yasumura, T.D. Stowe, E.M. Chow, T. Pfafman, T.W. Kenny, B.C. Stipe and D. Rugar, *J. Microelectromech. Sys.* 9(1) Mar. 2000, 117
- [27] W.-T. Hsu, J. R. Clark, and C. T.-C. Nguyen, "A sub-micron capacitive gap process for multiple-metal-electrode lateral micromechanical resonators," *Technical Digest*, 14th Int. IEEE Micro Electro Mechanical Systems Conference, Interlaken, Switzerland, Jan.

21-25, 2001, pp. 349-352.

[28] P.M. Osterberg and S.D. Senturia, "M-Test: A test chip for MEMS material property measurement using electrostatically actuated test structures" *J. Microelectromechanical Systems*, vol. 6 pp. 107-118, 1997.

[29] G. Pearson, W. Read, Jr., and W. Feldman, "Deformation and fracture of small Si crystals," *Acta Metall.*, vol. 5, p. 181, 1957.

[30] Shuvo Roy, Russell G. DeAnna, Christian A. Zorman and Mehran Mehregany "Fabrication and Characterization of Polycrystalline SiC Resonators" *IEEE Transactions on Electron Devices*, vol. 49, No.12 December 2002.

[31] Jing Wang, James E. Butler, D.S.Y. Hsu and Clark T.-C. Nguyen "CVD Polycrystalline diamond high-Q micromechanical resonators" *IEEE International Conference Micro Electro Mechanical Systems*, 2002. pp. 657-660

[32] J. Wang, J. E. Butler, D.S.Y. Hsu, and C. T. -C. Nguyen, "High-Q Micromechanical resonators in CH₄-reactant optimized high acoustic velocity CVD polydiamond" *Tech. Digest, 2002 Solid-State Sensor, Actuator and Microsystems Workshop*, Hilton Head Island, South Carolina, June 2-6, 2002, pp. 61-62.

[33] N. Sepúlveda, D.M. Aslam, J.P. Sullivan, "Polycrystalline diamond RF MEMS resonators with the highest quality factors" to be presented at *IEEE MEMS'06*.

[34] L. Sekarik, J.M. Parpia, H.G. Craighead, T. Feygelson, B.H. Houston, J.E. Butler, J. *Appl. Phys.* 81, 23 pp.4455 (2002).

[35] Mustafa U. Demirci, Mohamed A. Abdelmoneum and Clark T.-C. Nguyen "Mechanically corner-coupled square microresonator array for reduced series motional resistance", *IEEE Transducers, Solid-State Sensors, Actuators and Microsystems*, 12th International Conference, vol.2 June9-12, 2003

[36] F. Bannon III, Clark, John R., Clark T.-C. Nguyen "High Q HF Micromechanical Filters", *IEEE JSSC*, pp.512-526, April 2000

[37] Navid, R.; Clark J.R.; Demirci, M; Nguyen, C.T.-C. "Third-order intermodulation distortion in capacitively-driven CC-beam micromechanical resonators" *IEEE International Conference on Micro Electro Mechanical Systems*, 2001. pp.228-231

[38] Colm M Flannery, Michael D Whitfield and Richard B Jackman "Acoustic wave properties of CVD diamond" *Institute of Physics Publishing. Semicond. Sci. Technol.* 18 (2003) S86-S95

[39] K. Iakoubovskii, *Optical Study of Defects in Diamond*, PhD thesis, Katholieke Universiteit Leuven, 2000.

- [40] Y. Tang and D. M. Aslam "Technology of polycrystalline diamond thin films for microsystems applications" J. Vac. Sci. Technol. B 23(3), May/Jun 2005
- [41] S. Matsumoto, Y. Sato, M. Kamo, and N. Setaka, Jpn. J. Appl. Phys., Part 1 **21**, 183 (1982).
- [42] R. C. Hyer, M. Green, K. K. Mishra, and S. C. Sharma, J. Mater. Sci. Lett. **10**, 515 (1991).
- [43] A. Lettington and J. W. Steeds, *Thin Film Diamond* _Chapman and Hall, London, (1994).
- [44] J. Stiegler, Y. vonKaenel, M. Cans, and E. Blank, J. Mater. Res. **11**, 716 (1996).
- [45] L.A. Chernozatonskii, Z. Ya. Kosakovskaya, Yu. V. Gulyaev, N.I. Sinitsyn, G.V. Torgashov, and Yu. F. F. Zakharchenko, "Influence of external factors on electron field emission from thin-film nanofilament carbon structures" J. Vac Sci Technol. B 14(3), p. 2080, 1996.
- [46] T. Xie, W.A. Mackie and P.R. Davis, "Field emission from ZrC films on SSi and Mo single emitters and emitter arrays", J. Vac Sci. Technol. B 14(3), p.2090, 1996.
- [47] J.S. Ma, H. Kawarda, T. Yonehara, J.I. Suzuki, J. Wei, Y. Yokota and A Hiraki "Selective Nucelation and Growth of Diamond Particles by Plasma-assisted Chemical Vapor Deposition" App. Phys. Lett., vol. 55 no.11, pp.1071-1073, 1989.
- [48] M.P. Everson and M.A. Tamor :Studies of Nucleation and Growth Morphology of Boron-doped Diamond Microcrystals by Scanning Tunnelling Microscopy" J. Vac. Sci. Technol. B, vol.9 no.3 pp. 1570-1575, 1991.
- [49] S. Ijima, Y. Aikawa, and K. Baba, "Early Formation of Cemical Vapor Deposition Diamond Films" Appl. Phys. Lett., vol.57, no.25, pp. 2646-2648, 1990.
- [50] K. Hirabayashi, Y. Taniguchi, O. Takamatsu, T. Ikeda, K. Ikoma and N. Iwasaki-Kurihara. "Selective Deposition of Diamond Crystals by Chemcial Vapor Deposition Using a Tungsten-filament Method" Appl. Phys. Lett., vol. 53 no.19 pp. 1815-1871, 1988.
- [51] B.W. Sheldon, R. Csencstis, J. Rankin, and R.E. Boekenhauer, "Bias-enhanced Nucleation of Diamond During Microwave-assisted Chemical Vapor Deposition" J. Appl. Phys., vol. 75, no.10, pp.5001-5008, 1994.
- [52] B.R. Stoner, G.H. Ma, S.D. Wolter, and J.T. Glass, "Characterization of Bias-enhanced Nucleation of Diamond on Silicon by in vacuo Surface Analysis and Transmission Electron Microscopy" Phys Rev. B. vol.45, pp.11067-11084, 1992.

- [53] X. Jiang, C.P. Klages, R. Zachai, M. Hartweg and H.J. Fusser, "Epitaxial Diamond Thin Films on (001) Silicon Substrates" *Appl. Phys. Lett.*, vol. 62, pp.3438-3440, (1993).
- [54] A. Massod, M. Aslam, M.A. Tamor and T.J. Potter, "Techniques for Patterning CVD Diamond Films on Non-diamond substrates," *J. Electrochem. Soc.*, vol 138. no.11pp. L67-L68, 1991.
- [55] B.V. Spitsyn, G. Popovic and M.A. Prelas, "Problems of Diamond Film Doping" 2nd Int Conf. on the Application of Diamond Films and Related Materials, Ed. M. Yoshikawa, M. Murakawa, Y. Tzeng and W.A. Yarbrough, MY, Tokyo., pp. 57-64, 1993.
- [56] Gennady SH. Gildneblat, Stephen A. Grot, and Andrzej Badzian, "The electrical properties and Device Applications of Homoepitaxial and Polycrystalline Diamond Films" in *Proc. Of the IEEE*, vol. 79, pp647-667, 1991.
- [57] T. Takada, T. Fukunaga, K. Hayashi, and Y. Yokota, *Sens. Actuators, A* **82**, 97 (2000).
- [58] J. Cifre, J. Puigdollers, M. C. Polo, and J. Esteve, *Diamond Relat. Mater.* **3**, 628 (1994).
- [59] J.F. Prins, *Thin Solid Films* **212**, 11 (1992)
- [60] J.F. Prins, *Diamond Related Materials*. **11**, 612 (2002)
- [61] F. Zhang, E. Xie, B. Yang, Y. Cai and G. Chen, "Synthesis and Infrared Absorption Characteristics of Boron-Doped Semiconducting Diamond Thin Films". *Materials Letters*, vol. 19, pp.115-118, 1994
- [62] X. Jiang, M. Paul, P. Willich, E. Bottger and C.-P. Klages, "Controlled Boron Doping in Chemical Vapor Deposited Diamond Films", *Diamond 96*, Tours, France, Sept. 8-13, poster 11.051, 1996
- [63] E. Colineau, et.al. "Minimization of Defects Concentration from Boron Incorporation in Polycrystalline Diamond Films", *Diamond 96*, Tours, France, Sept. 8-13, poster 11.0512, 1996.
- [64] X.Z. Liao, et al. "The influence of Boron Doping on the Structure and Characteristics of Diamond Thin Films," *Diamond 96*, Tours, France, Sept. 8-13, poster 8.060, 1996
- [65] K. Miyata, K. Kumagai, K. Nishimura and K. Kobashi, "Morphology of heavily B-Doped Diamond Films," *J. Mat. Res.*, vol.8, pp. 2845-2857, 1997.

- [66] T. Roppel, R. Ramesham and S.Y. Lee, "Thin Film Diamond Microstructures" *Thin Solid Films*, vol. 212, pp.56-62, 1992.
- [67] J.L. Davidson, C. Ellis and R. Ramesham, "Selective Deposition of Diamond Films," *New Diamond*, vol.6, pp.29-32, 1990.
- [68] O. Dorsch, M. Werner, and E. Obermeier, *Diamond Relat. Mater.* **4**, 456 (1995).
- [69] M. Bernard, A. Deneuve, T. Lagarde, and E. Treboux, *Diamond Relat. Mater.* **11**, 828 (2002).
- [70] C. Vivensang, L. FerlazzoManin, M. F. Ravet, and G. Turban, *Diamond Relat. Mater.* **5**, 840 (1996).
- [71] R. Otterbach and U. Hilleringmann, *Diamond Relat. Mater.* **11**, 841(2002).
- [72] H. Shiomi, *Jpn. J. Appl. Phys., Part 1* **36**, 7745 (1997).
- [73] F. Silva, R. S. Sussmann, F. Benedic, and A. Gicquel, *Diamond Relat. Mater.* **12**, 369 (2003).
- [74] W. Kern and D. A. Puotinen, *RCA Rev.* **31**, 187 (1970).
- [75] R. R. Thomas, F. B. Kaufman, J. T. Kirleis, and R. A. Belsky, *J. Electrochem. Soc.* **143**, 643 (1996).
- [76] N. Sepulveda-Alancastro and D. M. Aslam, "Polycrystalline diamond technology for RF MEMS Resonators" *Microelectron. Eng.* **73-74**, 435 (2004).
- [77] H. Windischmann, Glenn F. Epps, Yue Cong and R. W. Collins, "Intrinsic stress in diamond films prepared by microwave plasma CVD" *J. Appl. Phys.* **69** (4) Feb. 1991, pp. 2231-2237.
- [78] P T Docker, P K Kinnell and M C L Ward, "Development of the one-step DRIE dry process for unconstrained fabrication of released MEMS devices" *J. Micromech. Microeng.* **14** pp. 941-944 (2004)
- [79] L M Phinney , G Lin, J Wellman and A Garcia, "Surface roughness measurements of micromachined polycrystalline silicon films" *J. of Micromechanics and Microengineering* **14**, 927-93, 2004
- [80] John R. Clark, Wan-Thai Hsu, and Clark T.-C. Nguyen, "High-Q VHF Micromechanical Contour-Mode Disk Resonator" *IEEE Int. Electron Devices Meeting* , Dec 11-13, 2000 pp. 493-496.

- [81] N. Sepulveda, D.M. Aslam, J.P. Sullivan, "Polycrystalline Diamond MEMS Resonator Technology for Sensor Applications" *Diamond and Related Materials*, Currently in press.
- [82] Kirt R. Williams, Kishan Gupta, Mathew Wasilik, "Etch rates for micromachining process-Part II" *IEEE J. Micro Electrom. Sys.* Vol.12 no.6 Dec 2003.
- [83] Ville Kaajakari, Tomi Mattila, Antti Lipsanen, and Aarne Oja, "Nonlinear Mechanical Effects in Silicon Longitudinal Mode Beam Resonators", *Sensors and Actuators A: Physical* vol. 120(1), pp.64-70, 2005
- [84] E. S. Zouboulis, M. Grimsditch, A. K. Ramdas and S. Rodriguez, "Temperature dependence of the elastic moduli of diamond: A Brillouin-scattering study" *Physical Review B*, vol. 57, pp. 2889-2896, 1998.
- [85] F. Szuecs, M. Werner, R. S. Sussmann, C. S. J. Pickles and H. J. Fecht, "Temperature dependence of Young's modulus and degradation of chemical vapor deposited diamond" *Journal of Applied Physics* vol. 86, pp.6010-6017, 1999
- [86] J. O. Orwa, K. W. Nugent, D. N. Jamieson, and S. Praver, "Raman investigation of damage caused by deep ion implantation in diamond", *Physical Review B*, vol. 62, pp.5461-5472, 2000.
- [87] Liwei Lin, "MEMS Post-Packaging by Localized Heating and Bonding", *IEEE TRANSACTIONS ON ADVANCED PACKAGING*, VOL. 23, NO. 4, PP. 608-616, NOVEMBER 2000
- [88] X. Liu, D.M. Photiadis, J.A. Bucaro, J.F. Vignola, B.H. Houston, H.-D. Wu, D.B. Chrisey, "Low temperature internal friction of diamond-like carbon films" *Material Science and Engineering A*, 5 July 2002.
- [89] B.E. White, Jr., R.O. Pohl, *Materials Research Symposium Proc.* 356 (1995) 567.
- [90] Victor J. Milenkovic, "Rotational polygon containment and minimum enclosure using only robust 2D constructions" *Computational Geometry, Theory and Applications* (13) pp.3-19 1999
- [91] H. Freeman and R. Shapira, "Determining the Minimum-Area Encasing Rectangle and Arbitrary Closed Curve", *Communications of the ACM*, vol. 18 pp.409-413, 1975
- [92] H. J. McSkimin and P. Andreatch Jr, "Elastic Moduli of Diamond as a Function of Pressure and Temperature" *Journal of Applied Physics*, vol. 43, pp. 2944-2948, July 1972.

[93] W. T. Hsu; C.T.-C. Nguyen, "Stiffness-compensated temperature-insensitive micromechanical resonators" IEEE Int. Conference on MEMS, pp.731 – 734, Jan 20-24 2002

[94] . T. Hsu; J.R Clark,.; C.T.-C Nguyen,.; "Mechanically temperature-compensated flexural-mode micromechanical resonators" Electron Devices Meeting, International pp. 399 – 402, Dec 10-13 2000

[95] J. Yang, T. Ono, and M. Esashi, "Mechanical behavior of ultrathin micro-cantilever," *Sens. Actuators*, vol. 82, pp. 102–107, 2000

[96] D.A. Czaplewski, J.P. Sullivan, T.A. Friedmann and J.R. Wendt, "Mechanical dissipation at elevated temperatures in tetrahedral amorphous carbon oscillators" *Diamond and Related Materials*, Currently in press.